Array Processing for Mobile Wireless Communication in the 60 GHz Band

Daniel J. Jakubisin

Thesis submitted to the Faculty of the
Virginia Polytechnic Institute and State University
in partial fulfillment of the requirements for the degree of

Master of Science
in
Electrical Engineering

Claudio R. C. M. da Silva, Co-Chair
R. Michael Buehrer, Co-Chair
Steven W. Ellingson

November 9, 2012
Blacksburg, Virginia

Keywords: communications, array processing, 60 GHz band

Array Processing for Mobile Wireless Communication in the 60 GHz Band

Daniel J. Jakubisin

(ABSTRACT)

In 2001, the Federal Communications Commission made available a large block of spectrum known as the 60 GHz band. The 60 GHz band is attractive because it provides the opportunity of multi-Gbps data rates with unlicensed commercial use. One of the main challenges facing the use of this band is poor propagation characteristics including high path loss and strong attenuation due to oxygen absorption. Antenna arrays have been proposed as a means of combating these effects. This thesis provides an analysis of array processing for communication systems operating in the 60 GHz band. Based on measurement campaigns at 60 GHz, deterministic modeling of the channel through ray tracing is proposed. We conduct a site-specific study using ray tracing to model an outdoor and an indoor environment on the Virginia Tech campus. Because arrays are required for antenna gain and adaptability, we explore the use of arrays as a form of equalization in the presence of channel-induced intersymbol interference. The first contribution of this thesis is to establish the expected performance achieved by arrays in the outdoor environment. The second contribution is to analyze the performance of adaptive algorithms applied to array processing in mobile indoor and outdoor environments.

Dedication

To my wife, Emily,

Thank you for your patience and loving encouragement.

Acknowledgments

I would like to thank Dr. da Silva for his investment in my education from the very beginning of my graduate studies. It was his course – Stochastic Signals and Systems – that gave me an entirely new view of communications theory. I am grateful for his willingness to advise me through my M.S. studies and teach me how rigorous research is conducted. I would also like to thank Dr. Buehrer for his input into this thesis and specifically for his willingness to advise me as I continue my education and pursue a Ph.D. degree.

To Gautham, Chris, Yue, and Dhiraj – the fellow "da Silva students" – thank you for all your encouragement and input throughout these years.

I would like to thank my parents, Chuck and Nita; until college they taught me everything I know. Many times I know you wondered if home schooling was going to work. Thank you for persevering. Finally, I am grateful to Jesus Christ for giving up his life so that I might have life in him. Everything that I accomplish is through him.

Contents

List of Figures

List of Tables

Chapter 1

Introduction

Frequency spectrum around 60 GHz has been allocated for unlicensed use in numerous countries around the globe. In the United States, the Federal Communications Commission (FCC) designated the frequency band from 57–64 GHz for unlicensed use in 2001 [1]. This block of spectrum, commonly referred to as the 60 GHz band, is attractive because its bandwidth far surpasses other unlicensed allocations, with the exception of ultra-wideband (UWB). The FCC has set a favorable equivalent isotropically radiated power (EIRP) transmission limit for the 60 GHz band – orders of magnitude higher than that of UWB [2]. As a result, systems operating in this band are expected to be capable of supporting multi-Gbps data rates. Consumer demand for wire-free transmission and mobility has led to widespread adoption of wireless systems in recent years. As this trend continues, the 60 GHz band has the potential to meet growing demand for higher data rate wireless communication.

Although the 60 GHz band has been available for over a decade, semiconductor technology traditionally used for millimeter wave (30–300 GHz) radio frequency front ends is still too expensive for commercial applications [1], [2], [3]. Recent advances to reduce the dimensions of complementary metal-oxide-semiconductor (CMOS) has made operation at 60 GHz feasible for this technology [2]. With affordable CMOS technology now becoming available at 60 GHz, it is important that other challenges to operation in the 60 GHz band are addressed.

One such challenge is poor propagation characteristics. Electromagnetic waves in the 60 GHz band experience strong attenuation from oxygen molecules [4] and significant power loss in transmission through common building materials [5], [6], [7]. Furthermore, path loss increases with frequency which in turn reduces received power. Consider the equation for power transmission over a communication link [8]

$$P_r = P_t \frac{G_t G_r \lambda_c^2}{(4\pi d)^2} \tag{1.1}$$

where P_r is the received power, P_t is the transmitted power, G_t is the transmitter's antenna gain, G_r is the receiver's antenna gain, λ_c is the carrier wavelength, and d is the distance between the transmitter and receiver. The received power is proportional to the square of the signal wavelength. For example, received power is 28 dB lower at 60 GHz than at 2.4 GHz due to increased path loss.

Systems in the 60 GHz band must compensate through increased antenna gain. Antenna gain is expressed as [8]

$$G = \frac{4\pi}{\lambda_c^2} A_e \tag{1.2}$$

where A_e is the effective aperture of the antenna. Substitution of (1.2) into (1.1) produces

$$P_r = P_t \frac{A_{e,t} A_{e,r}}{d^2 \lambda_c^2}. \tag{1.3}$$

Thus, for constant effective aperture at both the transmitter and receiver, the ratio of received power to transmitted power is *inversely* proportional to the square of wavelength and actually increases with higher frequency. This demonstrates the potential for strong received signal power at 60 GHz. The required trade-off for antenna gain is directional transmission which reduces coverage area.

Antenna arrays are a viable option for achieving the required effective aperture. Array elements with half-wavelength spacing are separated by 2.5 mm at a carrier frequency of 60 GHz. Thus, four by four and six by six planar arrays have reasonable dimensions for a handheld device. In time-varying channels (for example, mobile applications) antenna arrays are able to achieve high antenna gain while remaining adaptable to changes in the propagation environment. Acquisition and tracking of highly directional links arise as two challenges to the development of 60 GHz technology.

Initially, 60 GHz technology is expected to support high throughput, short range transmission within a home or office setting. Two standardization efforts have been undertaken by the Institute of Electrical and Electronics Engineers (IEEE). They are 802.15.3c for wireless personal area networks (WPANs) and 802.11ad for wireless local area networks (WLANs). The IEEE task groups in charge of these standards have identified numerous potential applications [9], the majority of which are for indoor networks or fixed outdoor networks. Thus, as the authors of [10] state "much of the current research involving mm-wave short range communications has been carried out considering a range of indoor environments for stationary transmitter and receiver scenarios". However, two important mobile outdoor applications have been identified: public safety radios [9] and soldier-to-soldier military radios [10]. Both applications would benefit from the high capacity offered by the 60 GHz band. For example, the ability to transmit live video between first responders (soldiers) as well as back to a headquarters (command and control center) is seen as a significant advantage.

The focus of this thesis is on the unique challenges to array processing in mobile outdoor networks. Outdoor networks must support a longer range of transmission than is expected of indoor home and office networks. Measurement studies have shown that delay spread in a wireless channel is often significantly higher outdoors than it is indoors [11]. Since delay spread provides an indication of intersymbol interference (ISI) due to multipath, this means that outdoor links are generally more susceptible to ISI. Furthermore, in mobile networks the array processor must adapt to the time-varying channel. Thus, efficient algorithms for acquisition and tracking are required.

1.1 Contribution of this work

This thesis provides an analysis of array processing for communication systems operating in the 60 GHz band. We conduct a site-specific study using ray tracing to model an outdoor and indoor environment on the Virginia Tech campus. Because arrays are required for antenna gain and adaptability, we explore the use of arrays as a form of equalization in the presence of channel-induced ISI. The proposal specification for 802.11ad defines single carrier and orthogonal frequency division multiplexing (OFDM) modulations for the physical layer [12]. All devices are required to support a single carrier, binary-phase-shift-keying (BPSK) modulation while higher order single carrier modulations and OFDM are optional. Thus, throughout this work, we utilize a single carrier system with BPSK or quadrature-phase-shift-keying (QPSK) modulation and a narrowband array processor. The first contribution is to establish the expected performance given this system model by evaluating the probability of a bit error P_b with nodes randomly placed outdoors. The second contribution is to simulate the mobile channel at 60 GHz for both outdoor and indoor environments and to analyze the performance of adaptive algorithms applied to array processing.

The system model is presented in Chapter 2. Based on measurement campaigns at 60 GHz, deterministic modeling of the channel through ray tracing is proposed. The ray tracer is presented and a mathematical framework for the following chapters is laid out.

Chapter 3 provides an initial investigation of outdoor performance in the 60 GHz band. A basic form of array processing known as beamsteering is utilized for this chapter. We evaluate the ability of four array geometries to mitigate ISI due to multipath. This chapter demonstrates the potential of the 60 GHz band for outdoor communication links while showing deficiencies in the beamsteering method. The results of this chapter guide our study of array processor performance in the following chapters.

Chapter 4 provides a survey of array processing methods and analyzes their performance in the stationary outdoor channel with complete channel knowledge. Derivations of array processing methods are given for four optimality criteria. This chapter demonstrates that significant performance gains can be achieved over the results of Chapter 3 by implementing a more advanced form of array processing. In addition, we make a comparison with the performance of beam codebook based array processing which is a low-complexity method of array processing developed for the 802.15.3c standard. The Minimum Mean Squared Error (MMSE) optimality criterion is identified as the best choice for adaptive methods considered in Chapter 5.

In Chapter 5, we remove the assumption of a stationary channel and perfect channel knowledge. Three adaptive methods are compared in terms of their ability to acquire the MMSE array weights and track the changing channel. The ray tracer developed in Chapter 2 is used to model the mobile channel in both the outdoor and indoor environments. We compare the performance achieved by the adaptive algorithms to the MMSE performance with perfect channel knowledge.

Finally, in Chapter 6 conclusions are drawn.

Chapter 2

System Model

This work focuses on array processing algorithms for optimizing the performance of a communication link in the 60 GHz band. The effectiveness of array processing is highly dependent on the channel between the transmitter and receiver. Thus, a significant part of our effort is devoted to modeling the channel.

A block diagram of the communication system is displayed in Fig. 2.1. The "Modulator" block is used to represent bit-to-symbol conversion and pulse shaping. The transmitter and receiver are equipped with antenna arrays which have N_t and N_r elements, respectively. The channel is modeled as a multipath channel with K paths. The "RF Processing & Matched Filter" block incorporates down-conversion, matched filtering, and sampling. The "De-Mod" block includes both symbol detection and symbol-to-bit conversion.

We begin in Section 2.1 with channel modeling where we present the ray tracer developed for this work. In Section 2.2, the basics of phased array antennas are covered. A mathematical overview of the entire system is presented in Section 2.3. Also, Section 2.3 covers how the probability of a bit error P_b is calculated in the following chapters.

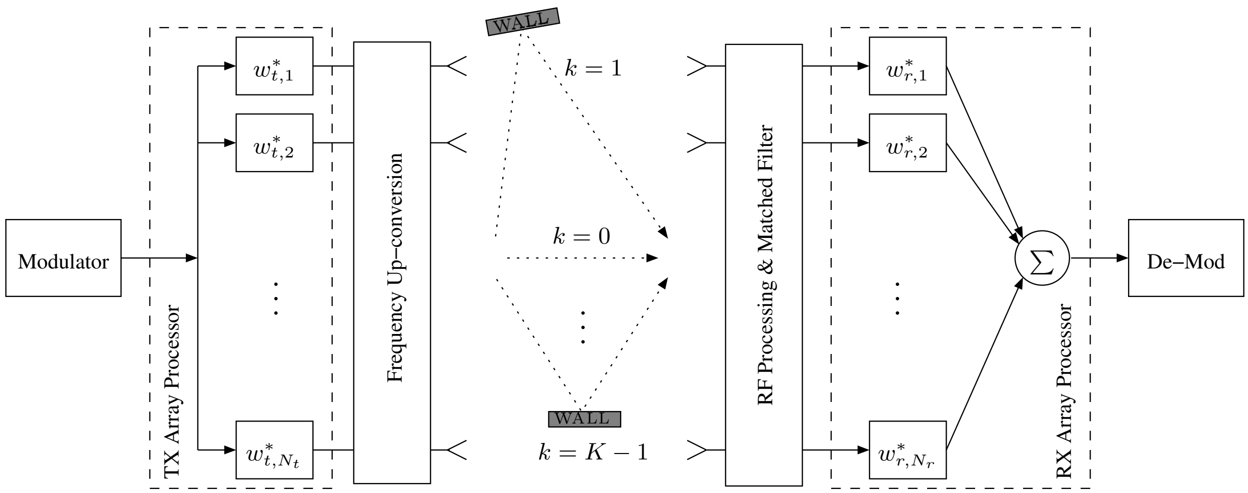

Figure 2.1: System block diagram

2.1 Channel model

A significant amount of literature is available on experimental characterization of the wireless channel at 60 GHz. A partial list of such measurement campaigns includes [6], [13], [14], [15], [16], and [17]. In [18], probabilistic channel models are developed for three environments: a conference room, an office cubicle, and a living room. The models are characterized specific to the geometry, material characteristics, and blockage that is typical in each environment. However, probabilistic models are not well developed for outdoor environments. Furthermore, probabilistic models developed for the indoor environment do not support time-variation in the channel. Measurements at 60 GHz have demonstrated that the channel can be modeled with sufficient accuracy using ray tracing [6], [17]. Other works which use ray tracing to model the 60 GHz channel outdoors include [10], [17], and [19]. In fact, [18] uses the results of ray tracing in addition to experimental measurements to develop probabilistic channel models. Because the focus of this work is on the outdoor environment, a ray tracer is developed to deterministically model the channel. This is particularly important in Chapter 5 where ray tracing is used to study a time-varying mobile channel.

The academic portion of the campus of Virginia Tech is used as the outdoor environment and the conference room of 460 Durham Hall is used as the indoor environment. Ray tracing is applied to these environments to find the set of paths between the transmitter and receiver. From this data, parameters of the channel impulse response (CIR) are calculated. We characterize the outdoor channel using the results of ray tracing and compare with channel measurements conducted in [13].

2.1.1 Ray tracing

Multipath arriving at a receiver may arise from a line-of-sight (LOS) path, from transmission through obstructions, and from reflection, diffraction, and scattering off of obstructions in the path of the transmitted signal. Measurements at 60 GHz conducted in [6] and [17] demonstrate that the LOS and reflected paths are the dominant sources of received power. In [17], a comparison is made to measurements at 1.7 GHz which shows that higher penetration, reflection, and diffraction losses are unique to the 60 GHz band when compared with lower frequencies. Both [6] and [17] argue for deterministic channel modeling based on ray tracing of the LOS and reflected paths. The authors of [17] develop a ray tracer which ignores diffraction and scattering and is shown to produce good agreement with measurements. We make the same assumption in our ray tracer and do not model diffraction and scattering. Also, in our ray tracer, transmission through objects (walls, furniture, etc.) is not considered due to high attenuation by materials at 60 GHz [5], [6].

Our ray tracer uses an image-based method [20] to find the multipath. Consider the example of image-based ray tracing for a first-order reflection shown in Fig. 2.2(a). In this method, the transmitter's location P_{TX} is reflected across Wall 1. The reflection of P_{TX} is given by $P_{TX'}$. A line is drawn between $P_{TX'}$ and the receiver's location P_{RX}. The point at which this line intersects Wall 1 is given by P_1 and is the point of reflection. If the line drawn between $P_{TX'}$ and P_{RX} does not intersect Wall 1, the path does not exist. Additionally, if the path between the transmitter and P_1 or between P_1 and the receiver is blocked, the path does not exist. An example of a second-order reflection is given in Fig. 2.2(b).

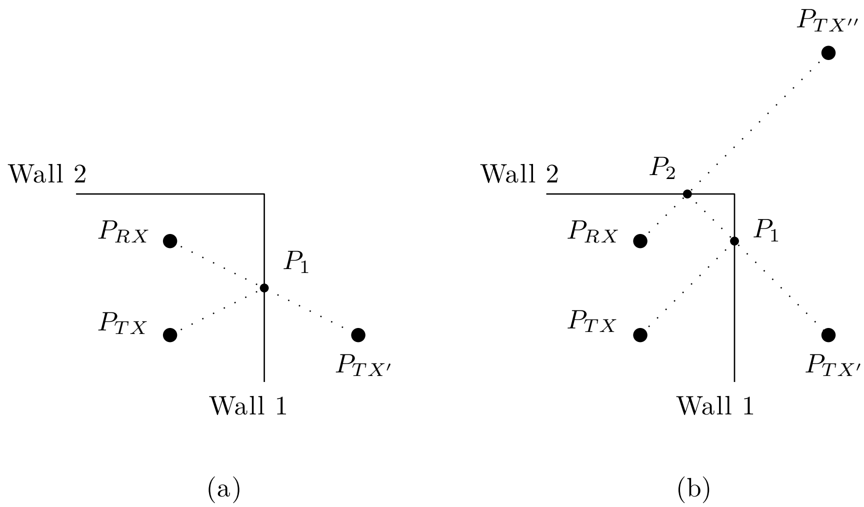

Figure 2.2: Ray tracing example for (a) first-order and (b) second-order reflections

Algorithm 2.1 First-order reflection ray tracing

for $i = 1 \rightarrow numWalls$ **do**
    Reflect P_{TX} across Wall i: $P_{TX'}$
    Find the intersection of Line $\overline{P_{TX'}P_{RX}}$ with Wall i: P_i
    if intersection does not exist **then**
        increment i (path does not exist)
    end if
    Verify Line $\overline{P_iP_{RX}}$ does not intersect any wall other than i
    Verify Line $\overline{P_{TX}P_i}$ does not intersect any wall other than i
    Store points $[P_{TX}\ P_i\ P_{RX}]$
end for

Algorithm 2.2 Second-order reflection ray tracing

for $i_1 = 1 \rightarrow numWalls$ **do**

Reflect P_{TX} across Wall i_1: $P_{TX'}$

for $i_2 = 1 \rightarrow i_1 - 1$ **and** $i_1 + 1 \rightarrow numWalls$ **do**

Reflect $P_{TX'}$ across Wall i_2: $P_{TX''}$

Find the intersection of Line $\overline{P_{TX''}P_{RX}}$ with Wall i_2: P_{i_2}

if intersection does not exist **then**

increment i_2 (path does not exist)

end if

Find the intersection of Line $\overline{P_{TX'}P_{i_2}}$ with Wall i_1: P_{i_1}

if intersection does not exist **then**

increment i_2 (path does not exist)

end if

Verify Line $\overline{P_{i_2}P_{RX}}$ does not intersect any wall other than i_2

Verify Line $\overline{P_{i_1}P_{i_2}}$ does not intersect any wall other than i_1,i_2

Verify Line $\overline{P_{TX}P_{i_1}}$ does not intersect any wall other than i_1

Store points [P_{TX} P_{i_1} P_{i_2} P_{RX}]

end for

end for

Algorithms for finding the first-order reflection paths and second-order reflection paths are given in Algs. 2.1 and 2.2, respectively[1]. The process followed in these algorithms can be extended to higher order reflections. However, we limited the search of our ray tracer to the LOS component and the first- and second-order reflections. This is because measurement results suggest that the power content of higher order reflected paths is negligible [6]. The coordinates of the transmitter, receiver, and reflection points are stored during ray tracing. This information is necessary for calculation of the channel parameters as discussed in the following section.

2.1.2 Extraction of channel parameters

Ray tracing provides a set of paths from the transmitter to the receiver. Using this information, we extract the parameters of the CIR. The mathematical expression for the CIR is

$$h(t) = \sum_{k=0}^{K-1} \alpha_k e^{j\psi_k} \delta(t - \tau_k), \tag{2.1}$$

where K is the number of paths and α_k, τ_k, and ψ_k are the magnitude, time delay, and phase of the kth path, respectively. The calculation of each parameter is discussed in turn.

The magnitude coefficient is comprised of three parts: path loss PL_k, loss due to oxygen absorption OL_k, and reflection loss RL_k. The path loss depends on the path distance as

$$PL_k = \left(\frac{4\pi d_k}{\lambda_c}\right)^2, \tag{2.2}$$

where d_k is the distance traveled by the kth path. Oxygen absorption has been determined to result in a loss of approximately 15 dB/km [17]. Thus, the loss due to oxygen absorption is

$$OL_k = 10^{d_k 1.5/1000}. \tag{2.3}$$

The reflection loss depends on the material that is reflecting the wave (especially the thickness and roughness of the material) as well as the *angle of incidence*. The angle of incidence is

[1]The total number of walls is given by $numWalls$

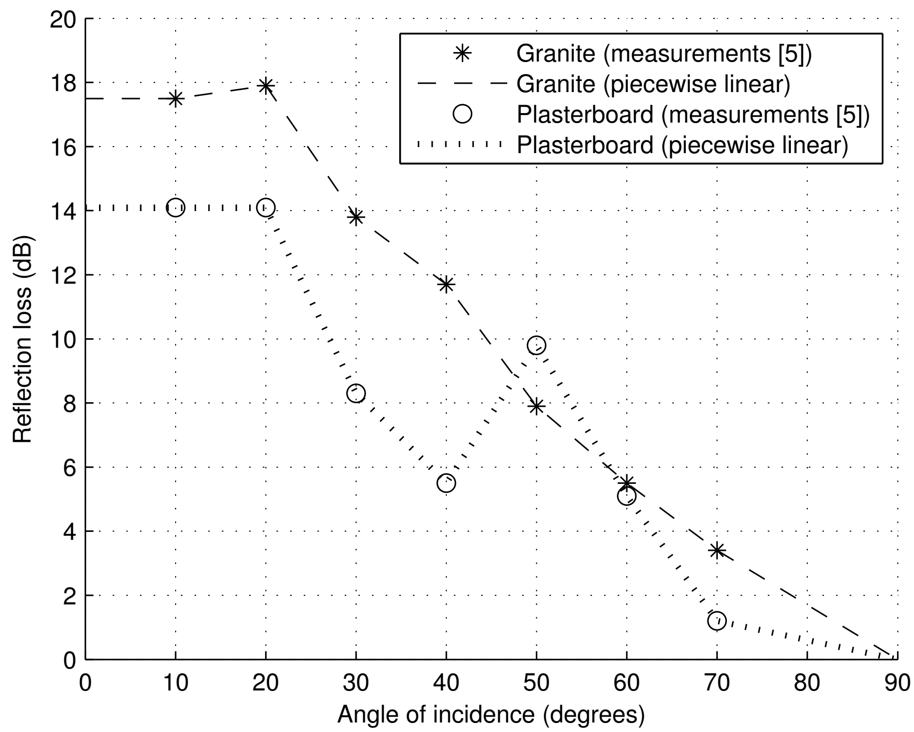

Figure 2.3: Piecewise linear reflection loss model

measured with respect to the normal vector of the wall. The angle is calculated from the coordinates stored during ray tracing.

All surfaces are modeled as granite in the outdoor environment and plasterboard in the indoor environment. We model the reflection loss of these materials based on measurements of reflection loss conducted at 60 GHz [5]. Measured reflection losses taken from [5] for plasterboard and granite are shown with respect to the angle of incidence in Fig. 2.3. We create a piecewise linear reflection loss model from the measured values to determine the loss for angle of incidence in the range [0,90). We assume that the reflection loss at 0 degrees (perpendicular to the surface) is equal to the loss at 10 degrees. Although there is no reflection at 90 degrees, for the purpose of the model, the loss is set to 0 dB. The resulting reflection loss model is shown in Fig. 2.3.

After the three terms are calculated, the kth magnitude coefficient is given by

$$\alpha_k = (PL_k \cdot OL_k \cdot RL_k)^{-1}. \tag{2.4}$$

The paths are sorted by strength in descending order such that the strongest path corresponds to $k = 0$. If a LOS path exists, it will be the path $k = 0$.

We make the assumption that the receiver is synchronized in both time and phase to the strongest multipath component. Thus, we measure the time delay and phase offset with respect to the strongest path. The time delay of the kth path τ_k is found from the difference in distance and the speed of light c as

$$\tau_k = \frac{d_k - d_0}{c}. \tag{2.5}$$

It is useful to break the time delay into an integer and a decimal component based on a single symbol duration T. The delay of each multipath component is defined as an integer multiple of the symbol period η_k and a fractional symbol period ϵ_k where $0 \leq \epsilon_k < 1$. The total time delay is $\tau_k = (\eta_k + \epsilon_k)T$. This leads to the following expression for the CIR

$$h(t) = \sum_{k=0}^{K-1} \alpha_k e^{j\psi_k} \delta(t - (\eta_k + \epsilon_k)T). \tag{2.6}$$

Phase offset arises from excess delay with respect to the strongest (i.e., the synchronous) path as well as from a phase shift of π resulting from each reflection. The phase offset of the kth path is given by

$$\psi_k = (\omega_c \tau_k + \pi N_{refl,k}) \bmod 2\pi, \tag{2.7}$$

where ω_c is the carrier frequency in radians, $N_{refl,k}$ is the number of reflections for the kth path. In (2.7), "mod" is the modulo operator which ensures that the range of ψ_k is $[0, 2\pi)$.

For each path, the angle of departure from the transmitter and the angle of arrival at the receiver is calculated in spherical coordinates. We use ϕ to denote the azimuth angle and θ to denote the inclination angle. The direction of the kth path is given by the pair $(\phi_{t,k},\ \theta_{t,k})$ for the angle of departure at the transmitter and $(\phi_{r,k},\ \theta_{r,k})$ for the angle of arrival at the receiver. The angles are used in Section 2.2 on array theory.

2.1.3 Environments

The outdoor environment is modeled after the academic buildings on the Virginia Tech campus. A 2-dimensional layout of the buildings is shown in Fig. 2.4. The solid lines correspond to the building structure. The nodes are placed inside the dotted perimeter line which corresponds to the road surrounding this portion of the campus. In the 3-dimensional model, the ground surface is level and continuous across the entire layout. The walls extend above the heights of the transmitter and receiver and are flat along the vertical dimension. The name "Urban Canyon" has been given to this type of model [21]. An example multipath channel modeled by the ray tracer is shown in Fig. 2.5.

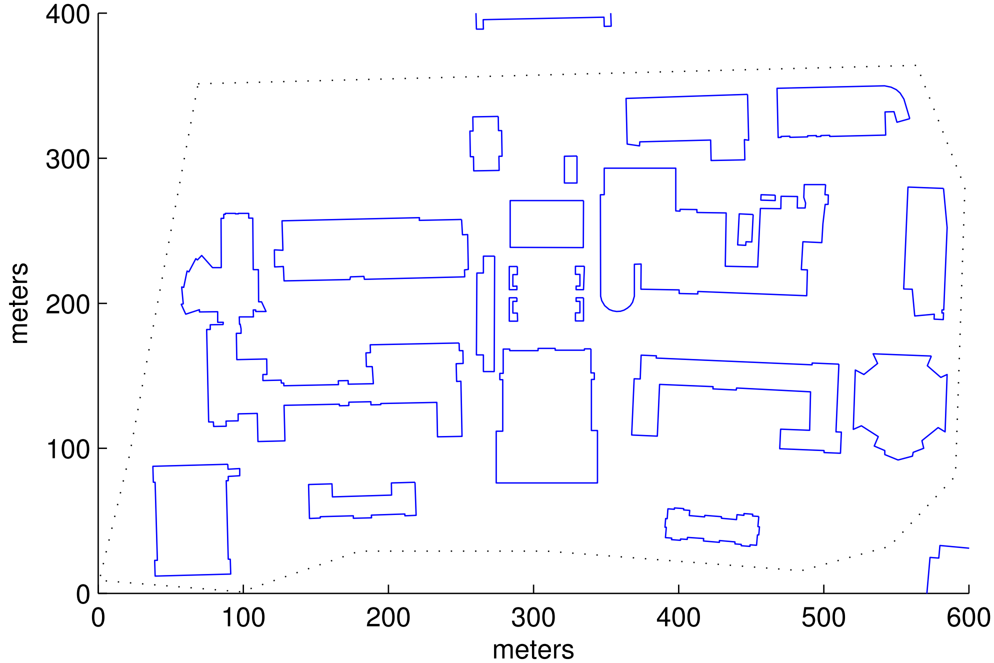

Figure 2.4: Outdoor environment: Virginia Tech campus

We consider the indoor environment when simulating the time varying channel in Chapter 5. A 2-dimensional layout and description of this environment are provided in Section 5.3.

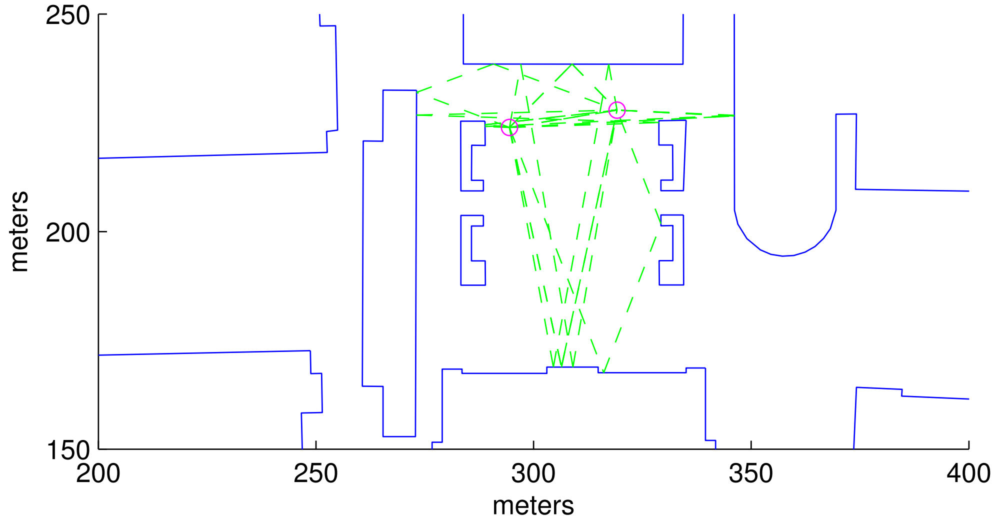

Figure 2.5: Example multipath channel modeled by the ray tracer

2.1.4 Characterization of the outdoor channel

Using ray tracing, we generate 100 000 channel realizations in the outdoor environment at each of 1, 2.5, 5, 7.5, 10, 25, 50, 75, and 100 m distances between the transmitter and receiver. In each channel realization, the transmitter/receiver pair is randomly placed within the perimeter with the requirement that there is a LOS path between them. The height of the nodes is uniformly distributed from 1 to 2 m.

Several representative channel impulse responses are shown in Fig. 2.6: two for a 10 m range and two for a 50 m range. Each of these channels is dominated by the LOS and ground bounce components of the multipath. In each of the 10 m channels, some power separation between the LOS and ground bounce impulses is visible. At a distance of 50 m, the LOS and ground bounce paths visually overlap on the plots. We find that, in general, as the distance between the transmitter and receiver increases, the strength of the ground bounce and other reflected paths increases relative to that of the LOS path. This is particularly true of the ground bounce where, as range is increased, the channel gain and time delay approach that of the LOS.

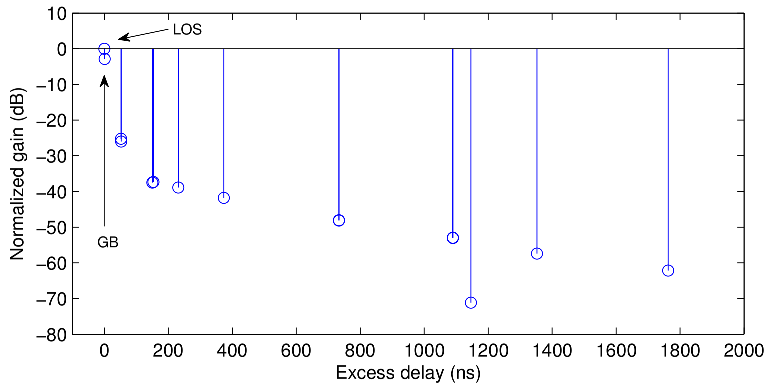

(a) First CIR at 10m

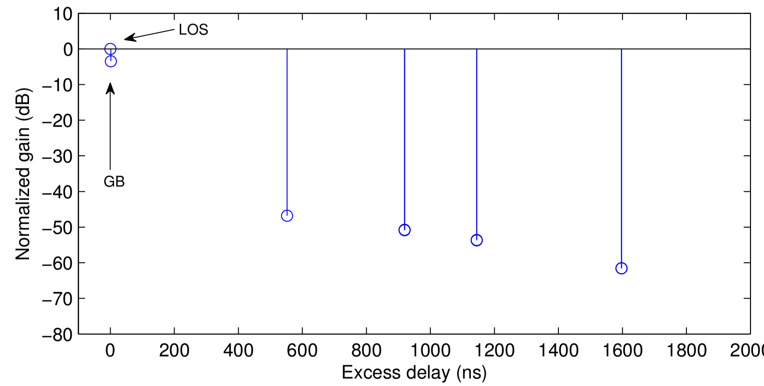

(b) Second CIR at 10m

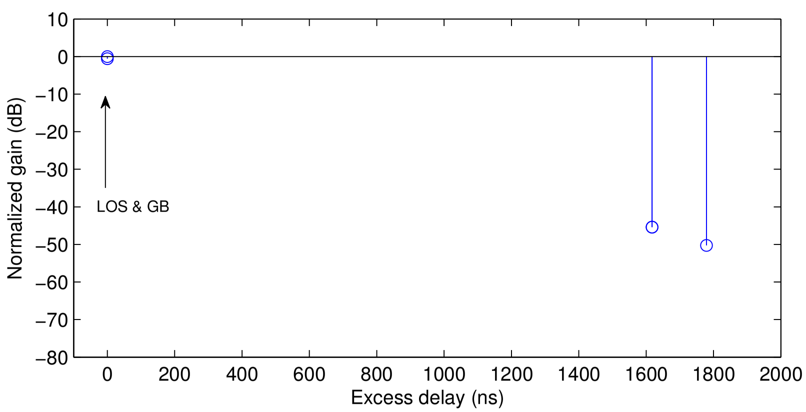

(c) First CIR at 50m

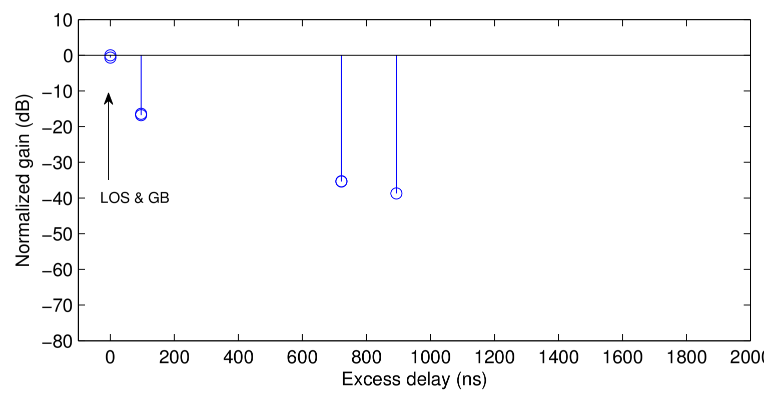

(d) Second CIR at 50m

Figure 2.6: Four representative channel impulse responses for the outdoor environment

Three characteristics of the ray tracing results are presented: the power content, delay spread, and phase distribution. The purpose is to verify the ray tracer and to provide useful information about the channel characteristics for subsequent chapters.

- **Power content** We desire to have a measure of the number of paths required to represent a given percentage of the received power. Fig. 2.7 displays the probability that 99% of the total received power is contained within a given number of paths.

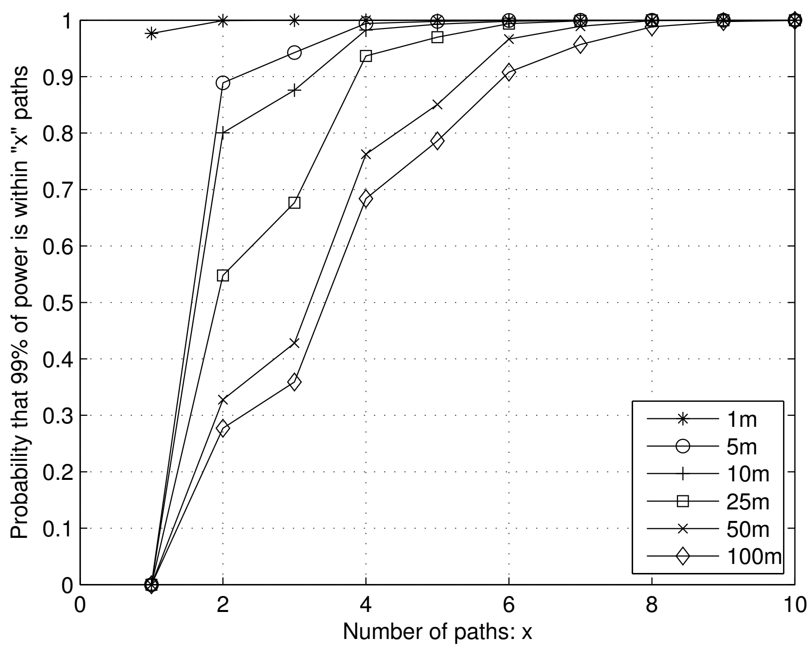

Figure 2.7: Power content for several ranges in the outdoor environment

- **Delay Spread** The RMS delay spread σ_T is a statistic for the time dispersion of the multipath. The definition is taken from [11] and is given by

$$\sigma_T = \sqrt{\bar{\tau^2} - (\bar{\tau})^2}, \tag{2.8}$$

where $\bar{\tau}$ and $\bar{\tau^2}$ are defined as

$$\bar{\tau} = \frac{\sum_{k=0}^{K-1} \alpha_k^2 \tau_k}{\sum_{k=0}^{K-1} \alpha_k^2} \tag{2.9}$$

and

$$\bar{\tau^2} = \frac{\sum_{k=0}^{K-1} \alpha_k^2 \tau_k^2}{\sum_{k=0}^{K-1} \alpha_k^2}, \tag{2.10}$$

respectively. The cumulative distribution function (CDF) of delay spread for four ranges is plotted in Fig. 2.8. Included in these plots is the delay spread for two subsets of the paths. This provides an indication of the influence that the weaker paths have on the delay spread values. Table 2.1 summarizes the delay spread distributions for the set of ranges considered.

Delay spreads of 10–25 ns are common for distances of 25 m and above. Therefore, the coherence bandwidth for these channels is on the order of 10 MHz. The anticipated bandwidth of signals in the 60 GHz band is 1-2 GHz. Thus, the channel in the outdoor environment is frequency selective.

Equalization and OFDM are two techniques designed to compensate for frequency selective channels [22]. Equalization is commonly accomplished employing a linear filter and optimized based on the peak distortion criterion or the minimum mean square error (MMSE) criterion [22]. OFDM divides the available band among multiple orthogonal sub-carriers each of which is effectively transmitted over a frequency-flat channel. OFDM is included in the proposal specification for 60 GHz WLANs [12] in addition to the single carrier physical layer specifications. In this thesis, our focus is on array processing for single carrier systems. We investigate the ability of antenna arrays and array processing to mitigate ISI in the outdoor environment in Chapters 3 and 4. Another multi-antenna method worth mentioning is space-time equalization, which provides resolution in space through the use of an array and resolution in time through the use of a linear filter per antenna element [23]. The space-time equalizer is capable of achieving performance gains over array processing and channel equalization performed separately [23].

We compare our delay spread distribution with that of measurements made at 60 GHz for city streets and squares [13]. Results from [13] are summarized in Table 2.1. The width of the city streets varied from 13 to 36 m and the dimensions of the city squares varied from 70 to 100 m. The dimensions of the open spaces on the Virginia Tech campus fall in between that of the streets and squares. In [13], example transmission distances of 13 to 90 m are cited for the city streets. Assuming that this is representative of all of the city street and square measurements, it is comparable to the distances which we consider. Our delay spread values fall in between the measured values. Thus, to the extent that RMS delay spread captures the effects of ISI in the multipath channel, we expect the results presented in the following chapters to be applicable to real-world channels such as those measured in [13].

- **Phase distribution** The phase of the strongest path is always zero due to the assumption of phase synchronization. As expected, the distribution of the phase for all other paths is observed to be uniform over the interval $[0, 2\pi)$. As range increases, the phase offset of the ground bounce remains uniformly distributed while the magnitude coefficient and time delay approach that of the LOS. Thus, the ground bounce is a source of deep fades in the overall received power.

2.2 Phased array antennas

Antenna arrays are comprised of a number of antenna elements designed to provide spatial resolution to the transmission and reception of signals. The receiver's array spatially samples the propagation environment providing the array processor the ability to discriminate be-

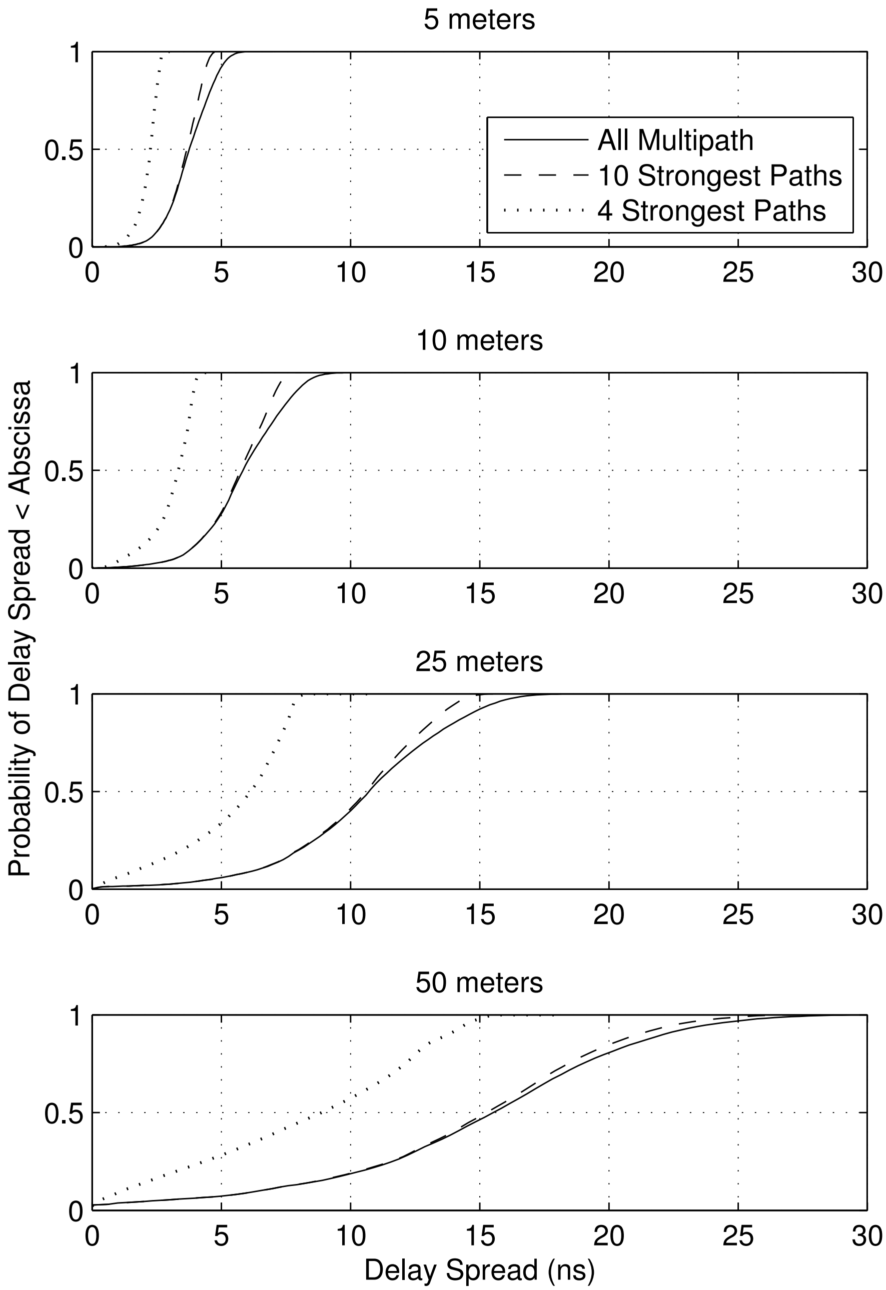

Figure 2.8: CDF of delay spread for four ranges in the outdoor environment

Table 2.1: 50% and 90% values of the cumulative distribution of delay spread outdoors.

Environment	Range (m)	50% (ns)	90% (ns)
Virginia Tech campus	1	1.00	1.26
	2.5	2.32	2.92
	5	3.78	4.97
	7.5	4.86	6.48
	10	5.94	7.92
	25	10.80	14.80
	50	15.84	22.44
	75	18.86	27.47
	100	20.16	31.20
	All	5.28	21.60
City Street [13]: mean [min–max]	13–90	5.54 [3.6–8.4]	17.83 [6.5–48.3]
City Square [13]: mean [min–max]		31.74 [20.1–40.8]	73.58 [55.2–92.2]

tween signals originating from different directions. In a complementary way, a transmitter's antenna array is able to control the strength of transmission as a function of the direction of transmission.

Many different array geometries are considered in the literature [24]. For phased array antennas it is desirable to have a relatively small inter-element spacing so that the received signal at each element is highly correlated. This work deals with uniform linear arrays and uniform planar arrays with inter-element spacings of $\lambda_c/2$. In this section, array theory pertaining to this work is covered. This provides both the theoretical background and the notation used in subsequent chapters.

2.2.1 Receiver array

In this section, the response of an array to a signal arriving from an arbitrary direction (ϕ, θ) is derived. The direction is given in spherical coordinates where ϕ is the azimuth angle and θ is the inclination angle. Fig. 2.9 shows the location of each element in a linear array with $N_r = 5$ elements. A signal is depicted arriving from azimuth direction ϕ ($\theta = 0$). As a result of the small inter-element spacing, signals are modeled as plane waves perpendicular to the direction of travel. We define the signal at the origin of the coordinate system to be[2]

$$\Re\{r(t)e^{j\omega_c t}\} \tag{2.11}$$

where $r(t)$ is the baseband signal and ω_c is the carrier frequency in radians. The received signal in the nth antenna element is time shifted with respect to the signal given in (2.11) and is written as $\Re\{r(t-\rho_n)e^{j\omega_c(t-\rho_n)}\}$. The time shift for the nth element ρ_n is determined by the time of arrival of the wavefront at the nth antenna element with respect to the origin. The projection (i.e., the inner product) of the nth element's position vector $\mathbf{p}_n$ onto the direction vector of the signal $\mathbf{a}$ gives the distance that the wavefront travels between the nth element and the origin. Thus, the time shift is equal to[3]

$$\rho_n = \frac{\mathbf{p}_n^T \cdot \mathbf{a}}{c}, \tag{2.12}$$

where the position vector and signal direction vector are defined as

$$\mathbf{p}_n = \begin{bmatrix} p_{n_x} \\ p_{n_y} \\ p_{n_z} \end{bmatrix} \text{ and} \tag{2.13}$$

$$\mathbf{a} = \begin{bmatrix} -\sin(\theta)\cos(\phi) \\ -\sin(\theta)\sin(\phi) \\ -\cos(\theta) \end{bmatrix}, \tag{2.14}$$

respectively, and c is the speed of light. The wavefront may arrive at the nth element before or after arriving at the origin of the coordinate system. Thus, ρ_n may be positive or negative.

---

[2] $\Re$ denotes the real part of the argument

[3] superscript T denotes *transpose*

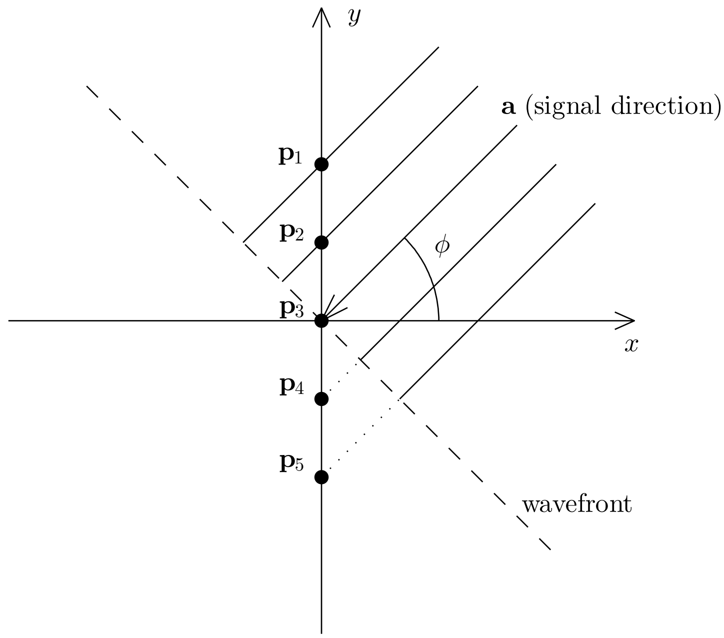

Figure 2.9: Linear array in the x-y plane with a plane wave signal

It is desirable to use baseband representation throughout the remainder of this chapter. The signal in the nth element in terms of the baseband representation is $r_n(t) = r(t - \rho_n)e^{-j\omega_c \rho_n}$. Let the bold typeset $\mathbf{r}(t)$ be a column vector of the received signals in each antenna element,

$$\mathbf{r}(t) = \begin{bmatrix} r_1(t) \\ r_2(t) \\ \vdots \\ r_n(t) \\ \vdots \\ r_{N_r}(t) \end{bmatrix}. \tag{2.15}$$

Although signals at 60 GHz have large bandwidth (for example, the IEEE's proposal specification for 802.11ad defines a signal bandwidth of 2.16 GHz [12]), they are assumed to be narrowband in regard to the array. This is because the baseband signal $r(t)$ is changing relatively slowly with respect to the time delays. The time bandwidth product (TBWP) is a key metric in determining whether the signal is narrowband with respect to the array. The narrowband assumption is valid for $TBWP << 1$ [25] where time is the time delay across the array aperture. Consider a system with a six by six antenna array with element spacings of $\lambda_c/2$ and a signal bandwidth of 2.16 GHz. For this system, the maximum TBWP is 0.13 when the signal crosses the diagonal of the array. Thus, the approximation is valid for communication systems anticipated for the 60 GHz band.

The narrowband assumption allows the simplification $r(t - \rho_n) \approx r(t)$ to be made. The result is a *phased array antenna* where the signal in each element experiences a phase shift as the signal crosses the array as given by $r_n(t) = r(t)e^{-j\omega_c\rho_n}$. This simplification is further supported by the use of phased array antennas in the 60 GHz band. For example, the IEEE TGad standard group [12] and Sibeam (now owned by Silicon Image) are two examples of groups working with phased array antennas at 60 GHz.

A new vector $\mathbf{v}_r$ is defined which contains the phase shifts for each element of the receiver's array. This vector, called the *array vector*, is expressed as

$$\mathbf{v}_r = \begin{bmatrix} e^{-j\omega_c\rho_1} \\ e^{-j\omega_c\rho_2} \\ \vdots \\ e^{-j\omega_c\rho_n} \\ \vdots \\ e^{-j\omega_c\rho_{N_r}} \end{bmatrix}. \tag{2.16}$$

Using (2.16), the signal in each array element can be written simply as

$$\mathbf{r}(t) = r(t)\mathbf{v}_r. \tag{2.17}$$

2.2.2 Transmitter array

At the transmitter, the theory is complementary. We are now interested in the transmission of the signal in a particular direction. In the far field the signal can be modeled as a plane wave. Let the column vector $\mathbf{z}(t)$ denote the signal being transmitted by each array element. By working with the geometry of the array, it can be shown that for a signal transmitted in direction $(\phi,\ \theta)$ the time shifts are identical to the time shifts experienced by a signal arriving from the same direction. Thus, the definitions in (2.12), (2.13), (2.14), and (2.16) are valid for the transmitter's array vector $\mathbf{v}_t$. In the direction $(\phi,\ \theta)$ the signal from each antenna element sums as follows:

$$\mathbf{v}_t^T\mathbf{z}(t) = \begin{bmatrix} e^{-j\omega_c\rho_1} \ e^{-j\omega_c\rho_2} \ \cdots \ e^{-j\omega_c\rho_{N_t}} \end{bmatrix} \begin{bmatrix} z_1(t) \\ z_2(t) \\ \vdots \\ z_{N_t}(t) \end{bmatrix}. \tag{2.18}$$

2.2.3 Incorporating arrays into the channel model

Each multipath component has a unique direction with respect to the transmitter and the receiver. In order to express this mathematically, we incorporate the array vectors into the CIR expression of (2.6) as

$$\mathbf{H}(t) = \sum_{k=0}^{K-1} \mathbf{v}_{r,k}\mathbf{v}_{t,k}^T \alpha_k e^{j\psi_k}\delta(t-(\eta_k+\epsilon_k)T), \tag{2.19}$$

where the receiver and transmitter array vectors for the kth multipath are denoted $\mathbf{v}_{r,k}$ and $\mathbf{v}_{t,k}$, respectively. The resulting CIR $\mathbf{H}(t)$ is a $N_r \times N_t$ matrix which describes all channel specific information for the system model. We often work with the receiver's array only. In this case, the CIR can be written as

$$\mathbf{h}(t) = \sum_{k=0}^{K-1} \mathbf{v}_{r,k}\alpha_k e^{j\psi_k}\delta(t-(\eta_k+\epsilon_k)T). \tag{2.20}$$

2.2.4 Array processing

Array processing theory is covered in depth in Chapter 4. However, for the sake of completeness, a brief introduction is provided in this chapter. It has been shown that the direction of the signal corresponds to time shifts on the arrays. In order to control the response of the array and array processor in a particular direction, the array processor could introduce time shifts to the signal on each antenna element. Due to the narrowband assumption, the time shifts reduce to phase shifts. As shown in Fig. 2.1, the array processor multiplies the signal in each branch of the transmitter or receiver by a complex weight. The weight vector for the transmitter and receiver arrays are defined as

$$\mathbf{w}_t^* = \begin{bmatrix} w_{t,1}^* \\ w_{t,2}^* \\ \vdots \\ w_{t,N_t}^* \end{bmatrix} \qquad \text{and} \qquad \mathbf{w}_r^* = \begin{bmatrix} w_{r,1}^* \\ w_{r,2}^* \\ \vdots \\ w_{r,N_r}^* \end{bmatrix}, \tag{2.21}$$

respectively. In general, the complex weights allow for magnitude and phase adjustment of the signal in each branch.

2.3 Mathematical formulation

The system model at baseband is defined in this section. We implement BPSK and QPSK modulation schemes with unit power symbols y_m. A square root raised cosine pulse $p(t)$ normalized to unit energy is used to shape the symbols. The signal from the modulator is written as

$$q(t) = \sum_{m=-\infty}^{\infty} y_m p(t - mT). \tag{2.22}$$

The signal transmitted by each array element is given by $\mathbf{z}(t) = q(t)\mathbf{w}_t^*$. Utilizing the CIR defined in (2.19) produces the vector $\mathbf{r}(t)$ of the signal received by each array element,

$$\begin{aligned}\mathbf{r}(t) &= (\mathbf{H} * \mathbf{z})(t) + \mathbf{n}(t) \\ &= \sum_{k=0}^{K-1} \sum_{m=-\infty}^{\infty} \mathbf{v}_{r,k}\mathbf{v}_{t,k}^T \mathbf{w}_t^* \alpha_k e^{j\psi_k} y_m p(t - (m + \eta_k + \epsilon_k)T) + \mathbf{n}(t), \end{aligned} \tag{2.23}$$

where the noise $\mathbf{n}(t)$ is assumed to be a vector of complex Gaussian random processes. The noise in each branch is also assumed to be independent.

We define the signal after matched filtering to be

$$\begin{aligned}\mathbf{x}(t) &= (\mathbf{r} * p)(t) \\ &= \int_{-\infty}^{\infty} \sum_{k=0}^{K-1} \sum_{m=-\infty}^{\infty} \mathbf{v}_{r,k}\mathbf{v}_{t,k}^T \mathbf{w}_t^* \alpha_k e^{j\psi_k} y_m p(t - \tau - (m + \eta_k + \epsilon_k)T) p(\tau) d\tau \\ &\quad + \int_{-\infty}^{\infty} \mathbf{n}(\tau) p(t - \tau) d\tau \\ &= \sum_{k=0}^{K-1} \mathbf{v}_{r,k}\mathbf{v}_{t,k}^T \mathbf{w}_t^* \alpha_k e^{j\psi_k} \sum_{m=-\infty}^{\infty} y_m \int_{-\infty}^{\infty} p(t - \tau - (m + \eta_k + \epsilon_k)T) p(\tau) d\tau \\ &\quad + \int_{-\infty}^{\infty} \mathbf{n}(\tau) p(t - \tau) d\tau. \end{aligned} \tag{2.24}$$

In the frequency domain the pulse convolution can be seen as

$$\begin{aligned}\mathcal{F}\left\{\int_{-\infty}^{\infty} p(t - \tau - (m + \eta_k + \epsilon_k)T) p(\tau) d\tau\right\} &= \mathcal{F}\left\{p(t - (m + \eta_k + \epsilon_k)T) * p(t)\right\} \\ &= P(f)P(f)e^{-j\omega_c(m+\eta_k+\epsilon_k)T} \\ &= G(f)e^{-j\omega_c(m+\eta_k+\epsilon_k)T}, \end{aligned} \tag{2.25}$$

where $P(f)$ is the Fourier transform of the square root raise cosine pulse $p(t)$ and $G(f)$ is the Fourier transform of the raised cosine pulse $g(t)$ defined as

$$g(t) = \operatorname{sinc}\left(\frac{t}{T}\right) \frac{\cos(\pi\beta t/T)}{1 - 4\beta^2 t^2/T^2}, \tag{2.26}$$

where β is the roll-off factor. Transforming (2.25) back to the time domain results in $g(t - (m + \eta_k + \epsilon_k)T)$. Substituting the result of the convolution into (2.24) and sampling at the symbol rate T, the received signal at the lth time instant is given by

$$\mathbf{x}(l) = \sum_{k=0}^{K-1} \mathbf{v}_{r,k}\mathbf{v}_{t,k}^T\mathbf{w}_t^*\alpha_k e^{j\psi_k} \sum_{m=-\infty}^{\infty} y_m g((l-m-\eta_k-\epsilon_k)T) + \mathbf{n}'(l), \tag{2.27}$$

where $\mathbf{n}'(l) = \int_{-\infty}^{\infty} \mathbf{n}(\tau)p(lT-\tau)d\tau$. In (2.27), $\mathbf{n}'(l)$ is a vector of independent identically distributed (i.i.d.) circularly symmetric complex Gaussian random variables defined by $\mathcal{N}(\mathbf{0}, N_0\mathbf{I})$ where N_0 is the variance of each component of $\mathbf{n}'(l)$. Thus, the in-phase and quadrature components of $\mathbf{n}'(l)$ have variance $N_0/2$. In subsequent equations, the sample index (l) will be removed and it will be assumed that $\mathbf{x}$ and $\mathbf{n}'$ represent the lth sample.

A new variable s_k is defined as

$$s_k = \alpha_k e^{j\psi_k} \sum_{m=-\infty}^{\infty} y_m g((l-m-\eta_k-\epsilon_k)T). \tag{2.28}$$

Substitution of s_k into (2.27) produces

$$\mathbf{x} = \sum_{k=0}^{K-1} \mathbf{v}_{r,k}\mathbf{v}_{t,k}^T\mathbf{w}_t^* s_k + \mathbf{n}'. \tag{2.29}$$

The output of the receiver's array processor provides a decision metric for detection and is labeled $\hat{y}$. The expression for the decision metric is[4]

$$\begin{aligned}\hat{y} &= \mathbf{w}_r^H \left[\sum_{k=0}^{K-1} \mathbf{v}_{r,k}\mathbf{v}_{t,k}^T\mathbf{w}_t^* s_k + \mathbf{n}'\right] \\ &= \sum_{k=0}^{K-1} \mathbf{w}_r^H\mathbf{v}_{r,k}\mathbf{v}_{t,k}^T\mathbf{w}_t^* s_k + \mathbf{w}_r^H\mathbf{n}'.\end{aligned} \tag{2.30}$$

When working with the receiver array the notation can be simplified by incorporating $\mathbf{v}_{t,k}^T\mathbf{w}_t^*$ into the channel gains α_k in (2.28). This produces

$$\hat{y} = \sum_{k=0}^{K-1} \mathbf{w}_r^H\mathbf{v}_{r,k} s_k + \mathbf{w}_r^H\mathbf{n}'. \tag{2.31}$$

We now have two expressions for decision metric $\hat{y}$. Often the transmitter's weights will be fixed and we will seek to optimize the performance at the receiver. Thus, the expression in

[4]superscript H denotes *complex conjugate transpose*

(2.31) will be used frequently. When the term $\mathbf{v}_{t,k}^T \mathbf{w}_t^*$ is incorporated into the channel gains, the received signal vector $\mathbf{x}$ is expressed

$$\mathbf{x} = \sum_{k=0}^{K-1} \mathbf{v}_{r,k} s_k + \mathbf{n}'. \tag{2.32}$$

2.3.1 Calculation of the probability of a bit error

To determine the probability of a bit error P_b, we calculate the probability of incorrectly detecting a data bit from the strongest multipath component. Recall that in Section 2.1.2 we assume synchronization with the strongest path. For ease of analysis, the decision metric $\hat{y}$ defined in (2.30) is divided into two parts. The first is the information component $\hat{y}_{\mathrm{i}}$ which is comprised of the received multipath signal. The second part is the noise component $\hat{y}_{\mathrm{n}}$.

We consider two cases where the bit error probability is desired. The first is when we desire to calculate P_b for a particular channel realization. In this case, the channel parameters are deterministic. The transmitted symbols and noise are treated as random variables and the probability of a bit error is determined with respect to the transmitted symbols. This is accomplished by calculating the probability of a bit error given each transmitted symbol sequence $\mathbf{y}$ which we denote $P_{b|\mathbf{y}}$ and then taking the mean.

The noise component of the decision metric is a weighted sum of the noise samples from the array elements. Thus, $\hat{y}_{\mathrm{n}}$ is a zero-mean Gaussian random variable with variance

$$\sigma_{\hat{y}_{\mathrm{n}}}^2 = E[|\mathbf{w}_r^H \mathbf{n}'|^2] = \mathbf{w}_r^H E[\mathbf{n}' \mathbf{n}'^H] \mathbf{w}_r = N_0(\mathbf{w}_r^H \mathbf{w}_r). \tag{2.33}$$

The noise $\hat{y}_{\mathrm{n}}$ is complex valued with independent in-phase and quadrature components of equal power. Thus, the in-phase and quadrature components of the noise both have variance

$$\sigma_{\hat{y}_{\mathrm{n,I}}}^2 = \sigma_{\hat{y}_{\mathrm{n,Q}}}^2 = \frac{N_0}{2}(\mathbf{w}_r^H \mathbf{w}_r). \tag{2.34}$$

For BPSK modulation our only concern is the in-phase components. For a particular sequence of transmitted symbols $\mathbf{y}$, the expression for the probability of a bit error is given by

$$
\begin{aligned}
P_{b|\mathbf{y}} &= \frac{1}{2}\mathrm{erfc}\left(\frac{\mathrm{Re}\{\hat{y}_{\mathrm{i}}\}}{\sqrt{2\sigma^2_{\hat{y}_{\mathrm{n,I}}}}}\right) \\
&= \frac{1}{2}\mathrm{erfc}\left(\frac{\mathrm{Re}\{\hat{y}_{\mathrm{i}}\}}{\sqrt{N_0(\mathbf{w}_r^H\mathbf{w}_r)}}\right).
\end{aligned} \tag{2.35}
$$

Substituting $\mathrm{Re}\{\hat{y}_{\mathrm{i}}\} = \sqrt{E_b}$ and $\mathbf{w}_r^H\mathbf{w}_r = 1$ into (2.35) it can be verified that for an AWGN channel and no antenna array, (2.35) is equivalent to the well known expression for the bit error probability of optimally detected antipodal signaling [22]. The expected bit error probability is then

$$
P_b = \frac{1}{2^{|\mathbf{y}|}}\sum_{\mathbf{y}} P_{b|\mathbf{y}}, \tag{2.36}
$$

where $|\mathbf{y}|$ is the number of symbols which contribute to the metric $\hat{y}_{\mathrm{i}}$.

The probability of a bit error expression for QPSK treats the in-phase and quadrature components separately and is given by

$$
\begin{aligned}
P_b &= \frac{1}{4^{|\mathbf{y}|}}\sum_{\mathbf{y}} P_{b|\mathbf{y}} \\
&= \frac{1}{4^{|\mathbf{y}|}}\sum_{\mathbf{y}} \frac{1}{4}\mathrm{erfc}\left(\frac{\mathrm{Re}\{\hat{y}_{\mathrm{i}}\}}{\sqrt{N_0(\mathbf{w}_r^H\mathbf{w}_r)}}\right) + \frac{1}{4}\mathrm{erfc}\left(\frac{\mathrm{Im}\{\hat{y}_{\mathrm{i}}\}}{\sqrt{N_0(\mathbf{w}_r^H\mathbf{w}_r)}}\right).
\end{aligned} \tag{2.37}
$$

We assume Gray coding for QPSK. Thus, a detection error in the in-phase component leads to incorrect detection of one of the two bits. The same is true for the quadrature component.

In the second case, we desire to know the expected bit error probability for an arbitrary channel. We obtain the bit error probability by averaging over multiple channel realizations. The channel parameters are treated as deterministic for each realization. For instance, to determine the performance of the link at a distance of 25 m, we average P_b over 100 000 channel realizations with this range. For each channel realization, P_b is calculated with (2.35) and (2.37).

Chapter 3

Preliminary Study of Outdoor 60 GHz Band Communication

This chapter provides a preliminary study of link performance outdoors. The bit error probability of outdoor links in the 60 GHz band is evaluated using the outdoor environment developed in Chapter 2: the Virginia Tech campus. Although mobility is not directly considered in this chapter, we perform simulations with randomly placed nodes. This is intended to model ad hoc networks such as might be encountered in public safety and military applications.

This chapter builds upon existing research into outdoor use of the 60 GHz band. Studies of the feasibility and performance of outdoor links in the 60 GHz band include [10], [13], [19], and [26]. Specifically, in [26], wideband measurements of the 60 GHz channel are used to determine path loss and delay spread in an outdoor peer-to-peer environment. In [10], ray tracing is used to deterministically characterize the channel, and the feasibility of soldier to soldier mobile ad hoc networks in the 60 GHz band is analyzed. In [19], the capacity of links between stationary devices in an outdoor mesh network is studied. In [13], measurements and deterministic modeling are used to study propagation at 60 GHz. The authors of [13] provide an evaluation of initial transmission performance for indoor high data rate transmission. Several techniques for countering delay spread as a result of multipath are considered in [13] including Direct Sequence Spread Spectrum with a RAKE receiver, multicarrier modulation, antenna diversity, and adaptive equalization.

Beamsteering (also known as classical beamforming or maximum directivity beamforming) is the method of array processing for this chapter and is presented in Section 3.1. Antenna arrays increase the directivity of the signal in order to provide gain and as a result we expect a reduction in ISI due to multipath. Using beamsteering, we evaluate the ability of four different antenna array geometries to mitigate ISI in Section 3.2. In Section 3.3, a link budget is setup and the performance is evaluated versus the range between the transmitter and receiver. We find that ISI rather than additive noise becomes the limiting factor as the range of transmission increases. From the results of this chapter, direction is given for the work that follows in Chapters 4 and 5.

3.1 Beamsteering

In the simulations that follow, we use a method of array processing known as beamsteering in which the main beam of the array pattern is directed toward the LOS path [24]. On the transmitter's side, beamsteering provides weights which cause the signal transmitted by each array element to constructively sum in the direction of the LOS path. Similarly, on the receiver's side, the weights given by beamsteering constructively sum the signal arriving from the LOS path. In order to accomplish this, the array weights are set equal to the array vectors of the LOS path as given by [24]

$$\mathbf{w}_t = \frac{1}{N_t}\mathbf{v}_{t,0} \qquad \text{and} \tag{3.1}$$

$$\mathbf{w}_r = \frac{1}{N_r}\mathbf{v}_{r,0}. \tag{3.2}$$

The factors $1/N_t$ and $1/N_r$ normalize the weight vectors so that $||\mathbf{w}_t|| = 1$ and $||\mathbf{w}_r|| = 1$. For both the transmitter and the receiver, the response of the array in the direction of the

LOS path is given by

$$\frac{1}{N_t}\mathbf{v}_{t,0}^H\mathbf{v}_{t,0} = \frac{1}{N_r}\mathbf{v}_{r,0}^H\mathbf{v}_{r,0} = 1. \tag{3.3}$$

It can be shown that the transmitter's array provides a power gain of N_t in the direction of the LOS path. Let the power of the signal from the modulator $q(t)$ be given by P_q. After multiplication with the complex weights of (3.1), the vector of the signals applied to the array is given by $\mathbf{w}_t^H q(t) = \frac{1}{N_t}\mathbf{v}_{t,0}^H q(t)$ with the power in the nth element given by

$$P_n = \lim_{T\to\infty}\frac{1}{T}\int_{-T/2}^{T/2}\left|\frac{1}{N_t}e^{-j\omega_c\rho_n}q(t)\right|^2 dt = \frac{1}{N_t^2}\lim_{T\to\infty}\frac{1}{T}\int_{-T/2}^{T/2}|q(t)|^2\,dt = \frac{P_q}{N_t^2}. \tag{3.4}$$

The total transmitted power is given by the sum of the power in each element $\sum_{n=1}^{N_t} P_n = P_q/N_t$. From (3.3), it follows that the signal in the direction of the LOS path is $q(t)$. As noted, the power of $q(t)$ is P_q and the ratio of power transmission in the direction of the LOS to total power transmission is $\frac{P_q}{P_q/N_t} = N_t$.

As is shown in (2.33), noise power at the output of the receiver's array is scaled by

$$\mathbf{w}_r^H\mathbf{w}_r = \frac{1}{N_r^2}\mathbf{v}_{r,0}^H\mathbf{v}_{r,0} = \frac{1}{N_r^2}N_r = \frac{1}{N_r}. \tag{3.5}$$

The array response in the direction of the LOS component is shown to be 1 in (3.3). Therefore, the LOS signal to noise ratio (SNR) is multiplied by a factor of N_r due to the receiver's array.

It is shown in Section 4.1.2 that given an additive white Gaussian noise (AWGN) channel, beamsteering is known to maximize the SNR. In our case beamsteering will maximize the ratio between the power of the LOS path and noise. In the context of beamsteering we consider all multipath components other than the LOS to be interference. Although, beamsteering does not explicitly take into account the interference, we expect to see a reduction in the strength of these paths because their angles of arrival are different from that of the LOS path.

3.2 Performance in multipath

In order to measure the ability of phased array antennas to provide adequate performance in outdoor 60 GHz networks, we simulate the probability of a bit error. The ray tracer and outdoor environment described in Chapter 2 are used to provide LOS multipath channel parameters at 60 GHz. Pairs of nodes are placed randomly in the layout with ranges of 1, 2.5, 5, 7.5, 10, 25, 50, 75, and 100 meters. The height of the nodes is varied between 1 and 2 meters to model the height of a handheld device. At each range, 100 000 channel realizations are generated in order to determine the average probability of a bit error. The four strongest paths are used in calculations and the SRRC pulse is truncated to four symbol periods (i.e. the interval $-2T \leq t \leq 2T$). The modulation scheme is BPSK, the data rate is 1 Gbps, and the roll-off factor is 0.25.

The following antenna arrays are considered in this simulation:

- Six element vertical linear array (6×1)
- Six element horizontal linear array (1×6)
- Sixteen element vertical planar array (4×4)
- Thirty-six element vertical planar array (6×6)

The array elements are uniformly spaced at a distance of $\lambda_c/2$. We assume that the array elements are isotropic radiators.

The probability of a bit error with respect to E_b/N_0 is presented for ranges of 5, 10, 25, and 50 meters in Figs. 3.1–3.4, respectively. Noise power N_0 is measured *after* the receiver's array processor[1]. In this way the array gain over AWGN is ignored, allowing us to compare the performance of the four arrays in terms of their ability to mitigate ISI. The received

[1]The term N_0 in this chapter represents $N_0(\mathbf{w}_r^H\mathbf{w}_r)$ from Chapter 2

energy per bit is measured before the array processor and is given by

$$E_b = \frac{1}{\log_2 M} \sum_{k=0}^{K-1} \alpha_k^2 \tag{3.6}$$

where M is the modulation order.

From Fig. 3.1, it is observed that the planar arrays demonstrate similar performance at shorter range. The six by six planar array demonstrates a more substantial improvement over the four by four array at ranges of 10 and 25 m. The horizontal linear array is outperformed by the vertical linear array at all four ranges. This indicates that interference due to the ground bounce is more significant than interference from the surrounding buildings. In fact, the vertical linear array outperforms the four by four planar array for $E_b/N_0 < 11$ dB at 10 m and for all values of E_b/N_0 at 25 m. As shown in Fig. 3.2, at a range of 10 m there is an inversion between the vertical linear array and the four by four planar array. At lower values of E_b/N_0, the vertical linear array has better performance because of its ability to mitigate the ground bounce path which is always present. However, as the value of E_b/N_0 increases, the vertical array becomes interference limited more quickly due to a small percentage of channel realizations in which strong interference occurs from buildings.

The link at all ranges is interference limited and at ranges of 50 meters and greater the link becomes severely limited by interference to the point that all four arrays are incapable of mitigating the interference through beamsteering. This is primarily due to interference from the ground bounce. This result is anticipated in Section 2.1.4 where the CIRs given in Figs. 2.6c and 2.6d show that at 50 m the ground bounce is on the same order of magnitude as the LOS. As range increases, the difference between the arrival angles of the LOS and ground bounce paths decreases and the ground bounce is not mitigated by the arrays.

Because the link performance is interference limited, increasing the transmit power will not be sufficient for improving the link performance outdoors. In order for beamsteering to be more effective, increased resolution along the vertical axis (i.e., a narrower beamwidth as a result of more vertical array elements) is necessary. However, as shown in Fig. 3.4, there

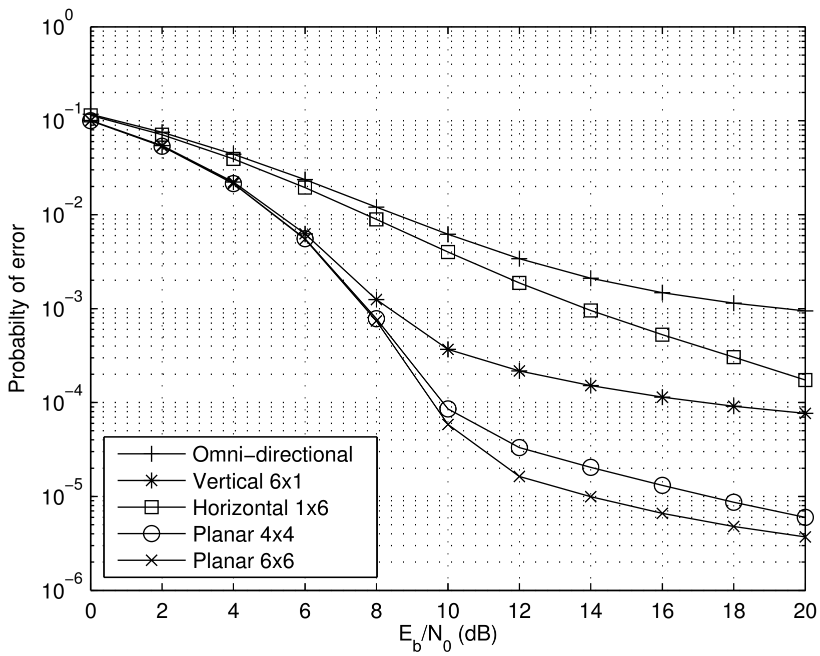

Figure 3.1: Beamsteering performance at a range of 5 m

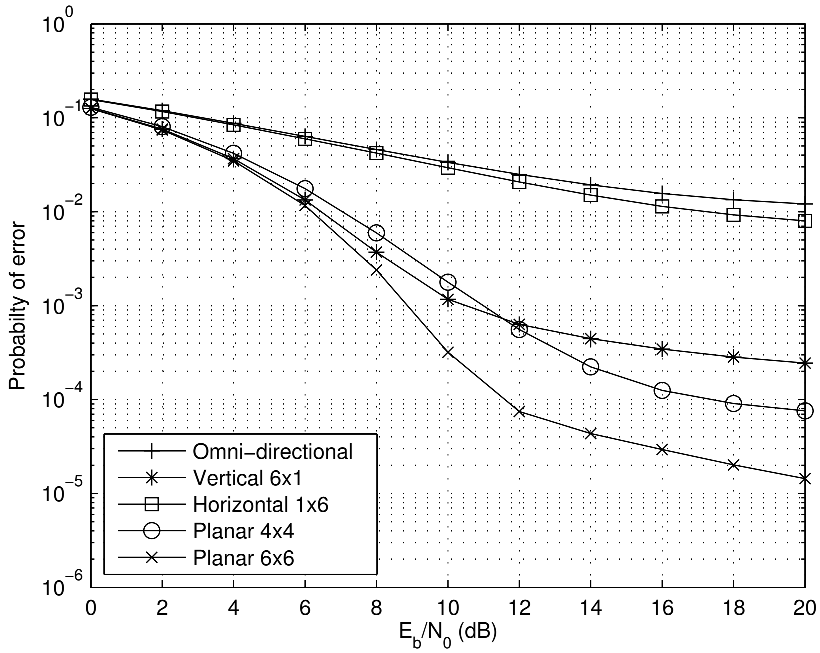

Figure 3.2: Beamsteering performance at a range of 10 m

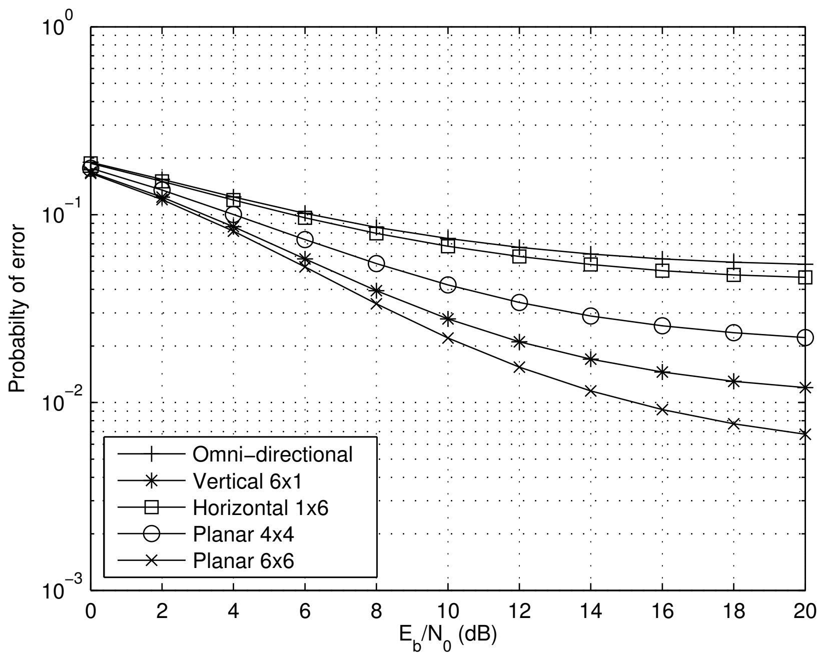

Figure 3.3: Beamsteering performance at a range of 25 m

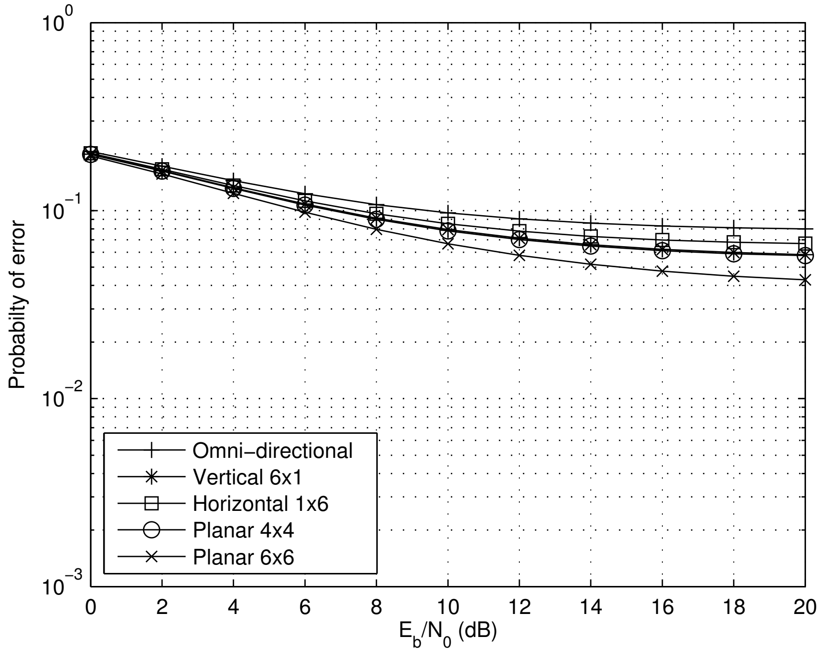

Figure 3.4: Beamsteering performance at a range of 50 m

is a minimal improvement in the performance of the six by six array over the four by four array at 50 m. Thus, at longer ranges, increasing the array size is not a promising solution.

3.3 Performance versus range

We now desire to simulate the probability of a bit error with respect to the range between the transmitter and receiver. To do this, we setup a link budget based on published capabilities of hardware at 60 GHz. Power amplifiers presented in [27] and [28] achieve output powers of 13.1 dBm and 14.5 dBm, respectively, with 1-dB compression. Thus, the transmit power is set to 13 dBm. The receiver noise figure is set to 6 dB which is a conservative estimate among values recently achieved (see, e.g., [29]). The linear arrays have a gain of 7.8 dBi, the four by four planar array has a gain of 12 dBi, and the six by six planar array has a gain of 15.6 dBi. The modulation is BPSK, the bit rate is 1 Gbps, and the roll-off factor is 0.25.

Based on this link budget, for an AWGN channel and a range of 100 meters the six by six planar array achieves an E_b/N_0 of 14.0 dB and $P_e = 10^{-12}$. Thus, sufficient antenna gain is provided by 36 antenna elements for low order modulations and especially BPSK. However, as demonstrated by the results shown in Figure 3.5, ISI limits the average probability of error to be greater than 10^{-2} for ranges of 50 m and greater. The six by six planar array demonstrates the best performance across all ranges as a result of having the highest array gain and most effective mitigation of multipath.

Comparing the P_b curves of both linear arrays we note that for distances less than about 5 m, the horizontal array performs better; and for distances greater than 5 m, the vertical array performs better. This follows exactly what we saw before, where the ground bounce is initially insignificant, but grows in relative strength as the range increases. Between 2.5 and 10 m the vertical array is capable of mitigating the ground bounce and its performance only drops by a single order of magnitude, while the horizontal array's performance drops by more than 3 orders of magnitude. As the link becomes interference limited, both linear

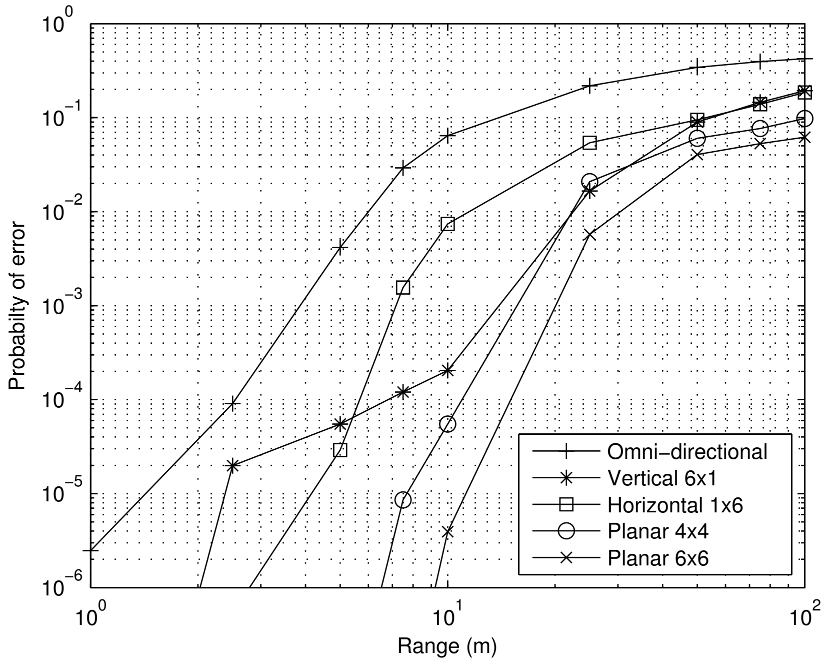

Figure 3.5: Probability of error versus distance over several array configurations

arrays converge to the same performance.

In Figs. 3.3 and 3.4 the vertical linear array achieved performance better than or equal to that of the four by four planar array. Now that array gain is considered, the four by four planar array benefits from higher SNR at the output of the array and outperforms the vertical array for ranges 50 m and greater.

We observe that the probability or error is greatly affected by a fraction of the channels having poor characteristics. As an example, whenever the transmitter and receiver are very close to a wall, this multipath component is on the same order of magnitude as the LOS path. Further insight into the performance is gained by assessing the link's probability of outage at longer ranges shown in Table 3.1. An outage is defined as any link which achieves a P_b less than a threshold of 10^{-6}.

Table 3.1: Outage probability with threshold $P_b < 10^{-6}$

	10 m	25 m	50 m	75 m	100 m
Omni-directional	1.0	1.0	1.0	1.0	1.0
Vertical	6.8×10^{-3}	0.75	1.0	1.0	1.0
Horizontal	0.38	0.74	1.0	1.0	1.0
Planar 4x4	5.3×10^{-4}	0.26	0.44	0.58	0.83
Planar 6x6	4.0×10^{-5}	9.8×10^{-2}	0.31	0.36	0.42

3.4 Conclusion

An initial analysis of the performance of antenna arrays in the 60 GHz band outdoors was presented in this chapter. The results demonstrate that beamsteering is not successful in mitigating ISI due to multipath. When the link budget is taken into account, reliable communication can only be achieved for ranges up to 10 m. At ranges of 25 and 50 m – typical ranges for outdoor environments – the link is severely interference limited.

At longer ranges, the ground bounce is a significant source of ISI. This is because as distance increases the magnitude and time delay approach that of the LOS path. In addition, the ground bounce enters the main beam of the array pattern. At ranges of 26 m and greater, the ground bounce will always have a delay relative to the LOS of less than 1 ns. At a data rate of 1 Gbps, this delay is less than the symbol period. Thus, it is expected that equalization will also be unable to resolve the ground bounce as the range is increased above 26 m.

Even though a larger number of array elements increases the directivity of the array, we observe a minimal improvement in performance with a larger array. For example, in Fig. 3.5 the six by six array does not significantly reduce P_b compared with the four by four array at ranges greater than or equal to 50 m. Thus, more powerful methods of array processing are explored in Chapter 4.

Chapter 4

Array Processing: Stationary Channel

As discussed in Chapter 1, antenna arrays are needed in the 60 GHz band in order to offset poor propagation characteristics. One of the primary goals of this thesis is to determine the performance we can expect to achieve with antenna arrays in an outdoor environment at 60 GHz. In Chapter 3, beamsteering is shown to be an insufficient means of mitigating ISI due to multipath. Therefore, in order to further evaluate the effectiveness of array processing at 60 GHz, improved methods of array processing are considered in this chapter.

In the literature, most of the work related to array processing for 60 GHz is focused on developing low-complexity methods of array weight selection or channel estimation [30], [31], [32]. Furthermore, work studying the performance of 60 GHz systems often makes a general assumption of directional antennas [19], [33]. Our goal is to determine the best performance which can be achieved using array processing. Therefore, in this chapter, we assume that the channel is stationary over the observation period and that the receiver has complete knowledge of the channel. The use of antenna arrays for the purpose of co-channel interference and multipath (or intersymbol) interference mitigation has been investigated (for example, [34] and [35]). We analyze the effectiveness of this concept in an outdoor environment in the 60 GHz band by obtaining performance results specific to our model of the Virginia Tech campus.

In Section 4.1, we present background theory of array processing. Numerous optimal array processing methods have been developed in the literature and each is built around an optimality criterion [24], [25], [36], [37], [38], [39]. In this chapter, we look at four optimality criteria and the resulting array weights. Specifically, we consider the maximum signal to interference and noise ratio (SINR), maximum signal to noise ratio (SNR), minimum mean square error (MMSE), and linearly constrained minimum variance (LCMV) criteria. Beamsteering is shown to provide identical weights to the maximum SNR criterion. In addition, the beam codebook based array processing method that has been adopted by the IEEE 802.15.3c standard [40] for 60 GHz systems is introduced in Section 4.2.

In Section 4.3, the performance of each method is simulated in the outdoor environment presented in Chapter 2. All array processing methods are used to determine the receiver's weight vector. At the transmitter we implement beamsteering. In quantifying the performance of each optimality criteria, we are able to select an effective criterion for adaptive array processing developed in Chapter 5. This chapter is concluded in Section 4.4

4.1 Array processing theory

In this chapter, as with beamsteering in Chapter 3, the strongest path (i.e., the LOS) is treated as the desired signal. The way in which the other multipaths are treated varies with each method. Before presenting each optimality criterion and the resulting array weights, two statistics of the received signal vector $\mathbf{x}$, defined in (2.32), are introduced.

The *correlation vector* $\mathbf{r}_{\mathbf{x}s_0}$ is a measure of the correlation between the received signal and the desired signal. The desired signal is the signal of the strongest path s_0 as defined in

(2.28). Using these definitions, we can express the correlation vector as

$$
\begin{aligned}
\mathbf{r}_{\mathbf{x}s_0} &= E[\mathbf{x}s_0^*] \\
&= E\left[\left(\sum_{k=0}^{K-1} \mathbf{v}_{r,k}s_k + \mathbf{n}'\right) s_0^*\right] \\
&= E\left[\sum_{k=0}^{K-1} \mathbf{v}_{r,k}s_k s_0^*\right] + E[\mathbf{n}' s_0^*] \\
&= \sum_{k=0}^{K-1} \mathbf{v}_{r,k}E[s_k s_0^*]. \qquad (4.1)
\end{aligned}
$$

where, as defined in (2.16), $\mathbf{v}_{r,k}$ is the array vector of phase offsets experienced by the kth multipath. The data symbols are assumed to have equal probabilities. We assume that we have knowledge of the channel parameters (α_k, ψ_k, η_k, ϵ_k, and $\mathbf{v}_{r,k}$) when calculating the array weights. The expectation of the signal components ($E[s_k s_0^*]$) will be explored further. First, the next statistic – the *correlation matrix* of the signal vector – is introduced. The correlation matrix is given by

$$
\begin{aligned}
\mathbf{R}_{\mathbf{xx}} &= E\left[\mathbf{x}\mathbf{x}^H\right] \\
&= E\left[\left(\sum_{k=0}^{K-1} \mathbf{v}_{r,k}s_k + \mathbf{n}'\right)\left(\sum_{k=0}^{K-1} \mathbf{v}_{r,k}s_k + \mathbf{n}'\right)^H\right] \\
&= E\left[\sum_{k_1=0}^{K-1}\sum_{k_2=0}^{K-1} \mathbf{v}_{r,k_1}\mathbf{v}_{r,k_2}^H s_{k_1}s_{k_2}^* + \sum_{k=0}^{K-1} \mathbf{v}_{r,k}\mathbf{n}'^H s_k + \sum_{k=0}^{K-1} \mathbf{n}'\mathbf{v}_{r,k}^H s_k^* + \mathbf{n}'\mathbf{n}'^H\right] \\
&= \sum_{k_1=0}^{K-1}\sum_{k_2=0}^{K-1} \mathbf{v}_{r,k_1}\mathbf{v}_{r,k_2}^H E\left[s_{k_1}s_{k_2}^*\right] + \sum_{k=0}^{K-1} \mathbf{v}_{r,k}E\left[\mathbf{n}'^H s_k\right] + \sum_{k=0}^{K-1} E\left[\mathbf{n}' s_k^*\right]\mathbf{v}_{r,k}^H + E\left[\mathbf{n}'\mathbf{n}'^H\right] \\
&= \sum_{k_1=0}^{K-1}\sum_{k_2=0}^{K-1} \mathbf{v}_{r,k_1}\mathbf{v}_{r,k_2}^H E\left[s_{k_1}s_{k_2}^*\right] + N_0\mathbf{I}. \qquad (4.2)
\end{aligned}
$$

As with (4.1), the expression for $\mathbf{R}_{\mathbf{xx}}$ is a function of $E[s_{k_1}s_{k_2}^*]$ which can be expanded as follows

$$\begin{aligned}
E[s_{k_1} s_{k_2}^*] = E\Bigg[&\left(\alpha_{k_1} e^{j\psi_{k_1}} \sum_{m_1=-\infty}^{\infty} y_{m_1} g\left((l - m_1 - \eta_{k_1} - \epsilon_{k_1})T\right) \right) \\
&\cdot \left(\alpha_{k_2} e^{-j\psi_{k_2}} \sum_{m_2=-\infty}^{\infty} y_{m_2}^* g\left((l - m_2 - \eta_{k_2} - \epsilon_{k_2})T\right) \right) \Bigg] \\
= \alpha_{k_1} \alpha_{k_2} e^{j\psi_{k_1}} e^{-j\psi_{k_2}} &\sum_{m_1=-\infty}^{\infty} \sum_{m_2=-\infty}^{\infty} \Big(E[y_{m_1} y_{m_2}^*] g\left((l - m_1 - \eta_{k_1} - \epsilon_{k_1})T\right) \\
&\cdot g\left((l - m_2 - \eta_{k_2} - \epsilon_{k_2})T\right) \Big) \\
= \alpha_{k_1} \alpha_{k_2} e^{j(\psi_{k_1} - \psi_{k_2})} &\sum_{m=-\infty}^{\infty} \Big(g\left((l - m - \eta_{k_1} - \epsilon_{k_1})T\right) \\
&\cdot g\left((l - m - \eta_{k_2} - \epsilon_{k_2})T\right) \Big).
\end{aligned} \tag{4.3}$$

where the definition of s_k from (2.28) is substituted. The expression in (4.3) follows from the assumption that

$$E[y_{m_1} y_{m_2}^*] = \begin{cases} 0 & m_1 \neq m_2 \\ 1 & m_1 = m_2 \end{cases}. \tag{4.4}$$

It is assumed that the receiver is synchronized with the strongest path s_0 and that the delay and phase of the multipaths are normalized by the strongest path. This results in $\eta_0 = 0$, $\epsilon_0 = 0$, and $\psi_0 = 0$. Substituting (4.3) into (4.1) and setting $\eta_0 = \epsilon_0 = \psi_0 = 0$, the expression for the correlation vector can be simplified as

$$\begin{aligned}
\mathbf{r}_{\mathbf{x}s_0} &= \sum_{k=0}^{K-1} \mathbf{v}_{r,k} E[s_k s_0^*] \\
&= \sum_{k=0}^{K-1} \mathbf{v}_{r,k} \alpha_k \alpha_0 e^{j\psi_k} e^{-j\psi_0} \sum_{m=-\infty}^{\infty} g\left((l - m - \eta_k - \epsilon_k)T\right) g\left((l - m - \eta_0 - \epsilon_0)T\right) \\
&= \sum_{k=0}^{K-1} \mathbf{v}_{r,k} \alpha_k \alpha_0 e^{j\psi_k} \sum_{m=-\infty}^{\infty} g\left((l - m - \eta_k - \epsilon_k)T\right) g\left((l - m)T\right).
\end{aligned} \tag{4.5}$$

Since the raised cosine pulse shape has nulls at $t = \pm T, \pm 2T \ldots$, it follows that

$$g((l-m)T) = \begin{cases} 0 & m \neq l \\ 1 & m = l \end{cases}. \tag{4.6}$$

Therefore, the correlation vector given by (4.5) reduces to

$$\mathbf{r}_{\mathbf{x}s_0} = \sum_{k=0}^{K-1} \mathbf{v}_{r,k} \alpha_k \alpha_0 e^{j\psi_k} g\left((-\eta_k - \epsilon_k)T\right). \tag{4.7}$$

For ease of analysis, we assume that the pulse $g(t)$ used for transmission is truncated such that it is non-zero over the interval

$$-\frac{N_{\text{sym}}}{2} T \leq t \leq \frac{N_{\text{sym}}}{2} T, \tag{4.8}$$

where N_{sym} is the duration of the pulse in multiples of the symbol period T. Substituting $(-\eta_k - \epsilon_k)T$ for t and given that η_k is by definition an integer produces

$$-\frac{N_{\text{sym}}}{2} \leq \eta_k \leq \frac{N_{\text{sym}}}{2} - 1. \tag{4.9}$$

For any delay η_k outside of this range, $g\left((-\eta_k - \epsilon_k)T\right) = 0$ in (4.7).

Returning to the correlation matrix $\mathbf{R}_{\mathbf{xx}}$ given in (4.2), we substitute (4.3) for $E[s_{k_1} s_{k_2}^*]$. Due to the finite pulse duration given in (4.8), the range of symbol indexes in the summation (4.3) can be reduced. We define a set $\mathcal{Y}_{k_1,k_2}$ as the symbol indexes m for which the term $g\left((l - m - \eta_{k_1} - \epsilon_{k_1})T\right) g\left((l - m - \eta_{k_2} - \epsilon_{k_2})T\right)$ is non-zero. Without loss of generality we let $l = 0$. The resulting expression for $\mathbf{R}_{\mathbf{xx}}$ is given by

$$\begin{aligned}\mathbf{R}_{\mathbf{xx}} = \sum_{k_1=0}^{K-1} \sum_{k_2=0}^{K-1} \Bigg(& \mathbf{v}_{r,k_1} \mathbf{v}_{r,k_2}^H \alpha_{k_1} \alpha_{k_2} e^{j(\psi_{k_1} - \psi_{k_2})} \\ & \cdot \sum_{m \in \mathcal{Y}_{k_1,k_2}} g\left((-m - \eta_{k_1} - \epsilon_{k_1})T\right) g\left((-m - \eta_{k_2} - \epsilon_{k_2})T\right) \Bigg) + N_0 \mathbf{I}.\end{aligned} \tag{4.10}$$

All the above work is used to calculate the signal statistics in simulations of array processor performance.

In the derivations that follow, the subscript r will be removed since we a concerned only with the receiver's array. Thus, for simplicity, we use $\mathbf{v}_k$ to denote $\mathbf{v}_{r,k}$, $\mathbf{v}_0$ to denote $\mathbf{v}_{r,0}$, and $\mathbf{w}$ to denote $\mathbf{w}_r$.

4.1.1 Maximum signal to interference and noise ratio

In this method, the performance metric is signal to interference plus noise ratio. We define the signal to be the strongest received multipath component. The other multipath components are treated as interference. To simplify the notation, the received signal $\mathbf{x}$ is expressed as

$$\mathbf{x} = \mathbf{v}_0 s_0 + \mathbf{u}, \tag{4.11}$$

where

$$\mathbf{u} = \sum_{k=1}^{K-1} \mathbf{v}_k s_k + \mathbf{n}'. \tag{4.12}$$

Following the same process used to obtain (4.10), the correlation matrix of the interference is given by

$$\begin{aligned}\mathbf{R_{uu}} &= E[\mathbf{u}\mathbf{u}^H] \\ &= \sum_{k_1=1}^{K-1} \sum_{k_2=1}^{K-1} \Bigg(\mathbf{v}_{k_1} \mathbf{v}_{k_2}^H \alpha_{k_1} \alpha_{k_2} e^{j(\psi_{k_1} - \psi_{k_2})} \\ &\qquad \cdot \sum_{m \in \mathcal{Y}_{k_1,k_2}} g\left((-m - \eta_{k_1} - \epsilon_{k_1})T\right) g\left((-m - \eta_{k_2} - \epsilon_{k_2})T\right) \Bigg) + N_0 \mathbf{I}. \end{aligned} \tag{4.13}$$

A derivation for the weights which maximize SINR is given in [37]. We present the derivation here for completeness while adapting the notation to the one used in our work. The SINR is given by

$$\begin{aligned}\mathrm{SINR} &= \frac{E\left[|\mathbf{w}^H \mathbf{v}_0 s_0|^2\right]}{E\left[|\mathbf{w}^H \mathbf{u}|^2\right]} \\ &= \frac{E\left[\mathbf{w}^H \mathbf{v}_0 s_0 s_0^* \mathbf{v}_0^H \mathbf{w}\right]}{E\left[\mathbf{w}^H \mathbf{u}\mathbf{u}^H \mathbf{w}\right]} \\ &= \frac{\mathbf{w}^H \mathbf{v}_0 E[s_0 s_0^*] \mathbf{v}_0^H \mathbf{w}}{\mathbf{w}^H E\left[\mathbf{u}\mathbf{u}^H\right] \mathbf{w}} \\ &= \alpha_0^2 \frac{\mathbf{w}^H \mathbf{v}_0 \mathbf{v}_0^H \mathbf{w}}{\mathbf{w}^H \mathbf{R_{uu}} \mathbf{w}} &(4.14) \\ &= \alpha_0^2 \frac{\mathbf{z}^H \mathbf{R_{uu}}^{-1/2} \mathbf{v}_0 \mathbf{v}_0^H \mathbf{R_{uu}}^{-1/2} \mathbf{z}}{\mathbf{z}^H \mathbf{z}} &(4.15)\end{aligned}$$

where in (4.15) we make the substitution $\mathbf{z} = \mathbf{R}_{\mathbf{uu}}^{1/2}\mathbf{w}$ to produce a standard quadratic form. The expression in (4.15) is known to be bounded by the maximum and minimum eigenvalues of $\mathbf{R}_{\mathbf{uu}}^{-1/2}\mathbf{v}_0\mathbf{v}_0^H\mathbf{R}_{\mathbf{uu}}^{-1/2}$ which is equivalent to $\mathbf{R}_{\mathbf{uu}}^{-1}\mathbf{v}_0\mathbf{v}_0^H$. It is explained in [37] that the optimization of the SINR can be setup as a eigenvalue problem. The maximum eigenvalue is denoted $\mathrm{SINR}_{\mathrm{opt}}$ and the corresponding eigenvector is denoted $\mathbf{w}_{\mathrm{opt}}$. The generalized eigenvalue problem is given by

$$\mathbf{v}_0\mathbf{v}_0^H\mathbf{w}_{\mathrm{opt}} = \mathrm{SINR}_{\mathrm{opt}}\mathbf{R}_{\mathbf{uu}}\mathbf{w}_{\mathrm{opt}}. \tag{4.16}$$

We substitute (4.14) with optimal weight vector $\mathbf{w}_{\mathrm{opt}}$ to produce

$$\mathbf{v}_0\mathbf{v}_0^H\mathbf{w}_{\mathrm{opt}} = \alpha_0^2\frac{\mathbf{w}_{\mathrm{opt}}^H\mathbf{v}_0\mathbf{v}_0^H\mathbf{w}_{\mathrm{opt}}}{\mathbf{w}_{\mathrm{opt}}^H\mathbf{R}_{\mathbf{uu}}\mathbf{w}_{\mathrm{opt}}}\mathbf{R}_{\mathbf{uu}}\mathbf{w}_{\mathrm{opt}}. \tag{4.17}$$

The term $\mathbf{v}_0^H\mathbf{w}_{\mathrm{opt}}$ is a scalar which appears on both sides of the equation. Thus, we remove this term which yields

$$\mathbf{v}_0 = \alpha_0^2\frac{\mathbf{w}_{\mathrm{opt}}^H\mathbf{v}_0}{\mathbf{w}_{\mathrm{opt}}^H\mathbf{R}_{\mathbf{uu}}\mathbf{w}_{\mathrm{opt}}}\mathbf{R}_{\mathbf{uu}}\mathbf{w}_{\mathrm{opt}}. \tag{4.18}$$

The term $\alpha_0^2\frac{\mathbf{w}_{\mathrm{opt}}^H\mathbf{v}_0}{\mathbf{w}_{\mathrm{opt}}^H\mathbf{R}_{\mathbf{uu}}\mathbf{w}_{\mathrm{opt}}}$ is scalar which we will denote by b. We rearrange (4.18) to solve for the optimal weights. The result is

$$\mathbf{w}_{\mathrm{SINR}} = \left(\frac{1}{b}\right)\mathbf{R}_{\mathbf{uu}}^{-1}\mathbf{v}_0. \tag{4.19}$$

The value of b simply scales the weight vector and does not affect the SINR.

4.1.2 Maximum signal to noise ratio

The derivation for the maximum SNR method follows the same procedure as the maximum SINR method. The result in (4.19) is used directly. The difference is that when no interference signal exists, the correlation matrix $\mathbf{R}_{\mathbf{uu}}$ simplifies to

$$\mathbf{R}_{\mathbf{uu}} = N_0\mathbf{I}. \tag{4.20}$$

Thus, the optimal weights are

$$\mathbf{w}_{\mathrm{opt}} = \left(\frac{1}{b}\right)\frac{1}{N_0}\mathbf{v}_0, \tag{4.21}$$

which in terms of SNR is equivalent to

$$\mathbf{w}_{\mathrm{SNR}} = \mathbf{v}_0. \tag{4.22}$$

This result is equivalent to the weights given by beamsteering. Thus, we conclude that beamsteering is optimal in the sense that it maximizes SNR.

4.1.3 Minimum mean square error

In this method, error is defined as the difference between the desired signal and the array output written as

$$e = \mathbf{w}^H \mathbf{x} - s_0. \tag{4.23}$$

The objective function which we seek to minimize is the mean square error (MSE) given by [39]

$$\begin{aligned} J(\mathbf{w}) &= E\left[|e|^2\right] \\ &= E\left[|\mathbf{w}^H \mathbf{x} - s_0|^2\right] \\ &= \mathbf{w}^H E\left[\mathbf{x}\mathbf{x}^H\right]\mathbf{w} - \mathbf{w}^H E\left[\mathbf{x}s_0^*\right] - E\left[s_0\mathbf{x}^H\right]\mathbf{w} + E\left[s_0 s_0^*\right] \\ &= \mathbf{w}^H \mathbf{R}_{\mathbf{xx}}\mathbf{w} - \mathbf{w}^H \mathbf{r}_{\mathbf{x}s_0} - \mathbf{r}_{\mathbf{x}s_0}^H \mathbf{w} + E\left[s_0 s_0^*\right]. \end{aligned} \tag{4.24}$$

The minimum is found by setting $\nabla J(\mathbf{w}) = \mathbf{0}$ and solving for $\mathbf{w}$. However, the derivative $\frac{\partial w^*}{\partial w}$ is not defined because w^* is not an analytic function of w. In [41], a proof is given to demonstrate that the objective function can be minimized when the gradient is taken with respect to either w^* or w where the variable w and its conjugate are considered unique. Thus, $\frac{\partial w^*}{\partial w} = 0$ and $\frac{\partial w}{\partial w^*} = 0$. Applying these concepts, [41] provides three gradient identities with respect to the variable w^*. First, the gradient is defined as

$$\nabla = \begin{bmatrix} \frac{\partial}{\partial w_1^*} \\ \frac{\partial}{\partial w_2^*} \\ \vdots \\ \frac{\partial}{\partial w_{N_r}^*} \end{bmatrix}. \tag{4.25}$$

The identities given by [41] are

$$\nabla(\mathbf{a}^H\mathbf{w}) = \mathbf{0}, \tag{4.26}$$

$$\nabla(\mathbf{w}^H\mathbf{a}) = \mathbf{a}, \text{ and} \tag{4.27}$$

$$\nabla(\mathbf{w}^H\mathbf{A}\mathbf{w}) = \mathbf{A}\mathbf{w}. \tag{4.28}$$

Applying these identities, the gradient of the MSE is

$$\nabla J(\mathbf{w}^H) = \mathbf{R}_{\mathbf{xx}}\mathbf{w} - \mathbf{r}_{\mathbf{x}s_0}. \tag{4.29}$$

Setting the right hand side of (4.29) equal to zero, the weights which minimize the objective function are

$$\mathbf{w}_{\mathrm{MMSE}} = \mathbf{R}_{\mathbf{xx}}^{-1}\mathbf{r}_{\mathbf{x}s_0}. \tag{4.30}$$

4.1.4 Linearly constrained minimum variance

In this method, we constrain the array response in the direction of the LOS path to be 1 as expressed by $\mathbf{w}^H\mathbf{v}_0 = 1$. The variance of the array output is minimized subject to (s.t.) this constraint. The variance of the array output is given by

$$E\left[|\hat{y}|^2\right] = E\left[\mathbf{w}^H\mathbf{x}\mathbf{x}^H\mathbf{w}\right] = \mathbf{w}^H\mathbf{R}_{\mathbf{xx}}\mathbf{w}. \tag{4.31}$$

The optimization problem can be stated formally as follows:

$$\min \quad \mathbf{w}^H\mathbf{R}_{\mathbf{xx}}\mathbf{w} \tag{4.32}$$

$$\text{s.t.} \quad \mathbf{w}^H\mathbf{v}_0 = 1. \tag{4.33}$$

The method of Lagrange multipliers [42] is used to find the minimum variance. Stationary points are found in this method. Due to the quadratic form of (4.32), a single stationary point exists which corresponds to the minimum for this function. A new function is defined

$$\Lambda(\mathbf{w}, \lambda) = \mathbf{w}^H\mathbf{R}_{\mathbf{xx}}\mathbf{w} + \lambda(\mathbf{w}^H\mathbf{v}_0 - 1), \tag{4.34}$$

where the variable λ is the Lagrange multiplier. The minimum is found by solving the following system of equations:

$$\nabla\Lambda(\mathbf{w},\lambda) = \mathbf{R}_{\mathbf{xx}}\mathbf{w} + \lambda\mathbf{v}_0 = 0 \tag{4.35}$$

$$\mathbf{w}^H\mathbf{v}_0 = 1, \tag{4.36}$$

where ∇ is the gradient operator for the complex conjugate weight vector as defined in (4.25). Solving (4.35) for $\mathbf{w}$ results in

$$\mathbf{w} = -\lambda\mathbf{R}_{\mathbf{xx}}^{-1}\mathbf{v}_0. \tag{4.37}$$

The value of λ is found by substitution of this result into (4.36). Manipulating the resulting equation produces

$$\begin{aligned}
&\left(\mathbf{w}^H\mathbf{v}_0 = 1\right)^* \\
&\mathbf{v}_0^H\mathbf{w} = 1 \\
&\mathbf{v}_0^H(-\lambda\mathbf{R}_{\mathbf{xx}}^{-1}\mathbf{v}_0) = 1 \\
&\lambda = -\left(\mathbf{v}_0^H\mathbf{R}_{\mathbf{xx}}^{-1}\mathbf{v}_0\right)^{-1}.
\end{aligned} \tag{4.38}$$

From equations (4.37) and (4.38) the array weight vector for the LCMV method is

$$\mathbf{w}_{\mathrm{LCMV}} = \frac{\mathbf{R}_{\mathbf{xx}}^{-1}\mathbf{v}_0}{\mathbf{v}_0^H\mathbf{R}_{\mathbf{xx}}^{-1}\mathbf{v}_0}. \tag{4.39}$$

4.2 Beam codebook concept

The design of a beam codebook intended for systems operating in the 60 GHz band is described in [30]. The goal of the beam codebook is to provide a low-complexity, low-overhead method of beamforming. The codebook is constructed from a discrete set of phase shifts (0, 90, 180, and 270 degrees) with no amplitude adjustment. This simplifies the involved hardware and reduces power consumption [30].

A medium access control (MAC) layer method for acquiring the best codebook weights is described in [40]. The proposed process divides the task of searching for the best weights into three stages: device to device linking, sector-level searching, and beam-level searching.

In the device to device linking stage, the transmitter's array and receiver's array are given quasi-omni radiation patterns in order to maximize coverage. Once the initial connection has been established, the devices search the coverage area of the selected quasi-omni pattern using a reduced beamwidth pattern known as a sector pattern. When the best sector pattern has been determined, the devices search the coverage area of the selected sector pattern with a further reduced coverage area known as the beam pattern. In each stage, the pattern which maximizes SINR is selected. The search is coordinated between the transmitter and receiver so that all combinations of transmitter and receiver patterns are checked. For example, if four sector patterns make up the selected quasi-omni patterns of the transmitter and receiver, then 16 combinations of sector patterns will be searched. By breaking the search into stages, the proposed method reduces the overhead associated with beamforming when compared with an exhaustive beam-level search.

The codebooks presented in [30] are designed for linear arrays. For a four element linear array the codebook is given by [30]

$$\mathbf{W} = \begin{bmatrix} 1 & 1 & 1 & 1 & 1 & 1 & 1 & 1 \\ -1 & -j & -j & -j & 1 & j & j & j \\ 1 & j & -1 & -j & 1 & j & -1 & -j \\ -1 & 1 & j & -1 & 1 & -1 & -j & 1 \end{bmatrix}, \tag{4.40}$$

where each column corresponds to a pattern and each row corresponds to an array element. A figure of the beam patterns of the eight sets of weights is given in [30].

The codebooks can be applied to planar arrays using the concept of pattern multiplication [24]. Consider a four by four planar array in the x-z plane as shown in Fig. 4.1 adapted from [24]. The array elements enclosed in the ellipse form a vertical linear array. These vertical linear arrays can be treated as elements of a horizontal linear array. Thus, the planar array is a four element linear array along the x-axis where each element is a linear array in the

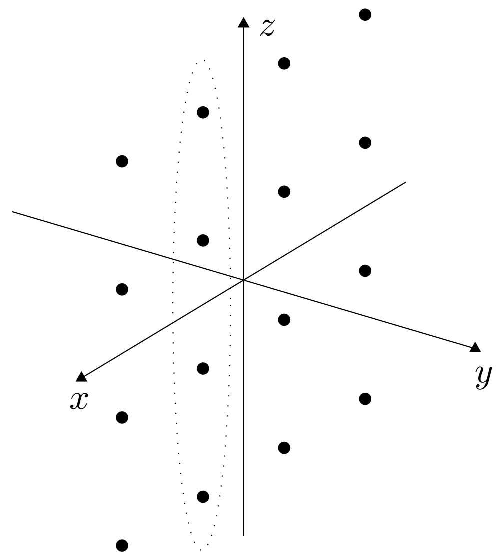

Figure 4.1: Planar array in the x–z plane

z-direction. The response of the planar array in the direction (ϕ, θ) is often termed the array factor and is denoted $AF_{\text{planar}}(\phi, \theta)$ and is calculated according to pattern multiplication as given by [24]

$$AF_{\text{planar}}(\phi, \theta) = AF_{\text{hori}}(\phi, \theta) AF_{\text{vert}}(\phi, \theta) \tag{4.41}$$

where $AF_{\text{hori}}(\phi, \theta)$ is the response of a horizontal linear array along the x-axis and $AF_{\text{vert}}(\phi, \theta)$ is the response of a vertical linear array along the z-axis.

The weights for the four by four planar array are given by

$$\mathbf{w}_m \mathbf{w}_n^T, \tag{4.42}$$

where $\mathbf{w}_i$ represents the ith column of the codebook $\mathbf{W}$. The beam pattern along the x-axis is determined by $\mathbf{w}_n$ and the beam pattern along the z-axis is determined by $\mathbf{w}_m$.

The array gain of the codebook is compared to the array gain of beamsteering in [30] and its performance in terms of bit error rate is evaluated for an indoor environment in [40]. We compare the performance of the codebook alongside the optimal array processors in the next section.

4.3 Performance in the outdoor environment

Communication links are generally evaluated based on the probability of a bit error. Thus, the array weights which minimize P_b are said to be optimal. An array processing method which has the minimum bit error rate as its optimality criterion was developed in [43]. The main drawback of the method given by [43] is that a closed form solution to the array weights is not available. Instead, the optimal array weights can only be approximated asymptotically through the use of an iterative method. For this reason we have considered several other criteria in developing the array processing methods used in this Chapter: maximum SINR, maximum SNR, MMSE, and LCMV. These methods are not necessarily optimal in terms of the bit error probability. MMSE, in particular, would minimize the bit error probability if the interference were Gaussian distributed rather than from ISI due to multipath. In the results which follow, the probability of a bit error is chosen as the metric for comparing the performance of the array processing methods.

4.3.1 Performance versus signal to noise ratio

The performance of beamsteering (equivalently maximum SNR), maximum SINR, MMSE, and LCMV are simulated. We simulate a QPSK transmission with six by six planar arrays based on the system model described in Section 2.3. At the transmitter, beamsteering is used to direct the main beam of the array toward the LOS path. The probability of a bit error is simulated versus SNR per antenna where the signal power is taken to be the sum of the power of each multipath component as given by $\sum_{i=0}^{K-1} \alpha_k^2$.

The performance with omni-directional antennas is simulated to provide a reference point for the following results. The performance for the omni-directional system is shown in Fig. 4.2. As discussed in Chapter 3, the performance is limited by ISI due to multipath. For ranges above 10 m, increasing SNR makes very little impact on P_b.

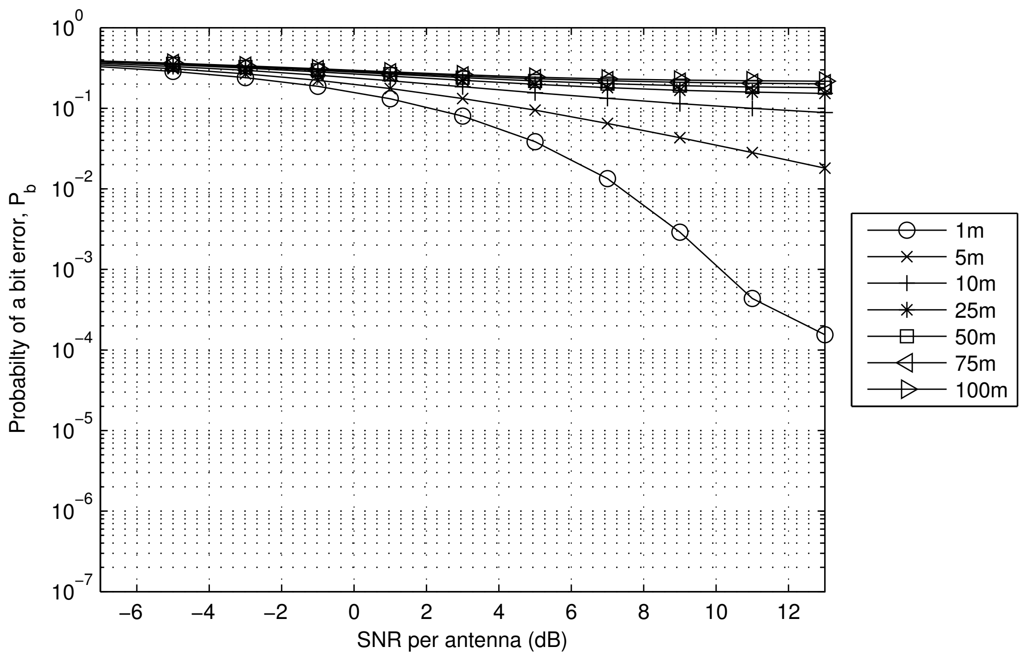

Figure 4.2: Performance for a system with omni-directional antennas

Figs. 4.3–4.6 display the performance of beamsteering, maximum SINR, MMSE, and LCMV, respectively. As seen in Fig. 4.3, and as discussed in Chapter 3, beamsteering becomes severely limited by ISI as the range increases. Maximum SINR, MMSE, and LCMV each take into account the interference due to multipath. The difference in their performance comes from how each optimality criteria handles the received multipath signal.

The maximum SINR method treats all paths other than the LOS path as interference and seeks to mitigate these paths while reducing noise power. Comparing Figs. 4.3 and 4.4, we see that the maximum SINR method leads to a performance improvement over beamsteering. Although non-LOS paths are treated as interference, they are not always sources of ISI. For example, there is often strong correlation between the ground bounce and the LOS path, especially ranges above 25 m. In these cases, the maximum SINR method rejects power

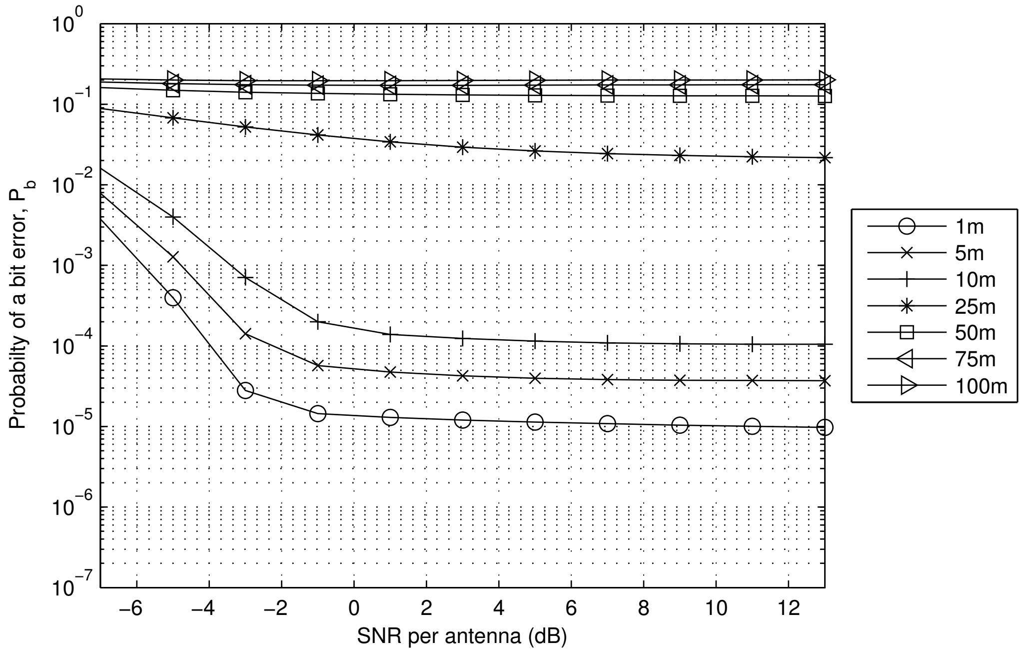

Figure 4.3: Performance of beamsteering with a six by six planar array

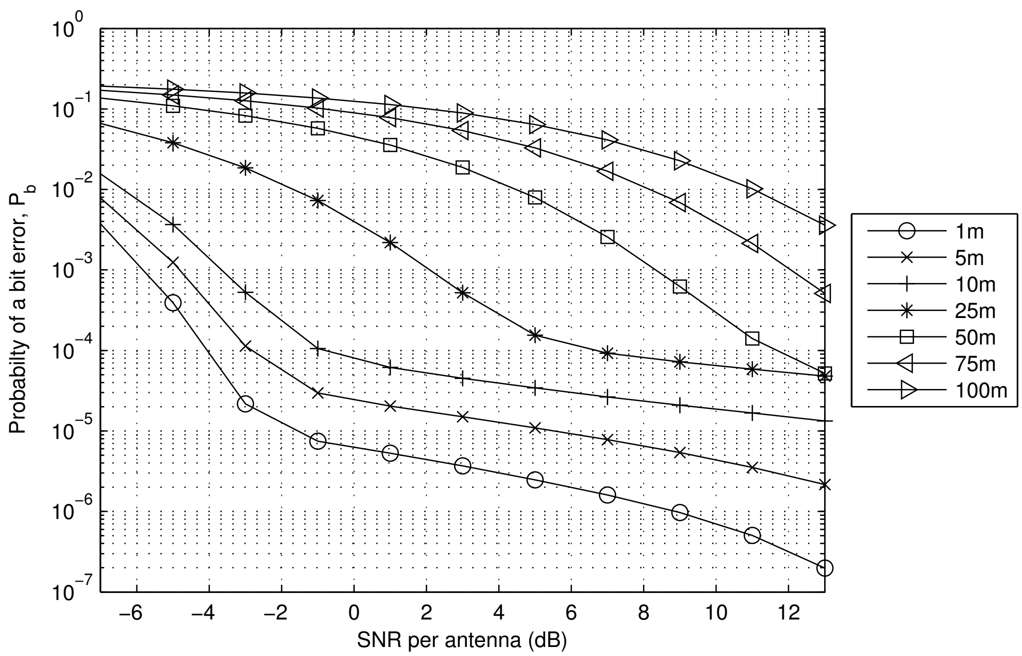

Figure 4.4: Performance of maximum SINR array processing with a six by six planar array

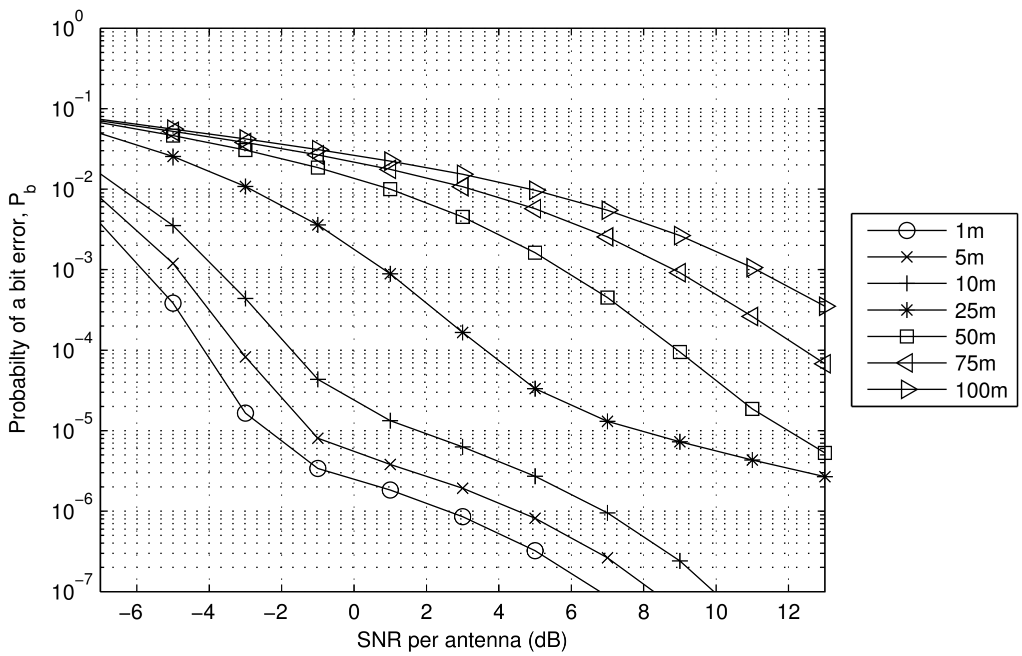

Figure 4.5: Performance of MMSE array processing with a six by six planar array

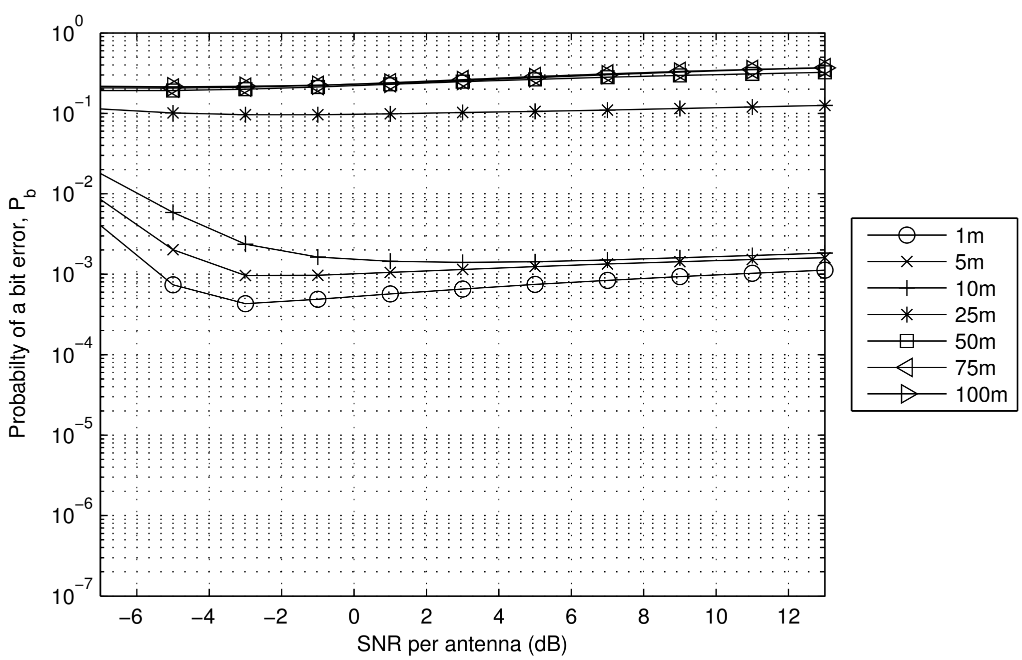

Figure 4.6: Performance of LCMV array processing with a six by six planar array

from paths which would constructively sum with the LOS path. As SNR increases, the emphasis shifts from minimizing noise power to minimizing interference. For this reason, we observe several specific cases where the probability of error curve increases with SNR when a non-LOS path is strongly correlated with the LOS path.

The MMSE array processor uses information about the desired signal's correlation with each multipath component constructively by means of the correlation vector $\mathbf{r}_{\mathbf{x}s_0}$. Power from the correlated paths is summed constructively, effectively increasing the SNR of the output. Multipath components which are not correlated with the desired signal (i.e., orthogonal) are attenuated by the array. Comparing Figs. 4.4 and 4.5, it can be seen that taking advantage of correlated paths other than the LOS provides further performance improvements.

The most striking feature of the performance curves for the LCMV array processor shown in Fig. 4.6 is that they are not monotonically non-increasing. The LCMV method seeks to minimize the variance of the array output with the constraint that the gain of the array in the direction of the LOS path is fixed to be 1. However, when a multipath component from another direction is correlated with the LOS path, the LCMV array processor adds these signals destructively. Thus, the gain in the direction of the LOS remains as 1, but the signal from the LOS path is canceled in order to minimize variance. As SNR increases, the weight of the term $\frac{N_0}{2}\mathbf{I}$ in $\mathbf{R}_{\mathbf{xx}}$ is reduced. This means that output variance due to the multipath signal will be more significant in relationship to the noise power and the variance is more effectively minimized by canceling the desired signal. In channels with a strong ground bounce component, the signal component of the array output has, in some cases, crossed the decision threshold. These cases dominate the P_b where decreased noise power leads to worse performance. Because of the poor performance of the LCMV array processor, we do not consider it in the remaining analysis.

The MMSE array processor provides the best performance among the methods considered. Fig. 4.5 shows that the P_b curves for MMSE are not limited by ISI due to multipath. The performance of the link can be improved by increasing the transmission power. At 100 m

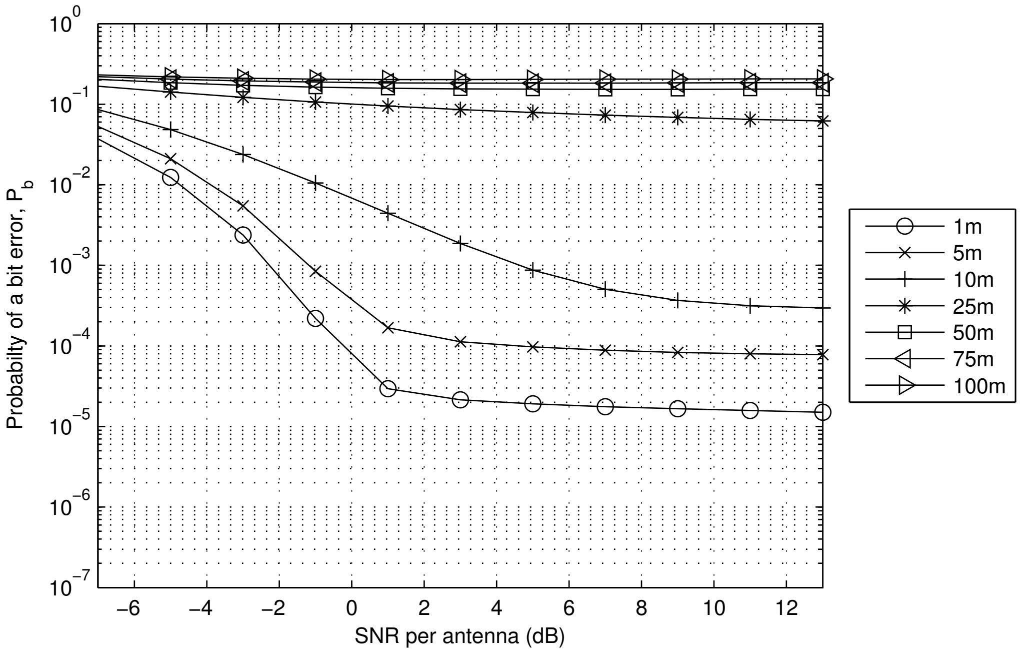

Figure 4.7: Performance of beamsteering with a four by four planar array

and for the link budget setup in Section 3.3, the average received SNR per antenna is 5.0 dB. This corresponds to an average P_b of 10^{-2}.

Figs. 4.7 and 4.8 show the performance of beamsteering and the beam codebook, respectively, for a four by four planar array. The beam codebook has nearly identical performance to that of beamsteering which is expected since the beam codebook has discrete beampatterns while beamsteering allows for continuous direction adjustment. We expect that the same behavior would be true of the six by six planar array. If so, the beam codebook would experience very similar degradations due to ISI as those observed in Fig. 4.3. Finally, limiting the phase adjustment to the discrete set of phase offsets does not noticeably reduce the performance, which agrees with the conclusions of [30].

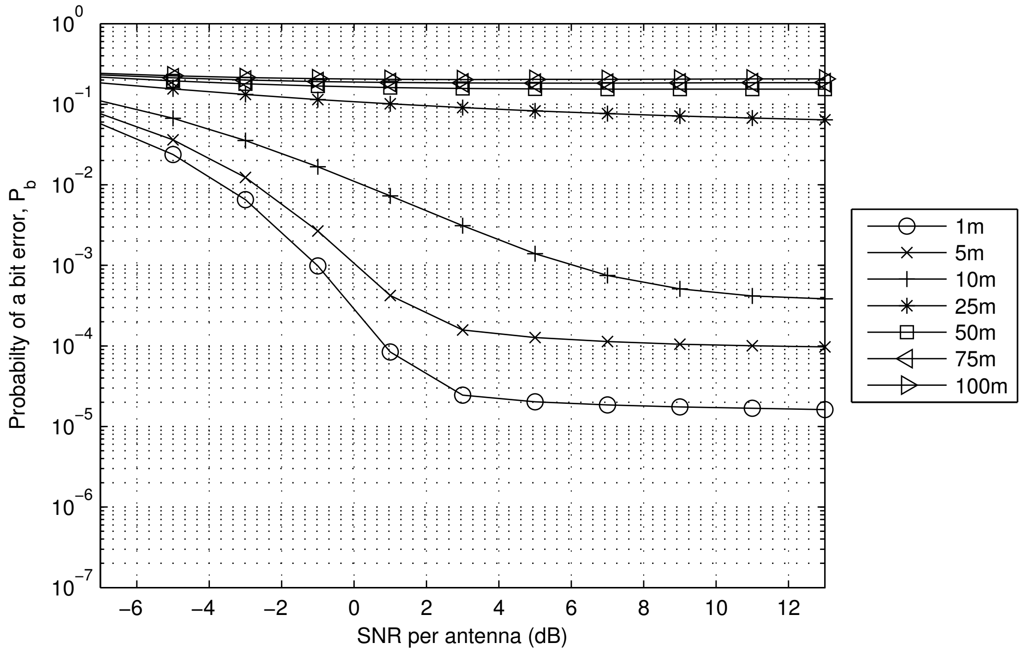

Figure 4.8: Performance of the beam codebook method with a four by four planar array

4.3.2 Analysis of the probability of error distribution

Further insight into the performance of each method can be gained by comparing the distribution of P_b. Fig. 4.9 displays the CDF of P_b for a six by six planar array. There is a cross over of the P_b curves for beamsteering and maximum SINR. Maximum SINR array processing provides gains over beamsteering in channel realizations with strong ISI. However, when non-LOS multipath components are beneficial, beamsteering is capable of achieving P_b significantly lower than maximum SINR.

The real benefit of MMSE array processing when compared to beamsteering is when the multipath interference is destructive, but correlated so that MMSE can correct the phase and add the correlated components constructively. For the MMSE method, in 25% and 50% of the channel realizations $P_b \leq 10^{-9}$ and $P_b \leq 4 \times 10^{-5}$, respectively. Compare this to the average bit error probability of 5×10^{-3} from Fig. 4.5 for the same range and SNR.

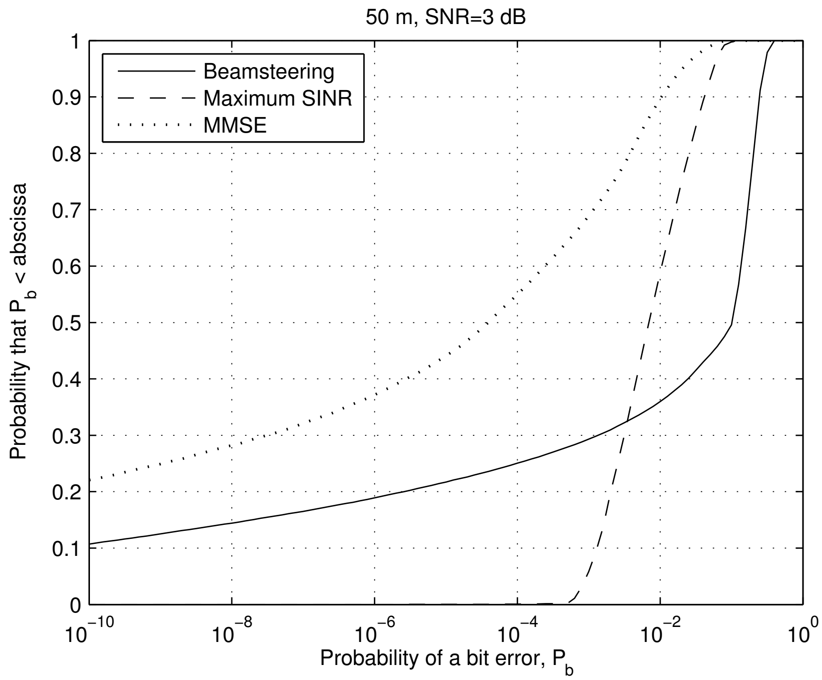

Figure 4.9: CDF of the probability of a bit error for random channels

4.3.3 Effect of the array geometry

In Chapter 2, we observed that the ground bounce path increased in strength relative the the LOS path as the range increased. In addition, the difference in delay between the ground bounce and LOS paths decreases as range increases. In general, this leads to stronger correlation between these paths, while the difference between their angles of arrival decreases. Because arrays are spatial processors, as this difference in angle of arrival decreases, the array is less effective. Taking all these factors into consideration we compare the performance of a four by four, a six by six, and a nine by four (vertical by horizontal) planar array. Fig. 4.10 shows the performance at three ranges.

With MMSE array processing, increased spatial resolution as a result of larger arrays leads to significant performance improvements. This was not the case with beamsteering as was shown in Section 3.2. We observe that at a range of 100 m the nine by four array provides a 2 dB improvement over the six by six array. The same result is observed for a 50 m range

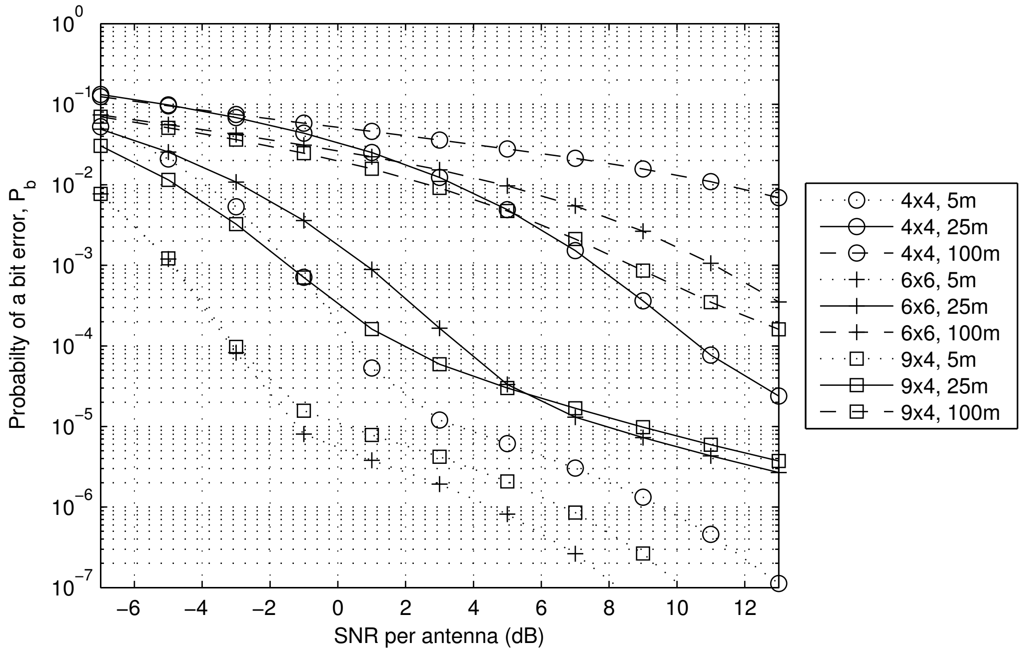

Figure 4.10: Comparison of array geometry with the MMSE method

and SNR less than 3 dB. However, the reduced resolution on the horizontal direction makes the nine by four array susceptible to strong interference from walls. For a range of 50 m and SNR greater than 5 dB the curves cross-over and the six by six array is marginally better. Since improved performance is primarily needed at longer ranges, the nine by four array is the best choice overall.

4.3.4 Performance versus transmit power

In this section, the performance versus transmit power for the six by six array is considered. The modulation is QPSK, the symbol rate is 1 GSps, and the noise figure is 6 dB. In Fig. 4.11 the performance of MMSE is shown with respect to the transmitted power. In this figure, the best 99% of the channel realization in terms of achieving the lowest P_b are selected. This removes channels with bad geometry (such as when either the transmitter or receiver are placed near to a wall) which dominate the performance as average P_b decreases. For example,

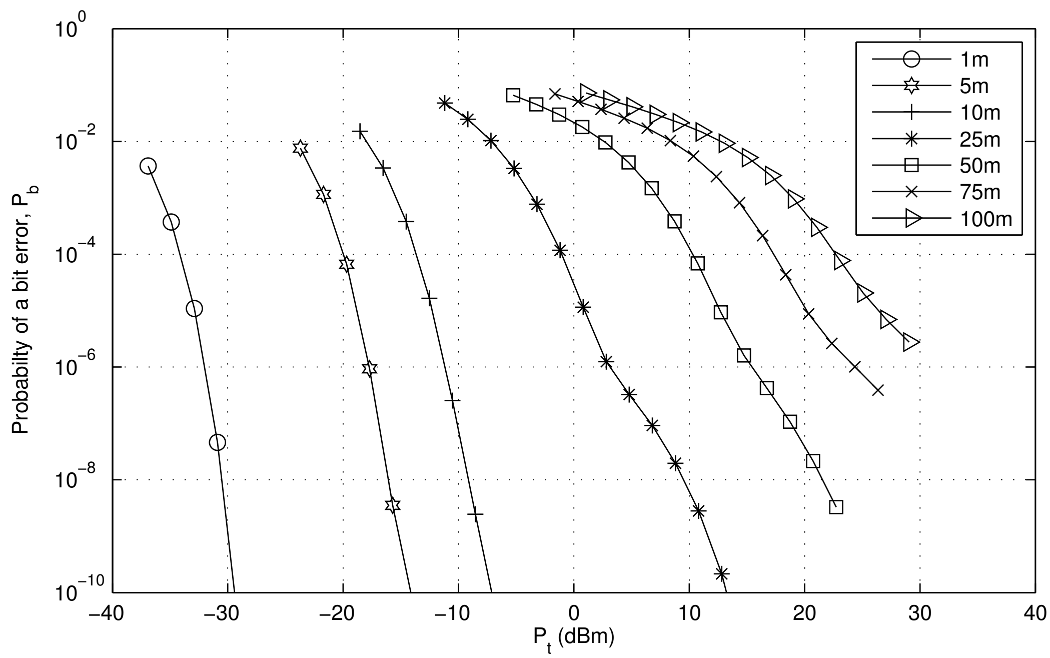

Figure 4.11: Performance versus transmitted power P_t for the best 99% of channel realizations

if 10 of the 100 000 channel realizations achieve $P_b = 10^{-1}$, the average P_b is limited to 10^{-5}.

In Fig. 4.11, as with Fig. 4.5, P_b does not become interference limited. However, due to ISI, substantial transmit power is required. Recall from Section 3.3 that in an AWGN channel with $P_t = 13$ dBm and at a range of 100 m the six by six array achieves $P_b = 10^{-12}$.

4.4 Conclusion

Four array processing methods, each built around an optimality criterion, were compared in terms of P_b in the outdoor environment developed in Chapter 2. The Maximum SINR and MMSE methods both have improved performance over beamsteering. The MMSE criterion outperforms the other methods by constructively summing correlated multipath components.

We evaluated a practical beam codebook approach to array processing which is being adopted by the IEEE 802.15.3c. The beam codebook method achieves a performance very near to that of the beamsteering method. This is expected, since the beam codebook effectively steers a beam to one of several predefined discrete directions. Thus the beam codebook, like beamsteering, does not sufficiently mitigate ISI and would need to be used along with another method for handling the frequency selective channel such as equalization or OFDM.

Based on the performance of the MMSE array processor, we find that the link budget of Section 3.3 is not sufficient to enable effective communication at a range of 100 m. With the MMSE method, the performance of the link is not interference limited which means that increased transmit power reduces P_b. Additionally, when used with MMSE array processing, larger arrays achieve significant performance improvements as demonstrated by the comparison of the four by four and six by six planar arrays in Section 4.3.3. Specifically, increased resolution in the vertical dimension improves performance at longer ranges as demonstrated by the nine by four array.

Based on this analysis, in Chapter 5, MMSE is selected as the criterion for adaptive array processing and the nine by four array is used in the outdoor environment.

Chapter 5

Array Processing: Time-Varying Channel

In communication systems, the channel – including the channel impulse response and direction of arrival information – is not known *a priori*. Adaptive algorithms based on the MMSE criterion estimate the incoming signal statistics: the correlation matrix $\mathbf{R}_{\mathbf{xx}}$ of the received signal $\mathbf{x}$ and the correlation vector $\mathbf{r}_{\mathbf{x}s_0}$ of the received signal and the desired signal s_0. Three adaptive array processing methods are considered in this chapter. The first is direct matrix inversion (DMI). In this method, estimated signal statistics are calculated from a block of samples and used in the corresponding expression for optimal weights. This requires inversion of the correlation matrix which is burdensome. The second method is the least mean square (LMS) algorithm which is a gradient method based on steepest decent. The algorithm minimizes the MSE between the actual array output and the known, desired output. Finally, the third method is the recursive least squares (RLS) algorithm. RLS estimates the inverse of the correlation matrix iteratively. In the RLS method, past samples are given less weight based on the parameter γ. RLS is known to converge faster and require more computation than LMS [36]. All three methods make use of the MMSE criterion. In order to determine the MSE, knowledge of the desired signal is required. This requirement can be met in a communication system by transmitting a training sequence.

We begin this chapter with the theoretical foundation of the three adaptive methods in Section 5.1. In section 5.2 the coherence time of the channel is considered. Walking speeds (1 m/s) are anticipated for commercial use of the 60 GHz band. Even though walking speeds would not cause rapid time variation of the channel at lower frequencies (for example, 2.4 GHz), the coherence time of the channel is inversely proportional to the carrier frequency and, therefore, time variation is important at 60 GHz.

Simulation results are divided into three sections. First, convergence is simulated in the stationary case in Section 5.3. Second, simulations of the adaptive array performance in a time varying channel are presented in Section 5.4. Third, we simulate the ability of the adaptive methods to track the changing channel by updating the weights at regular intervals in Section 5.5. The chapter conclusions are given in Section 5.6

5.1 Adaptive array theory

5.1.1 Direct matrix inversion

In this method, the signal statistics are estimated as [37]

$$\hat{\mathbf{R}}_{\mathbf{xx}} = \frac{1}{L}\sum_{l=1}^{L}\mathbf{x}(l)\mathbf{x}^{H}(l) \quad \text{and} \tag{5.1}$$

$$\hat{\mathbf{r}}_{\mathbf{x}s_0} = \frac{1}{L}\sum_{l=1}^{L}\mathbf{x}(l)s_0^{*}(l) \tag{5.2}$$

where $\mathbf{x}$ and s_0 are defined in (2.32) and (2.28), respectively, and L is the number of samples. The weights which optimize the MMSE performance are calculated from these estimates by using

$$\hat{\mathbf{w}}_{\mathrm{DMI}} = \hat{\mathbf{R}}_{\mathbf{xx}}^{-1}\hat{\mathbf{r}}_{\mathbf{x}s_0}. \tag{5.3}$$

It is possible that the estimated correlation matrix $\hat{\mathbf{R}}_{\mathbf{xx}}$ is singular for which the inverse does not exist. In this situation the pseudo-inverse is useful. Also, when the estimated correlation matrix is nearly singular, the inverse can suffer from scaling issues. Diagonal loading is another method for handling these situations in which a diagonal matrix is added to $\hat{\mathbf{R}}_{\mathbf{xx}}$ in order to improve the inversion process [44]. A disadvantage to diagonal loading is that the resulting weight vector is less sensitive [44]. In our application, diagonal loading would make the DMI method less sensitive to weaker multipath components. Singular and near singular correlation matrices are especially a problem when a small number of samples are used in the estimation process. Since it is assumed that the noise in each antenna is uncorrelated, the noise component of the correlation matrix is diagonal which aids in the inversion of $\hat{\mathbf{R}}_{\mathbf{xx}}$. Thus, as the number of samples is increased, matrix inversion becomes more reliable.

When the channel is time invariant, the performance of the DMI method approaches that of the theoretical MMSE as the number of samples used for estimation is increased. When the channel changes very slowly during the observation interval, the channel is considered to be time invariant. The definition of "changes very slowly" is related to the coherence time of the channel and is discussed in Section 5.2. Because all samples are given equal weight in (5.1) and (5.2), in a time-varying channel the DMI method will not effectively track changes in the channel. Instead the weights need to be re-estimated from new sets of samples as the channel changes. The performance of DMI is considered with respect to the number of samples L used in the estimates, while LMS and RLS are iterative methods in which performance is evaluated as a function of the number of iterations.

5.1.2 Least mean squares

The LMS algorithm, proposed for antenna arrays by Widrow [39], updates the weight vector as part of an iterative process of minimizing the MSE between the desired and actual array output. We use the same definitions for the error as we did in Section 4.1.3,

$$e(l) = \mathbf{w}^H(l)\mathbf{x}(l) - s_0(l), \tag{5.4}$$

where l is the sample index. The MSE is given by

$$E\left[|e|^2\right] = \mathbf{w}^H\mathbf{R}_{\mathbf{xx}}\mathbf{w} - \mathbf{w}^H\mathbf{r}_{\mathbf{x}s_0} - \mathbf{r}_{\mathbf{x}s_0}^H\mathbf{w} + E\left[s_0 s_0^*\right]. \tag{5.5}$$

The gradient of the MSE, as determined in Section 4.1.3, is

$$\nabla E\left[|e|^2\right] = \mathbf{R}_{\mathbf{xx}}\mathbf{w} - \mathbf{r}_{\mathbf{x}s_0}. \tag{5.6}$$

The method of steepest descent [37] provides a method for iteratively updating the weight vector. In the method of steepest decent, the weights are updated by taking successive steps in the direction opposite to the gradient of the MSE evaluated for the current weights. The direction opposite to the gradient vector is the direction of steepest downward slope in the MSE performance surface. The weight update equation is [37]

$$\mathbf{w}(l+1) = \mathbf{w}(l) - \mu(\mathbf{R}_{\mathbf{xx}}\mathbf{w}(l) - \mathbf{r}_{\mathbf{x}s_0}) \tag{5.7}$$

where μ is the step size parameter[1]. The expression in (5.7) does not require inversion of $\mathbf{R}_{\mathbf{xx}}$, but still assumes $\mathbf{R}_{\mathbf{xx}}$ and $\mathbf{r}_{\mathbf{x}s_0}$ are known. In the LMS algorithm, the signal statistics are estimated from a single sample and the weights are updated according to the method of steepest descent. Using the current sample to estimate $\hat{\mathbf{R}}_{\mathbf{xx}}$ and $\hat{\mathbf{r}}_{\mathbf{x}s_0}$ gives the approximations

$$\hat{\mathbf{R}}_{\mathbf{xx}} \approx \mathbf{x}(l)\mathbf{x}^H(l) \quad \text{and} \tag{5.8}$$

$$\hat{\mathbf{r}}_{\mathbf{x}s_0} \approx \mathbf{x}(l)s_0^*(l), \tag{5.9}$$

[1]The equations (5.7), (5.11), and (5.12) differ from the equations presented in [37] by a factor of two. This factor arises in (5.7) due to the way in which the gradient was calculated. Monzingo [37] derives the expression for the MSE gradient for real numbers and applies the result to complex numbers. In our work, we make use of [41] in deriving the MSE gradient for complex numbers. The factor of two is then introduced in (5.11) and (5.12) in order to remain consistent with Monzingo's work.

respectively. Substituting (5.8) and (5.9) into (5.7) produces the final form of the weight update equation for the LMS algorithm given by

$$\begin{aligned}\mathbf{w}(l+1) &= \mathbf{w}(l) - \mu[\mathbf{x}(l)\mathbf{x}^H(l)\mathbf{w}(l) - \mathbf{x}(l)s_0^*(l)] \\ &= \mathbf{w}(l) - \mu\mathbf{x}(l)[\underbrace{\mathbf{x}^H(l)\mathbf{w}(l) - s_0^*(l)}_{e^*(l)}] \\ &= \mathbf{w}(l) - \mu e^*(l)\mathbf{x}(l).\end{aligned} \tag{5.10}$$

The weights are estimated iteratively using (5.4) and (5.10).

The MSE is a quadratic function of the weight vector. Thus, the performance surface is a N_r-dimensional quadratic surface [36] where N_r is the number of antenna elements. The surface has a single, global minimum corresponding to the zero-crossing of the gradient of the MSE. In the time varying channel, the minimum of the MSE performance surface and the curvature of the surface will change.

The step size parameter has a significant effect on the convergence of the weight vector. If the step size is too small, convergence will be slow. If the step size is too large, the update of the weights will overshoot the minimum of the MSE and will not converge [36]. It is shown in [37] that stability is assured for a step size constrained to

$$0 < \mu < \frac{2}{\lambda_{\max}}, \tag{5.11}$$

where $\lambda_{\max}$ is the largest eigenvalue of $\mathbf{R_{xx}}$. The constraint in (5.11) can be approximated by

$$0 < \mu < \frac{2}{\mathrm{trace}[\mathbf{R_{xx}}]}. \tag{5.12}$$

In addition to stability, convergence is also assured by these constraints when the received signal statistics are stationary. According to [36], in the case of a time varying channel, "if the convergence is slower than the changing angles of arrival, it is possible that the adaptive array cannot acquire the signal of interest fast enough to track the changing signal".

After the LMS algorithm has converged, its ability to maintain good steady state performance is also dependent on the step size. Because each iteration is based on a single sample, the estimated gradient will be highly dependent on the transmitted symbols. The larger the step size, the more influence the most recent sample has on the weight update. A larger step size will experience worse steady state performance than a smaller step size, even though both step sizes satisfy the requirement of (5.11). Therefore, there is a trade-off between convergence rate and the steady state performance.

5.1.3 Recursive least squares

We follow the derivations given in [38] for the RLS algorithm and apply these concepts to antenna arrays as was done in [36]. The RLS method seeks to estimate a weighted correlation matrix and correlation vector. The weighted estimates are defined as

$$\hat{\mathbf{R}}_{\mathbf{xx}}(l) = \sum_{i=1}^{l} \gamma^{l-i} \mathbf{x}(i)\mathbf{x}^H(i) \tag{5.13}$$

and

$$\hat{\mathbf{r}}_{\mathbf{x}s_0}(l) = \sum_{i=1}^{l} \gamma^{l-i} \mathbf{x}(i) s_0^*(i), \tag{5.14}$$

where γ is the exponential weighting factor constrained to $0 < \gamma \leq 1$. The goal is to generate an iterative approach to solving the optimal MMSE solution for estimated statistics as given by

$$\hat{\mathbf{w}}(l) = \hat{\mathbf{R}}_{\mathbf{xx}}^{-1}(l)\hat{\mathbf{r}}_{\mathbf{x}s_0}(l). \tag{5.15}$$

The correlation matrix and correlation vector are written as a summation over all past samples $1 \leq i \leq l-1$ added to the current sample l as given by

$$\hat{\mathbf{R}}_{\mathbf{xx}}(l) = \gamma \sum_{i=1}^{l-1} \gamma^{l-1-i} \mathbf{x}(i)\mathbf{x}^H(i) + \mathbf{x}(l)\mathbf{x}^H(l) = \gamma \hat{\mathbf{R}}_{\mathbf{xx}}(l-1) + \mathbf{x}(l)\mathbf{x}^H(l) \tag{5.16}$$

and

$$\hat{\mathbf{r}}_{\mathbf{x}s_0}(l) = \gamma \sum_{i=1}^{l-1} \gamma^{l-1-i} \mathbf{x}(i) s_0^*(i) + \mathbf{x}(l) s_0^*(l) = \gamma \hat{\mathbf{r}}_{\mathbf{x}s_0}(l-1) + \mathbf{x}(l) s_0^*(l), \tag{5.17}$$

respectively. In contrast to the DMI method, the inverse of the correlation matrix is estimated directly. This eliminates the need to invert the correlation matrix. Applying the matrix inverse lemma, the correlation matrix inverse is given by

$$\begin{aligned}\hat{\mathbf{R}}_{\mathbf{xx}}^{-1}(l) &= \left(\gamma\hat{\mathbf{R}}_{\mathbf{xx}}(l-1) + \mathbf{x}(l)\mathbf{x}^H(l)\right)^{-1} \\ &= \gamma^{-1}\hat{\mathbf{R}}_{\mathbf{xx}}^{-1}(l-1) - \frac{\gamma^{-2}\hat{\mathbf{R}}_{\mathbf{xx}}^{-1}(l-1)\mathbf{x}(l)\mathbf{x}^H(l)\hat{\mathbf{R}}_{\mathbf{xx}}^{-1}(l-1)}{1+\gamma^{-1}\mathbf{x}^H(l)\hat{\mathbf{R}}_{\mathbf{xx}}^{-1}(l-1)\mathbf{x}(l)}. \qquad (5.18)\end{aligned}$$

The expression of (5.18) enables us to calculate the current estimate of the correlation matrix inverse from the previous estimate and the current received signal vector. A gain vector $\mathbf{g}(l)$ is defined as

$$\mathbf{g}(l) = \frac{\gamma^{-1}\hat{\mathbf{R}}_{\mathbf{xx}}^{-1}(l-1)\mathbf{x}(l)}{1+\gamma^{-1}\mathbf{x}^H(l)\hat{\mathbf{R}}_{\mathbf{xx}}^{-1}(l-1)\mathbf{x}(l)}. \qquad (5.19)$$

Substitution of (5.19) enables us to simplify (5.18) to

$$\hat{\mathbf{R}}_{\mathbf{xx}}^{-1}(l) = \gamma^{-1}\hat{\mathbf{R}}_{\mathbf{xx}}^{-1}(l-1) - \gamma^{-1}\mathbf{g}(l)\mathbf{x}^H(l)\hat{\mathbf{R}}_{\mathbf{xx}}^{-1}(l-1). \qquad (5.20)$$

Rearranging (5.19) produces

$$\begin{aligned}\mathbf{g}(l) &= \gamma^{-1}\hat{\mathbf{R}}_{\mathbf{xx}}^{-1}(l-1)\mathbf{x}(l) - \gamma^{-1}\mathbf{g}(l)\mathbf{x}^H(l)\hat{\mathbf{R}}_{\mathbf{xx}}^{-1}(l-1)\mathbf{x}(l) \\ &= \left[\gamma^{-1}\hat{\mathbf{R}}_{\mathbf{xx}}^{-1}(l-1) - \gamma^{-1}\mathbf{g}(l)\mathbf{x}^H(l)\hat{\mathbf{R}}_{\mathbf{xx}}^{-1}(l-1)\right]\mathbf{x}(l) \\ &= \hat{\mathbf{R}}_{\mathbf{xx}}^{-1}(l)\mathbf{x}(l), \qquad (5.21)\end{aligned}$$

where the expression in (5.21) follows from (5.20). The relationship in (5.21) will be useful in a subsequent expression.

Returning to (5.15), the following substitutions are made

$$\begin{aligned}\hat{\mathbf{w}}(l) &= \hat{\mathbf{R}}_{\mathbf{xx}}^{-1}(l)\hat{\mathbf{r}}_{xs_0}(l) & (5.22)\\ &= \gamma\hat{\mathbf{R}}_{\mathbf{xx}}^{-1}(l)\hat{\mathbf{r}}_{xs_0}(l-1) + \hat{\mathbf{R}}_{\mathbf{xx}}^{-1}(l)\mathbf{x}(l)s_0^*(l) & (5.23)\\ &= \hat{\mathbf{R}}_{\mathbf{xx}}^{-1}(l-1)\hat{\mathbf{r}}_{xs_0}(l-1) - \mathbf{g}(l)\mathbf{x}^H(l)\hat{\mathbf{R}}_{\mathbf{xx}}^{-1}(l-1)\hat{\mathbf{r}}_{xs_0}(l-1) + \hat{\mathbf{R}}_{\mathbf{xx}}^{-1}(l)\mathbf{x}(l)s_0^*(l) & (5.24)\\ &= \hat{\mathbf{w}}(l-1) - \mathbf{g}(l)\mathbf{x}^H(l)\hat{\mathbf{w}}(l-1) + \hat{\mathbf{R}}_{\mathbf{xx}}^{-1}(l)\mathbf{x}(l)s_0^*(l) & (5.25)\\ &= \hat{\mathbf{w}}(l-1) - \mathbf{g}(l)\left[\mathbf{x}^H(l)\hat{\mathbf{w}}(l-1) - s_0^*(l)\right], & (5.26)\end{aligned}$$

where (5.23) follows from the definition of the correlation vector estimate in (5.17), (5.24) follows from the simplified inverse correlation matrix update equation (5.20), (5.25) follows from (5.15) for the previous sample index $(l-1)$, and (5.26) follows from (5.21). The term in brackets in (5.26) is the complex conjugate of the error function defined in (5.4). Making this substitution produces the following form of the weight update equation:

$$\hat{\mathbf{w}}(l) = \hat{\mathbf{w}}(l-1) - \mathbf{g}(l)e^*(l). \tag{5.27}$$

An iteration of the RLS algorithm consists of the following computations:

$$(i) \qquad \mathbf{g}(l) = \frac{\gamma^{-1}\hat{\mathbf{R}}_{\mathbf{xx}}^{-1}(l-1)\mathbf{x}(l)}{1+\gamma^{-1}\mathbf{x}^H(l)\hat{\mathbf{R}}_{\mathbf{xx}}^{-1}(l-1)\mathbf{x}(l)} \tag{5.28}$$

$$(ii) \qquad e(l) = \hat{\mathbf{w}}^H(l-1)\mathbf{x}(l) - s_0(l) \tag{5.29}$$

$$(iii) \qquad \hat{\mathbf{w}}(l) = \hat{\mathbf{w}}(l-1) - \mathbf{g}(l)e^*(l) \tag{5.30}$$

$$(iv) \qquad \hat{\mathbf{R}}_{\mathbf{xx}}^{-1}(l) = \gamma^{-1}\hat{\mathbf{R}}_{\mathbf{xx}}^{-1}(l-1) - \gamma^{-1}\mathbf{g}(l)\mathbf{x}^H(l)\hat{\mathbf{R}}_{\mathbf{xx}}^{-1}(l-1) \tag{5.31}$$

The inverse correlation matrix is initialized by setting $\hat{\mathbf{R}}_{\mathbf{xx}}^{-1}(0) = \nu\mathbf{I}$ where ν is a regularization parameter. In [38] details are given on the effect of ν on the convergence of RLS. The principle given in [38] is that the convergence is improved when ν is a small positive constant for high SNR and a large positive constant for low SNR. We found through simulation that $\nu = 1/100$ provided good performance at an SNR per antenna of 3 dB.

Successive iterations of the RLS algorithm improves the estimated signal statistics. When the received signal statistics are stationary (time invariant channel), all samples are equally useful. Therefore, the exponential weighting factor is set to one so that past samples are not devalued. Because the RLS algorithm is iteratively estimating the signal statistics for a quadratic performance surface, the weights will converge to the optimal weights when the received signal statistics are stationary.

Generally the exponential weighting factor is set to one or close to one [38]. If the exponential weighting factor is too low, the RLS algorithm may never converge. This is because the estimated statistics are not accurate when enough samples are not included in the estimate. In the case of the time varying channel, the exponential weighting factor is useful for de-emphasizing the earlier samples which no longer represent the changing channel.

The RLS algorithm is known to converge more quickly than the LMS algorithm [36]. The RLS weight update in (5.30) has a similar form to the LMS weight update in (5.10). In RLS, more computation is required to determine the vector direction of the weight update and the step size which are determined by the gain vector $\mathbf{g}(l)$, updated every iteration. From a computation perspective, the RLS algorithm is still attractive because it does not require inversion of the correlation matrix as in the DMI method. For an array with 36 elements, the DMI method requires inversion of a 36×36 correlation matrix while the RLS method iteratively updates its inverse directly.

5.2 Channel coherence time

In our system model, we desire to not only track angle of arrival, but also mitigate multipath interference. This requires that the LMS algorithm be able to adapt to the changing phase offsets of the multipath components. Due to the carrier frequency of 60 GHz, the phase offsets change very quickly when compared to the rest of the channel parameters.

The *coherence time* of the channel is “a statistical measure of the time duration over which the channel impulse response is essentially invariant” [11]. An estimate of the coherence time T_C is given by [11]

$$T_C = \frac{0.423}{f_m} \tag{5.32}$$

where f_m is the maximum Doppler shift given by $f_m = v/\lambda_c$ and v and λ_c are the velocity and carrier wavelength, respectively. In this work, we model the transmitter and receiver moving at a velocity of 1 m/s. The maximum relative velocity between the two is 2 m/s. With a carrier frequency of 60 GHz and velocity of 2 m/s, the coherence time is 1.1 ms. At the symbol rate 1 Gsps (Giga symbols per second), this corresponds to 1.1 million symbols.

An example of the time-varying channel gain is shown in Fig. 5.1 for a transmitter and receiver moving at a velocity of 1 m/s each. The four strongest paths are used in the calculation of the channel gain. For this figure, we assume that a sinusoidal waveform with frequency 60 GHz is transmitted. The channel gain is expressed

$$\text{Channel Gain} = 20\log_{10}\left[\left|\sum_{k=0}^{3}\alpha_k e^{j\psi_k}\right|^2\right]. \tag{5.33}$$

The time period for updates to the CIR is expressed T_{chan}.

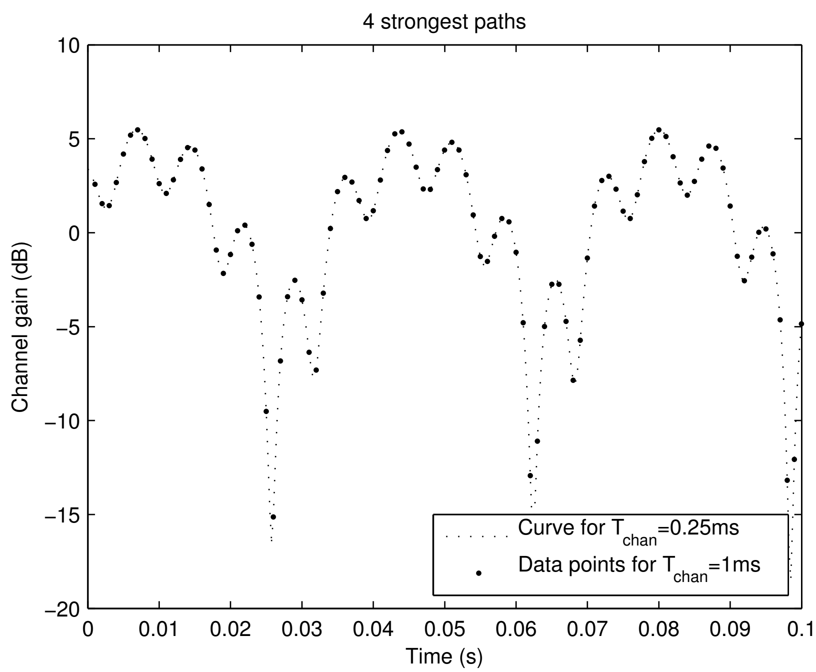

Figure 5.1: Channel gain

5.3 Convergence of the adaptive algorithms

We begin our analysis by considering the convergence of the adaptive algorithms over time intervals much less than the coherence time of the channel. Thus, we assume that the environment is stationary. The stationary case is significant because the rate at which we expect to update the weight vector is much higher than the rate of change in the channel. The CIR is determined using ray tracing and the four strongest paths are used in all implementations of the algorithms and in the calculation of the probability of a bit error.

The modulation is QPSK and the symbol rate is 1 Gsps. The pulse shape is defined over two symbol periods and is zero outside the interval $-T \leq t \leq T$. Beamsteering toward the strongest path is implemented on the transmitter's array. In the indoor environment, the arrays are four by four planar arrays. In the outdoor environment, the arrays are nine by four ('vertical' by 'horizontal') planar arrays.

In order to set the step size for LMS weight update, the algorithm estimates the upper limit of (5.12) from the first received signal sample $\mathbf{x}(1)$. We back off the estimated limit by a factor μ_{fac} so that the step size is given by

$$\mu = \mu_{\text{fac}} \frac{2}{\text{trace}[\mathbf{x}(1)\mathbf{x}^H(1)]}. \tag{5.34}$$

Several values of μ are considered corresponding to $\mu_{\text{fac}} \in \{1/2, 1/15, 1/25, 1/50\}$.

We analyze the convergence of the three adaptive methods for indoor and outdoor channels. The conference room of 460 Durham Hall is depicted in Fig. 5.2. In addition to the walls shown in the figure, the floor and ceiling are modeled in the indoor environment. All walls have a height of 3 meters. The table has a height of 1 meter. Three transmitter (TX) locations and three receiver (RX) locations are shown. RX1 is positioned at 2.75 meters and represents a ceiling mounted projector. RX2 is positioned at a height of 2 meters and represents an HDTV mounted to the wall. RX3, TX1, TX2, and TX3 represent portable devices such as laptops and are located at a height of 1.5 meters. The outdoor environment is shown in Fig. 5.3 along with six TX/RX pairs. These TXs and RXs represent hand-held devices for public safety or military use. Pairs 1, 2, 4, and 5 are at a range of 50 meters. Pairs 3 and 6 are at a range of 25 meters. All devices have heights between 1 and 2 meters. Table 5.1 lists fifteen scenarios for which simulations were run.

5.3.1 Effect of the initial weights on convergence

In the first simulation, LMS and RLS are implemented with three different starting weight vectors. The three starting weight vectors are zeros $\mathbf{w}(0) = [0, 0, 0, \ldots, 0]^T = \mathbf{0}$, omni-

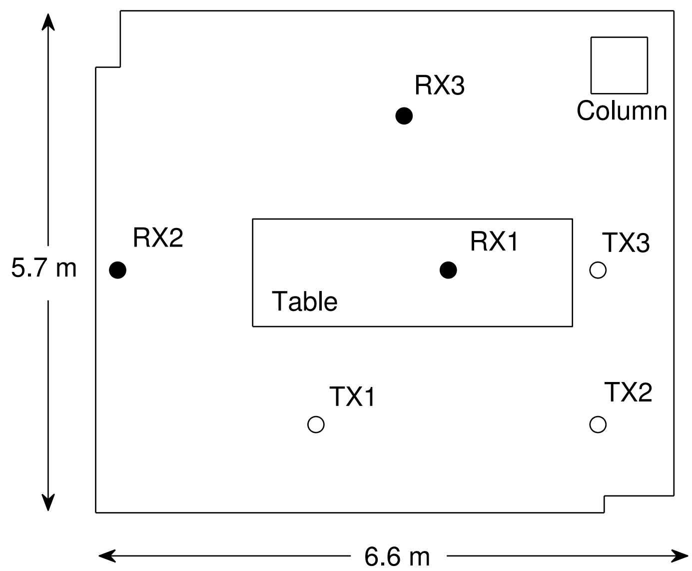

Figure 5.2: Conference room layout with transmitter and receiver locations

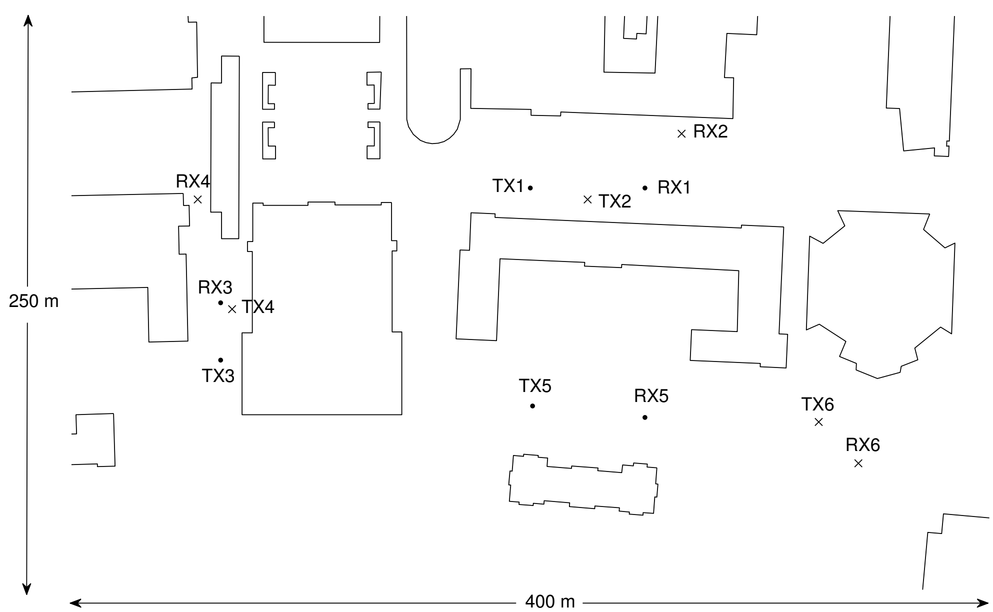

Figure 5.3: Virginia Tech campus layout

Table 5.1: List of scenarios

Label	Environment	RX	TX
I1	Indoor	1	1
I2	Indoor	1	2
I3	Indoor	1	3
I4	Indoor	2	1
I5	Indoor	2	2
I6	Indoor	2	3
I7	Indoor	3	1
I8	Indoor	3	2
I9	Indoor	3	3
O1	Outdoor	1	1
O2	Outdoor	2	2
O3	Outdoor	3	3
O4	Outdoor	4	4
O5	Outdoor	5	5
O6	Outdoor	6	6

directional reception $\mathbf{w}(0) = [1, 0, 0, \ldots, 0]^T$, and beamsteering $\mathbf{w}(0) = \mathbf{v}_0$. This provides insight into the sensitivity of the algorithms to the starting weights. The beamsteering case enables us to determine potential benefit that would result from knowledge of the transmitter's position or the angle of arrival of the LOS path. A complete set of simulation results are given in Appendix A. In this section, we include figures from scenarios which are representative of the results.

Convergence simulations of the LMS algorithm in scenarios I1 and O4 are shown in Figs. 5.4 and 5.5, respectively. With initial weight vector $\mathbf{w}(0) = \mathbf{0}$, the LMS algorithm typically converges within 100 iterations indoors and within 250 iterations outdoors. In contrast, the

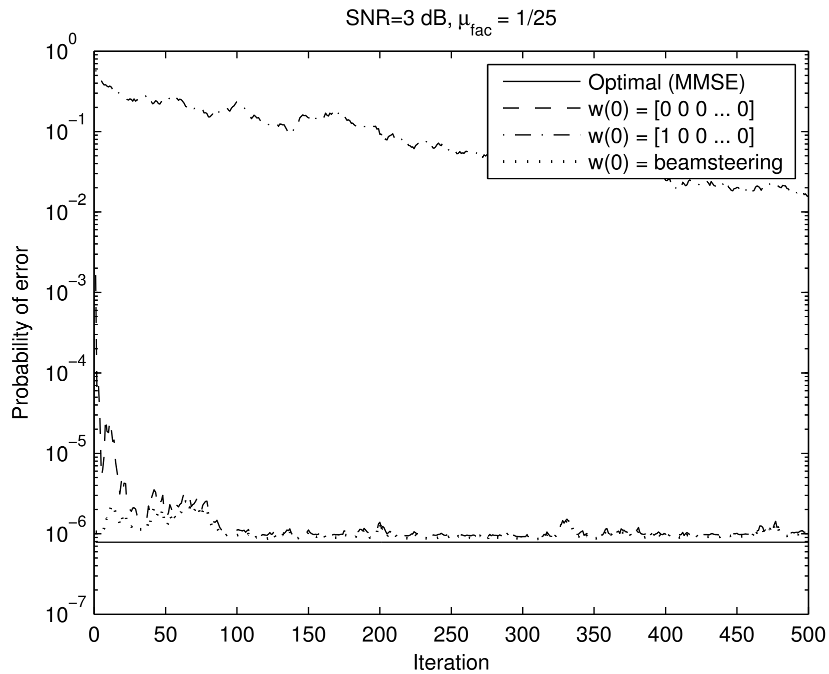

Figure 5.4: Effect of $\mathbf{w}(0)$ on the convergence of LMS for scenario I1

omni-directional initial weight vector requires 1000 or more iteration before converging to steady state. In the indoor scenario, using beamsteering to set the initial weights generally leads to the LMS algorithm starting with a lower probability of error over the first 50 to 100 iterations. In the outdoor scenarios, starting with either $\mathbf{w}(0) = \mathbf{0}$ or beamsteering leads to the same convergence rate in most cases. Two exceptions are scenarios O3 and O6 (see Figs. A.12 and A.15), where starting with beamsteering leads to the performance converging approximately 50 iterations faster than that of $\mathbf{w}(0) = \mathbf{0}$.

Convergence simulations of the RLS algorithm in scenarios I1 and O4 are shown in Figs. 5.6 and 5.7, respectively. The RLS algorithm demonstrates similar convergence behavior to LMS with each of the starting weight vectors. Indoors, the beamsteering weights often provide performance very near to the theoretical MMSE. In these cases, when beamsteering is used as the initial weight vector, very little adaptation is required. In contrast when beamsteering does not provide performance near the theoretical MMSE, convergence is at

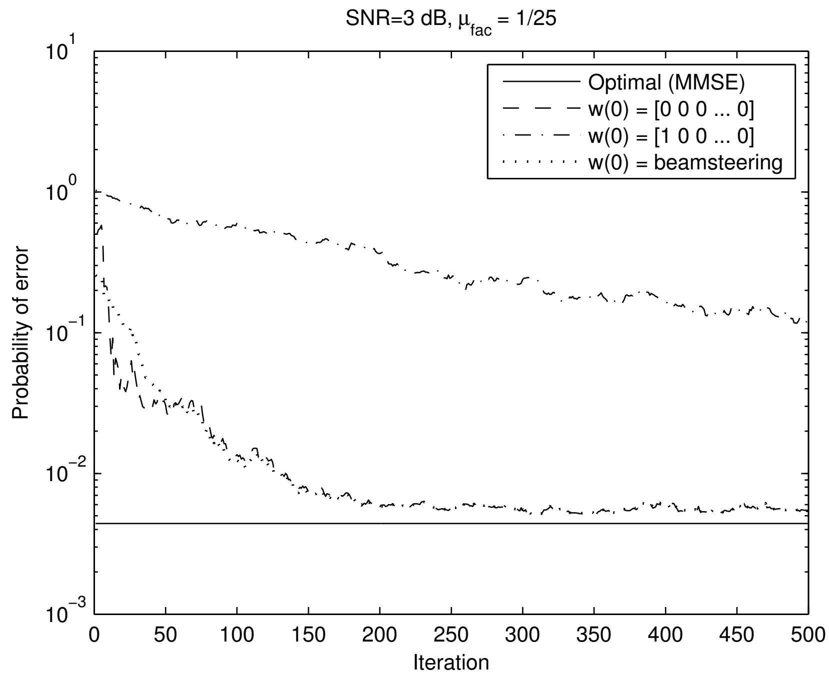

Figure 5.5: Effect of $\mathbf{w}(0)$ on the convergence of LMS for scenario O4

the same rate or slower compared to using $\mathbf{w}(0) = \mathbf{0}$. Scenarios I7, I8, and O2 represent cases where initializing with beamsteering leads to slower convergence (see Figs. A.22, A.23, and A.26).

Overall, $\mathbf{w}(0) = \mathbf{0}$ is a good selection for the initial weights. Beamsteering does not guarantee improvement in the convergence. In the cases that beamsteering does lead to an improvement, it is not substantial enough to warrant the additional effort required to obtain this information. Scenarios I4, O1, and O5 (see Figs. A.4, A.10, A.14, A.19, A.25, and A.29) show the algorithms obtaining P_b lower than that of the theoretical MMSE. This is because MMSE does not guarantee minimum P_b as addressed in Section 4.3.

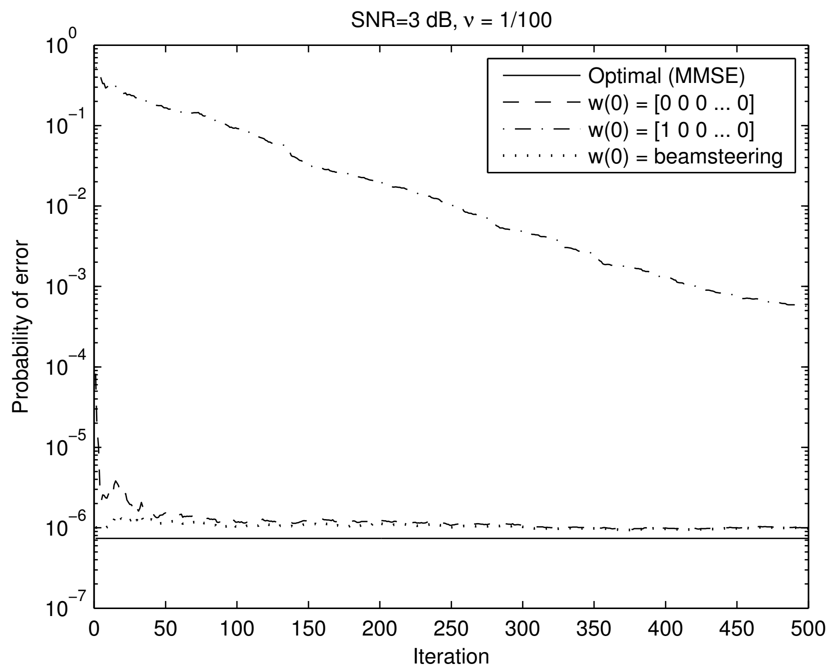

Figure 5.6: Effect of $\mathbf{w}(0)$ on the convergence of RLS for scenario I1

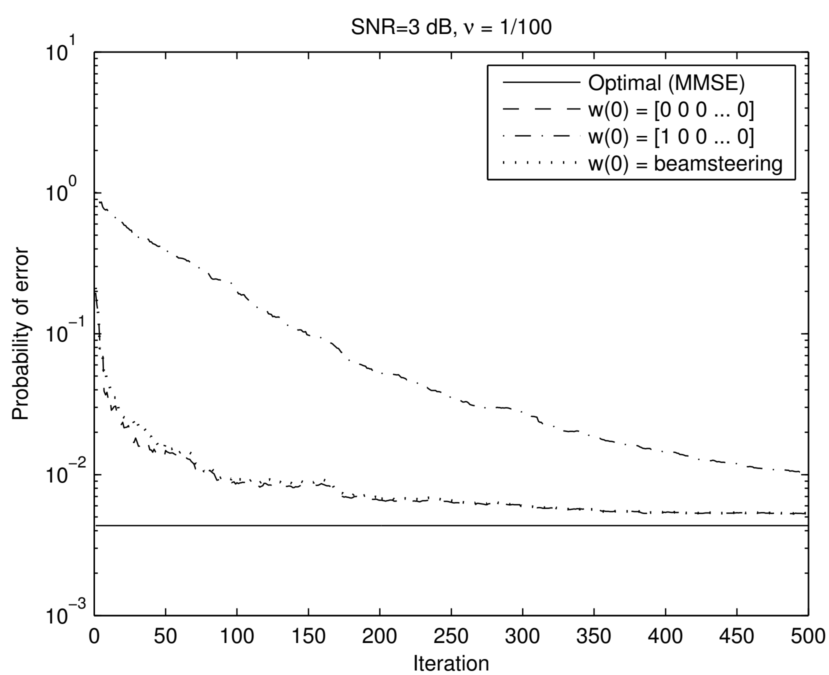

Figure 5.7: Effect of $\mathbf{w}(0)$ on the convergence of RLS for scenario O4

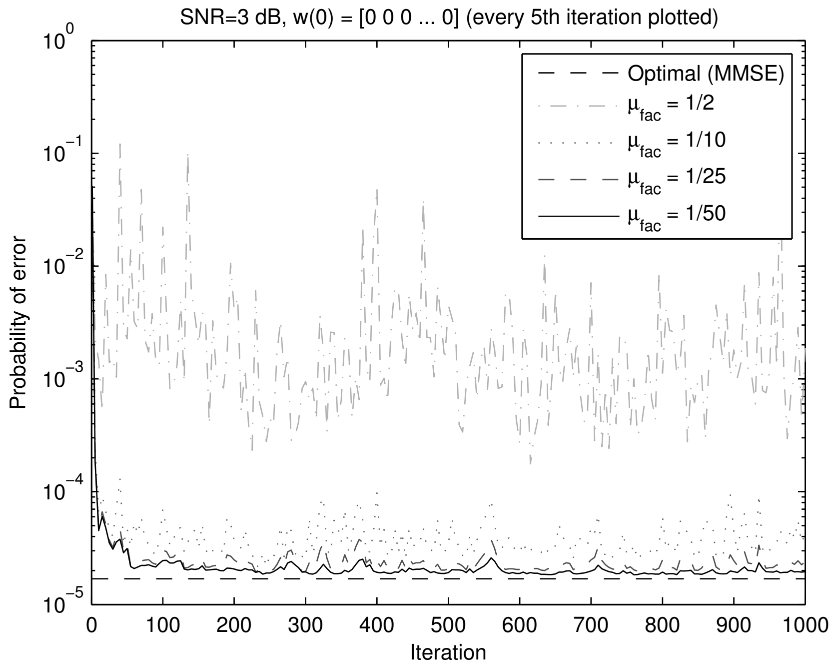

Figure 5.8: Effect of μ on the convergence of LMS for scenario I5

5.3.2 Effect of the step size parameter on the convergence of LMS

In this section, we consider the effect of the choice of the step size parameter μ on the convergence of the LMS algorithm. The value of the μ determines a trade-off between the convergence rate and the steady state performance. The convergence of LMS is shown in Fig. 5.8 for scenario I5 and in Fig. 5.9 for scenario O4. A complete set of figures for this simulation are presented in Appendix B.

The step size μ is controlled with the value of μ_{fac} as shown in (5.34). With $\mu_{\text{fac}} = 1/2$ the LMS algorithm does not converge. Because we use a rough estimate of the upper limit on the step size, this result is not unexpected. For μ_{fac}=1/10, 1/25, and 1/50 the LMS algorithm does consistently converge to the optimal solution. In the indoor environment, the benefit of the larger step size is not apparent in terms of convergence rate. With the smallest scale factor of 1/50 the LMS algorithm demonstrates a good convergence rate. In the outdoor environment, the benefit of the larger scale factor is visible. On the left hand

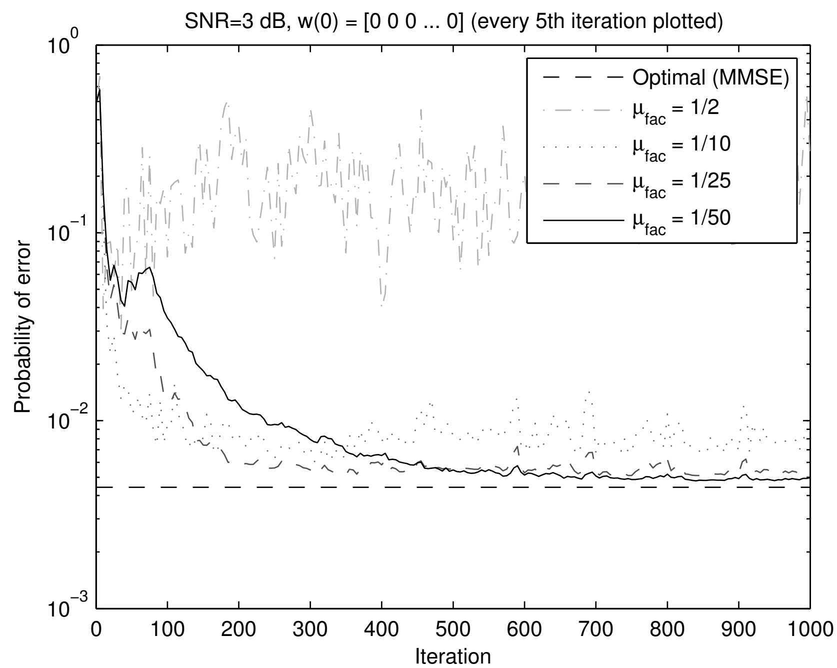

Figure 5.9: Effect of μ on the convergence of LMS for scenario O4

side of Fig. 5.9 – between 1 and 100 iterations – the larger scale factors (with the exception of 1/2) converge more quickly and provide better performance. On the right hand side of the figure – after 500 iterations – the algorithm achieves a better steady state performance with a smaller scale factor. We use a scale factor of 1/25 throughout the remainder of this chapter.

5.3.3 Comparison of DMI, LMS, and RLS

In this section, the P_b performance of each adaptive method is compared with respect to the number of samples or iterations. A complete set of simulations is presented in Appendix C. Here we present the results for scenario I3 in Fig. 5.10 and for scenario O3 in Fig. 5.11.

The DMI method does not provide good results unless approximately 20 samples for the indoor environments and 50 samples for the outdoor environments are used in the estimation. As discussed in Section 5.1.1, with a small number of samples, the matrix inversion of $\mathbf{R_{xx}}$ in

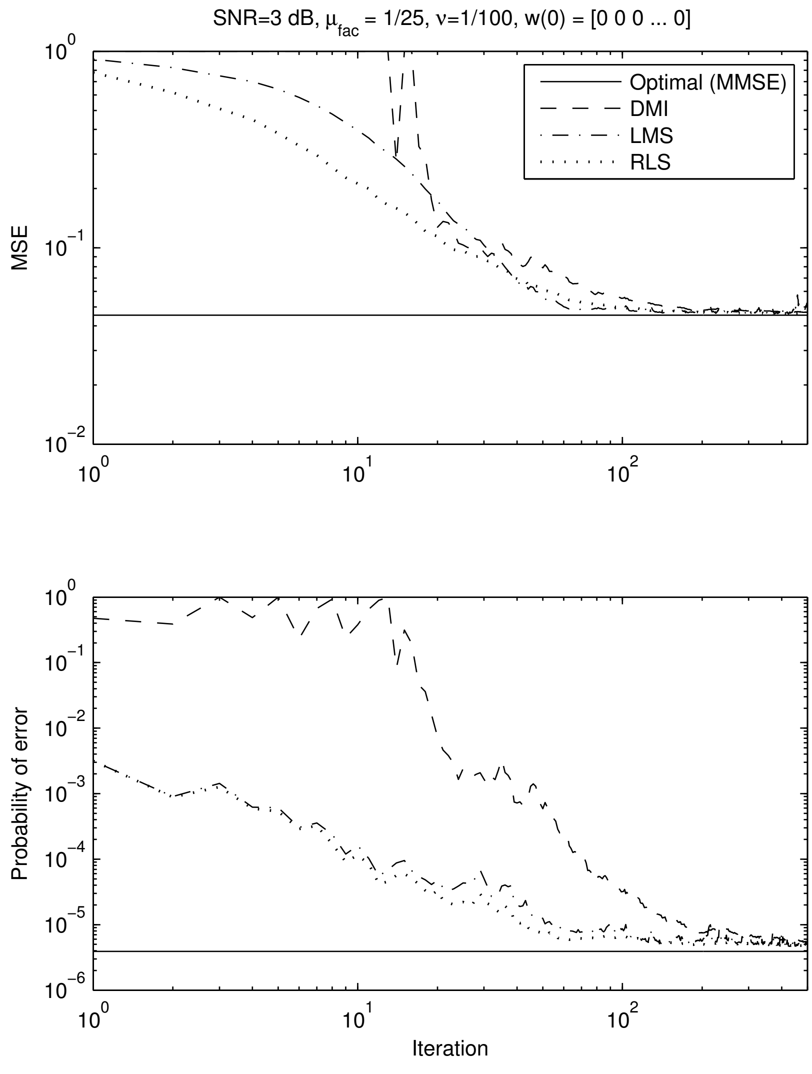

Figure 5.10: Comparison of convergence for scenario I3

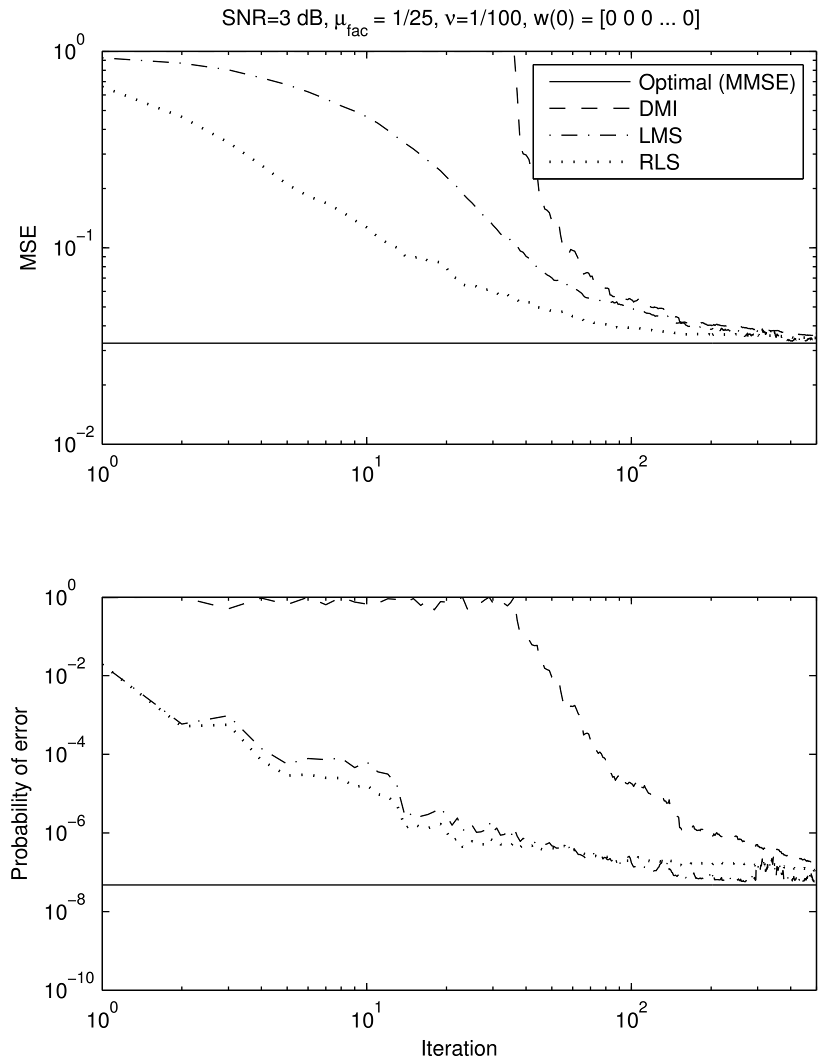

Figure 5.11: Comparison of convergence for scenario O3

the DMI method suffers from scaling issues and the potential for a singular correlation matrix. As expected, with more samples, the correlation of the noise in the diagonal elements of the correlation matrix aids in the inversion of the matrix. If the number of samples available for estimation is insufficient, diagonal loading is a simple method which can be implemented to avoid singular or near singular matrices [44].

As expected, RLS converges more quickly than LMS in terms of MSE. However, the P_b achieved by LMS and RLS during convergence is very similar. Two scenarios where RLS outperforms LMS in terms of P_b are O4 and O6 (shown in Figs. C.13 and C.15). Also, in scenarios O1 and O5, where the algorithms achieve a P_b lower than that of the theoretical MMSE, RLS converges more quickly in terms of P_b.

When the LMS algorithm reaches steady state, the P_b typically does not fluctuate substantially. Three realizations in which the P_b does fluctuate at steady state include the results of scenarios I4, O1, and O5 provided in Figs. C.4, C.10, and C.14. The RLS algorithm consistently has a good steady state performance.

5.4 Adaptive convergence in the time varying channel

In this section, we simulate the performance of the adaptive methods in a time varying channel. The channel is simulated via ray tracing for each iteration. In our simulations we setup the adaptive algorithms to perform iterations at a rate of $R_{\text{iter}} = 1 \times 10^6$ iterations/s. A two element antenna array implementing the LMS algorithm is demonstrated in [45] where the designed system performs iterations of the LMS algorithm at a rate of 25×10^6 iterations/s. Our rate is chosen in order to account for additional complexity with a 16 or 36 element array. Thus, the CIR is modeled at steps of 1 μs. Although the algorithms perform iterations every 1000 symbols, only a single sample is used in estimating the signal statistics as presented in Section 5.1.

Simulations were performed for each of the scenarios described in Section 5.3. The per-

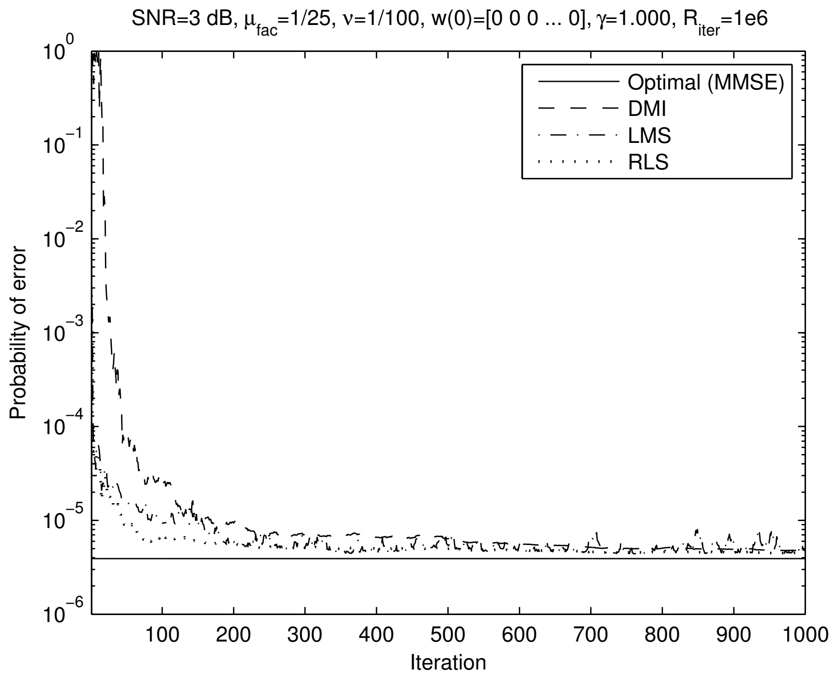

Figure 5.12: Time varying simulation for scenario I3

formance over 1000 iterations are shown for scenarios I3 and O6 in Figs. 5.12 and 5.13, respectively. As can be seen in these figures, the adaptive algorithms are capable of tracking the changing channel. The optimal probability of error is effectively constant over the 1 ms time interval which is approximately the coherence time of the channel.

A layout is shown in Fig. 5.14 which has been specifically designed so that a significant change in the CIR will occur during the simulation. The transmitter is moving toward the receiver at a velocity of 1 m/s and the receiver is stationary. At the starting point, the CIR consists of the LOS and four reflected components: the path shown with a single reflection, the path shown with two reflections, and a ground bounce path overlaying the single reflection path. Halfway through the simulation, two additional paths appear: the new path shown at the ending location and a ground bounce path which overlays this one. The range between the transmitter and receiver begins at 50 m. The total number of iterations is 1000. We consider two exponential weighting factors for the RLS algorithm. The performance with

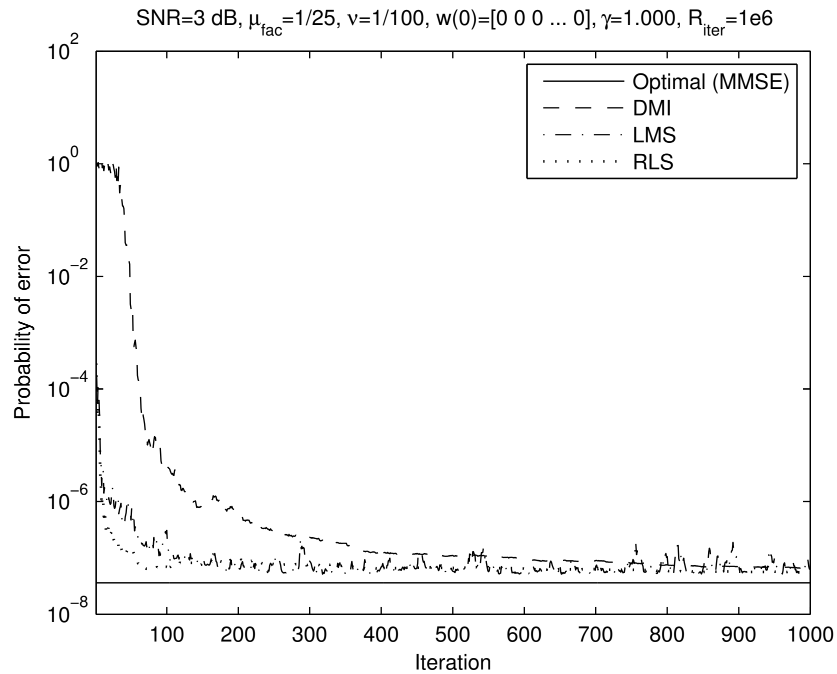

Figure 5.13: Time varying simulation for scenario O6

$\gamma = 1$ is shown in Fig. 5.15 and the performance with $\gamma = 0.995$ is shown in Fig. 5.16. The results demonstrate that all three methods are able to adapt to the changing phase of the multipath interference as well as quickly respond to the new multipath components. For the RLS method, γ is a useful parameter in the time varying channel. On the right hand side of Fig. 5.16, the RLS algorithm converges more quickly by devaluing past samples. However, RLS performs better prior to the introduction of the new multipath components when all samples are equally weighted with $\gamma = 1$.

The choice of $R_{\text{iter}} = 1 \times 10^6$ is arbitrary. For any rate higher than this, the result is the same; there is no change in the optimal probability of error and the adaptive methods are capable of tracking the channel. However, for a rate of $R_{\text{iter}} = 1 \times 10^5$, the optimal probability of error does change over 1000 iterations ($10 \times T_C$). The adaptive methods are still able to track this change. Because the channel changes very slowly relative to the data rate of the system, we believe a decision-directed approach may be a viable solution for single carrier

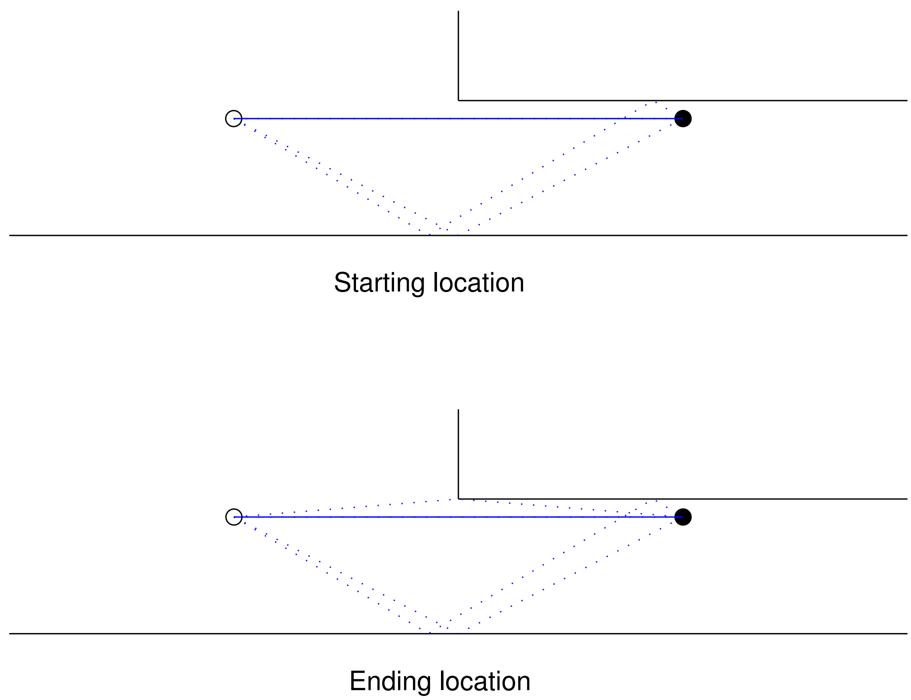

Figure 5.14: Outdoor layout for the time varying channel simulation. The transmitter (open dot) is moving toward the receiver (solid dot) at a speed of 1 m/s. The entire simulation covers 1 mm of movement. Halfway through the simulation new multipath components begin to arrive at the receiver.

systems operating in the 60 GHz band. After the initial acquisition of the array weights, a decision-directed approach based on the LMS algorithm could maintain the weight vector with no loss in spectral efficiency. If the error rate of the system suddenly increased or crossed a threshold, this could trigger a training packet to be transmitted for weight update.

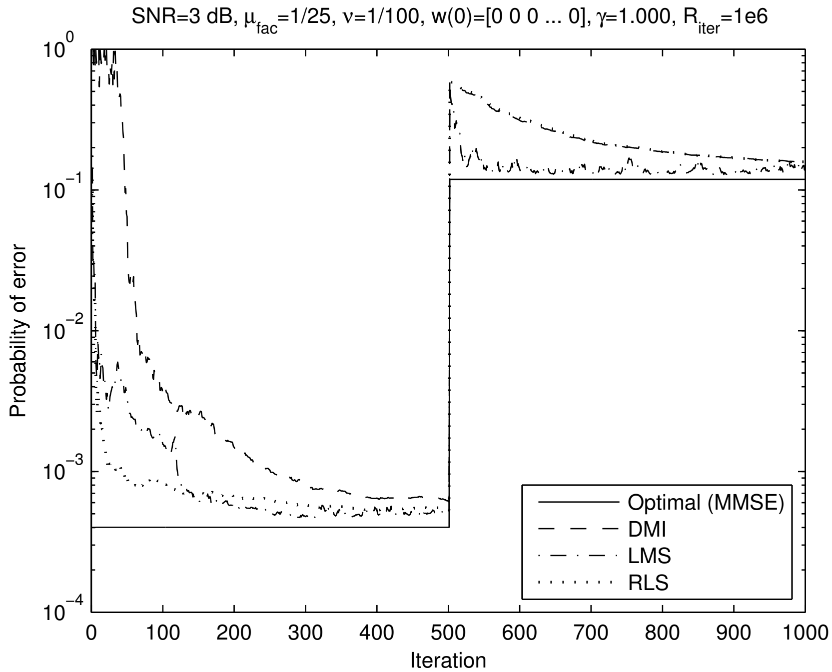

Figure 5.15: Time varying simulation with $\gamma = 1$

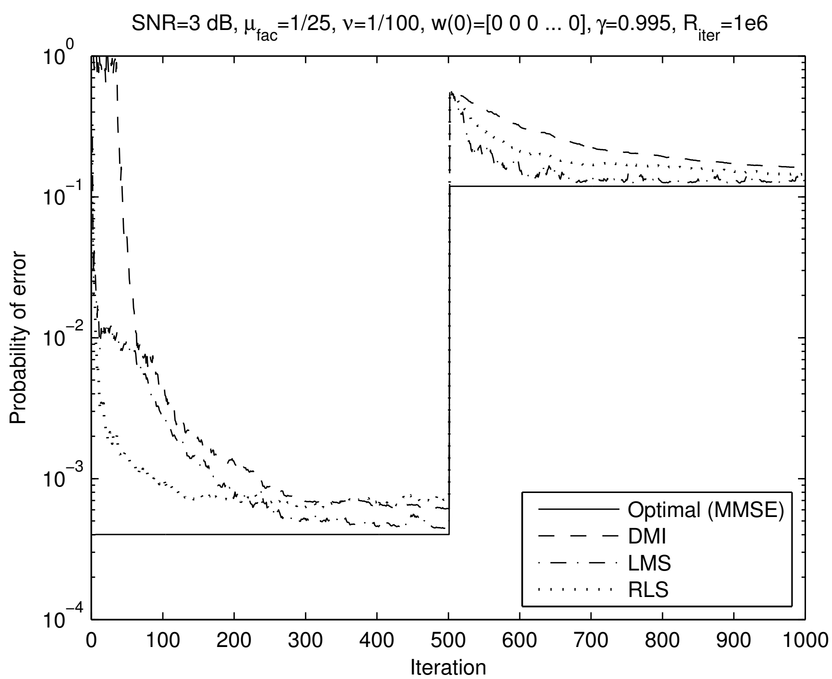

Figure 5.16: Time varying simulation with $\gamma = 0.995$

5.5 Regular weight update performance

In the previous section, we concluded that the adaptive algorithms are capable of tracking the channel when the weights are continuously updated. Knowing that near optimal weights can be acquired, we now investigate regular updates to the weights. Rather than continuously updating the weight vector, we seek to maintain near optimal performance while updating the weights at regular intervals of time.

The transmitter and receiver move at a velocity of 1 m/s in each scenario (the positions of RX1 and RX2 indoors are fixed). The CIR is simulated at time steps of 1 ms to match the channel coherence time. The weights are updated at a regular time interval denoted by T_{upd}. The performance between updates is compared with the optimal performance given continuous weight updates. The paths traveled in the indoor scenarios are shown in Fig. 5.17. The directions traveled in the outdoor scenarios are shown in Figs. 5.18, 5.19, and 5.20. In all scenarios, simulations are run for a duration of 2 seconds.

5.5.1 Analysis of the effect of T_{upd} on performance

In this simulation, we are specifically interested in the effect that T_{upd} has on our ability to track the time varying channel. Update intervals considered include $T_{\text{upd}} \in \{500, 100, 50, 10, 1\}$ ms. With $T_{\text{upd}} = 1$ ms, the weights are updated at each CIR update. The probability of error is calculated for all time steps using the most recent weight update. In order to isolate the effect of T_{upd}, we begin by assuming that the optimal MMSE weight vector is obtained at each update.

In the conference room, the scenarios with RX3 (I7, I8, and I9) resulted in the most rapid change in the channel. The performance for scenarios I7, I8, and I9 is shown in Figs. 5.21, 5.22, and 5.23, respectively. The performance strongly depends on the geometry of the environment. In Fig. 5.21, TX1 and RX3 are directly across from each other at 0.5 seconds. While the transmitter and receiver pass each other, the relative motion between them is

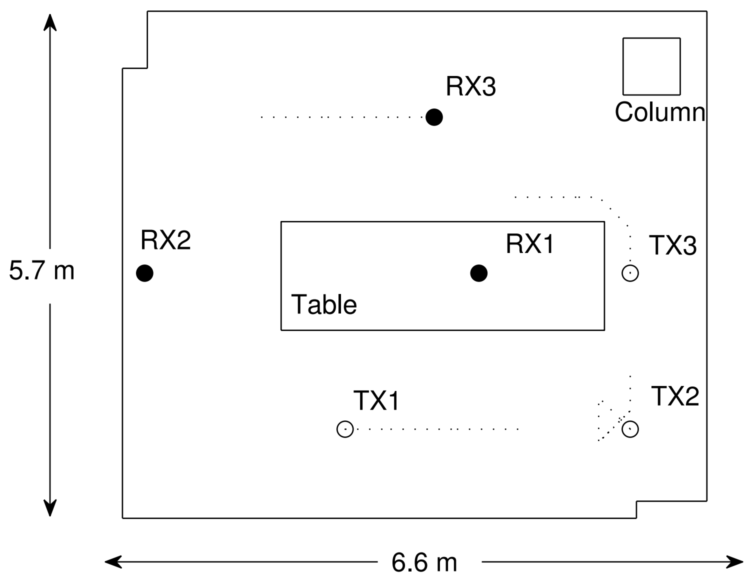

Figure 5.17: Indoor mobile simulations

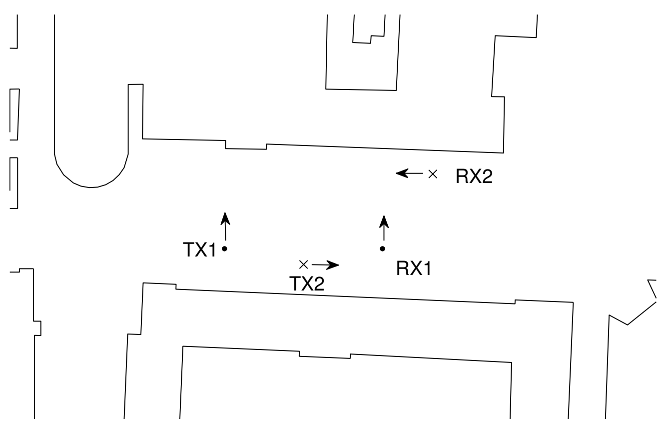

Figure 5.18: Outdoor mobile simulations for scenarios O1 and O2

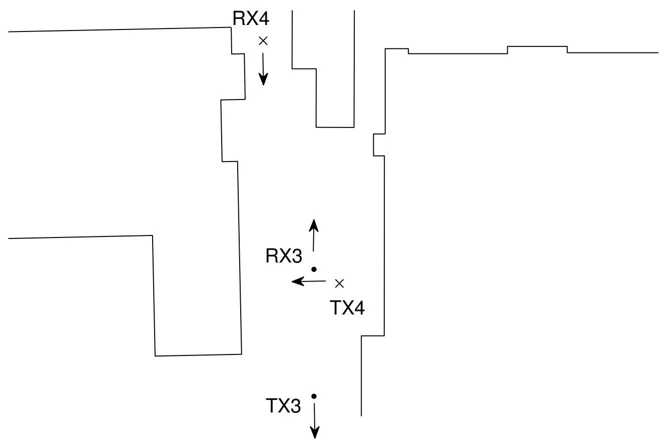

Figure 5.19: Outdoor mobile simulations for scenarios O3 and O4

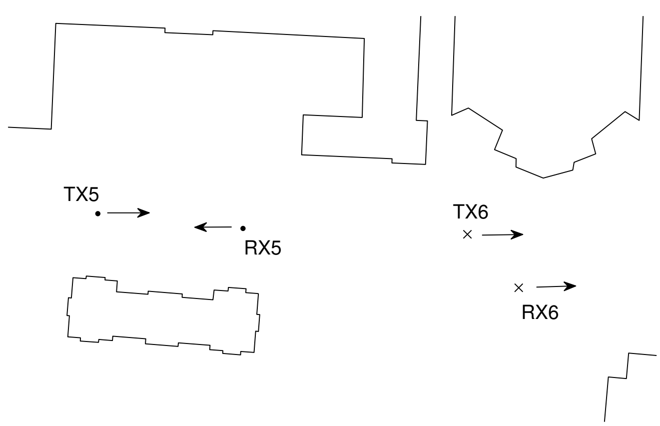

Figure 5.20: Outdoor mobile simulations for scenarios O5 and O6

slow. As the simulation progresses the relative motion between the transmitter and receiver increases. The effect on the performance is seen in how rapidly the optimal performance changes. In Fig. 5.23, the probability of error is observed fluctuating very rapidly at 0.3 seconds. This corresponds to the time when the devices are moving with perpendicular directions. This is the highest rate of change that we observed in our simulations. Fig. 5.24 displays a close up of the segment of interest from scenario I9. During the segment of the simulation between 0.2 and 0.34 seconds, the optimal weights do not completely mitigate all multipath interference. The result is that the phase of this interfering multipath component changes as the transmitter and receiver move. The interference cycles through constructive and destructive summation. However, the optimal weights remain relatively unchanged.

The MMSE weight vector mitigates interfering multipath components. As the angle of arrival changes, the interference is re-introduced. If the optimal weights effectively mitigate the interference, then the performance over time is not dependent on the changing phases of the multipath components. The requirement for updating the weights then becomes the changing angles of arrival which vary much more slowly than the phases.

The performance for scenario O5 is shown in Fig. 5.25. In this scenario, the ground bounce multipath component is correlated with the strongest path. The MMSE weights detect this correlation and seek to constructively add the ground bounce signal. This requires correction of the phase offset of the ground bounce and therefore requires tracking of the phase. The phase change of the ground bounce relative to the LOS is capable of being tracked with regular weight updates.

Overall, we found that continuous weight update is not necessary for maintaining optimal performance. The worst case scenarios have been presented here. The simulations demonstrate that $T_{\text{upd}} = 10$ ms leads to a negligible loss in performance over continuous weight update. The increase in probability of error with $T_{\text{upd}} = 50$ ms or 100 ms, is generally less than an order of magnitude and is often negligible for the scenarios with a lower rate of change.

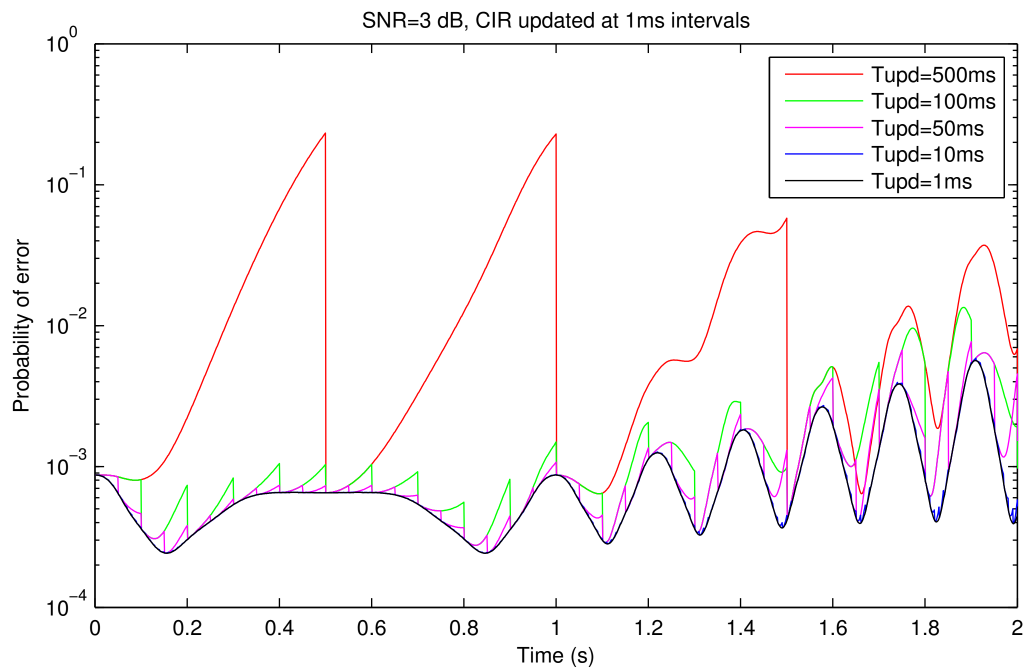

Figure 5.21: Performance for regular weight update in scenario I7

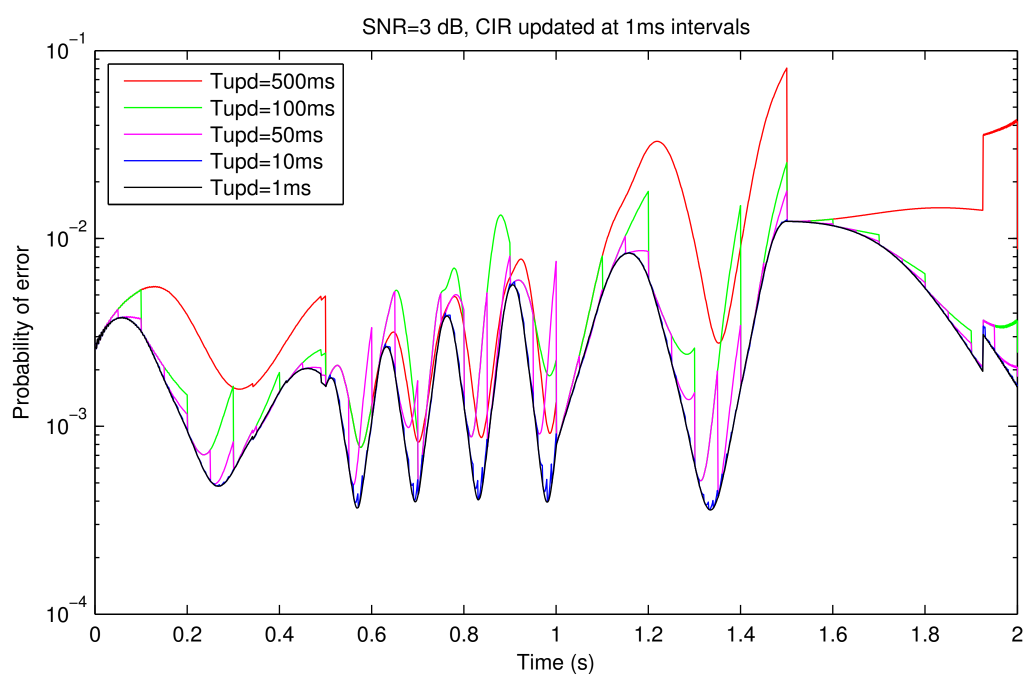

Figure 5.22: Performance for regular weight update in scenario I8

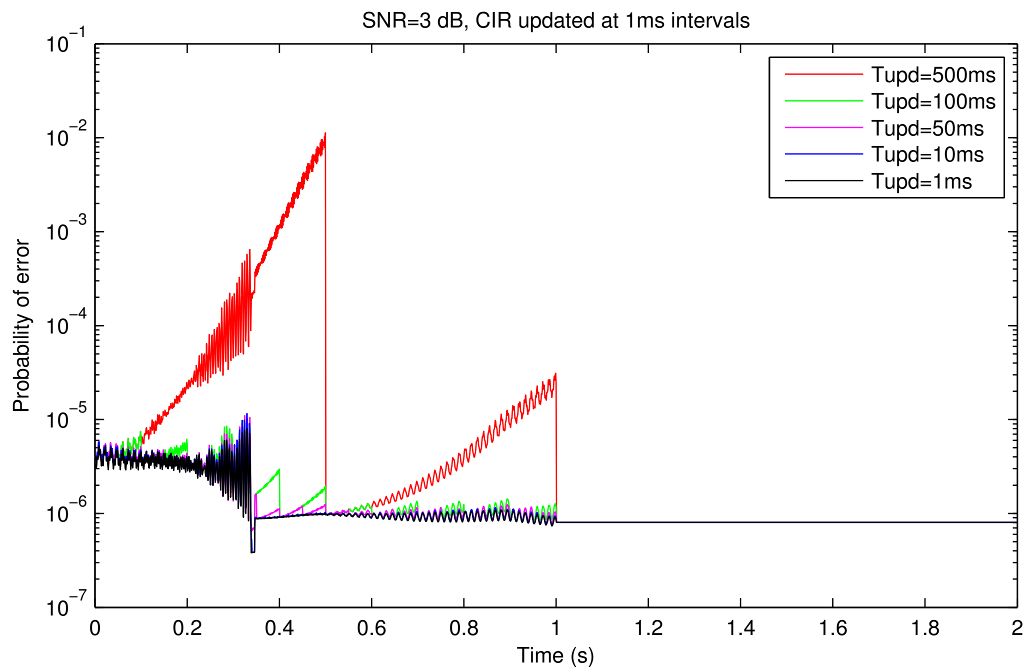

Figure 5.23: Performance for regular weight update in scenario I9

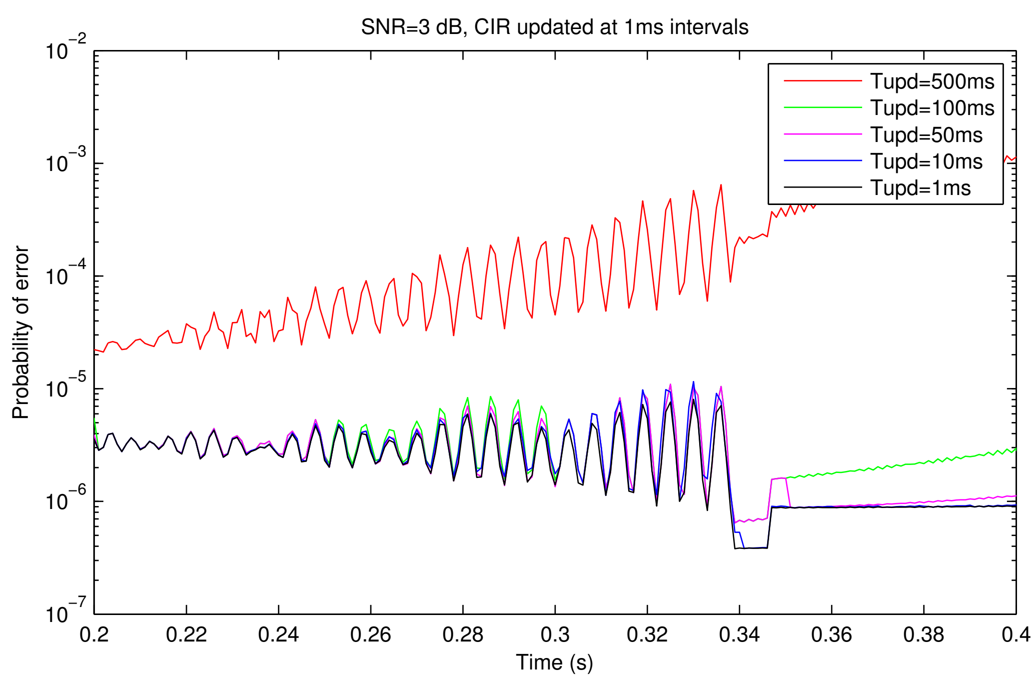

Figure 5.24: Close up of performance for regular weight update in scenario I9

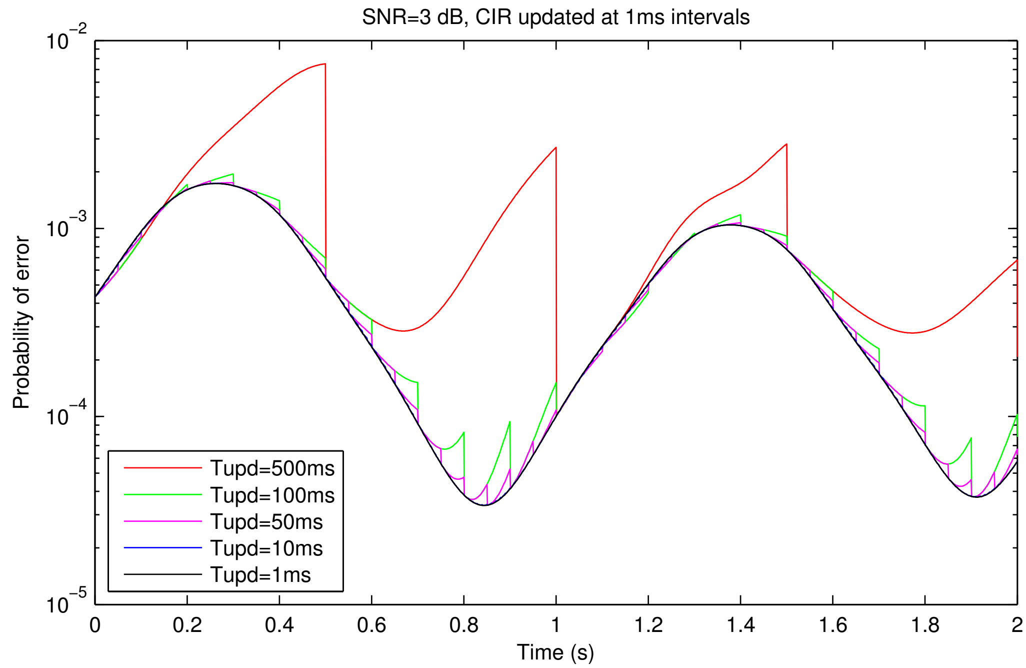

Figure 5.25: Performance for regular weight update in scenario O5

5.5.2 LMS performance

In order to analyze the performance of the LMS algorithm in regularly updating the weight vector, we maintain a constant interval of update at $T_{\text{upd}} = 50$ ms. In this simulation the number of iterations that the LMS algorithm performs per update is varied over the set $N_{\text{iter}} \in \{50, 100, 250, 500, 1000\}$. Based on the convergence results of Section 5.3, the LMS algorithm converges within approximately 100 iterations indoors and 250 iterations outdoors. The weight vector from the previous update is used as the initial weight vector in the current update. Using the previous weight vector in this way improves the performance over time and reduces the need for a high number of iterations at each update. Compare the performance in Fig. 5.26, where the previous weights are used, with the performance in Fig. 5.27, where the initial weight vector in each update is set to a vector of zeros.

Cases where the MMSE weights do not achieve the minimum P_b have been observed in Section 5.3. The results of Section 5.3 demonstrate that, in some cases, the weight vector at earlier

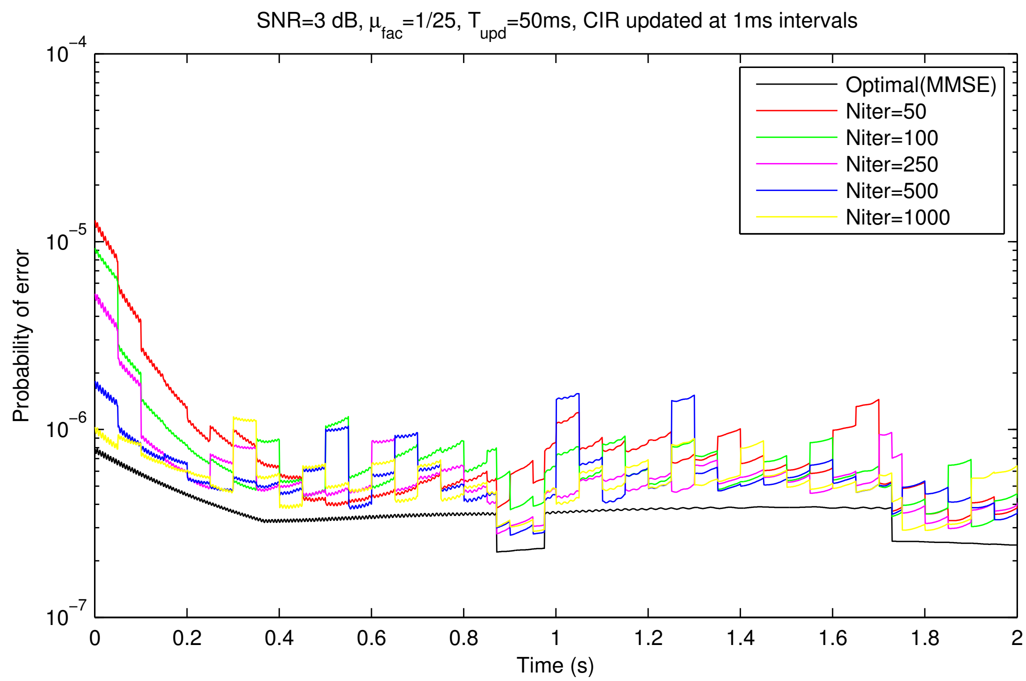

Figure 5.26: LMS performance in scenario I1 with regular weight update using previous weights

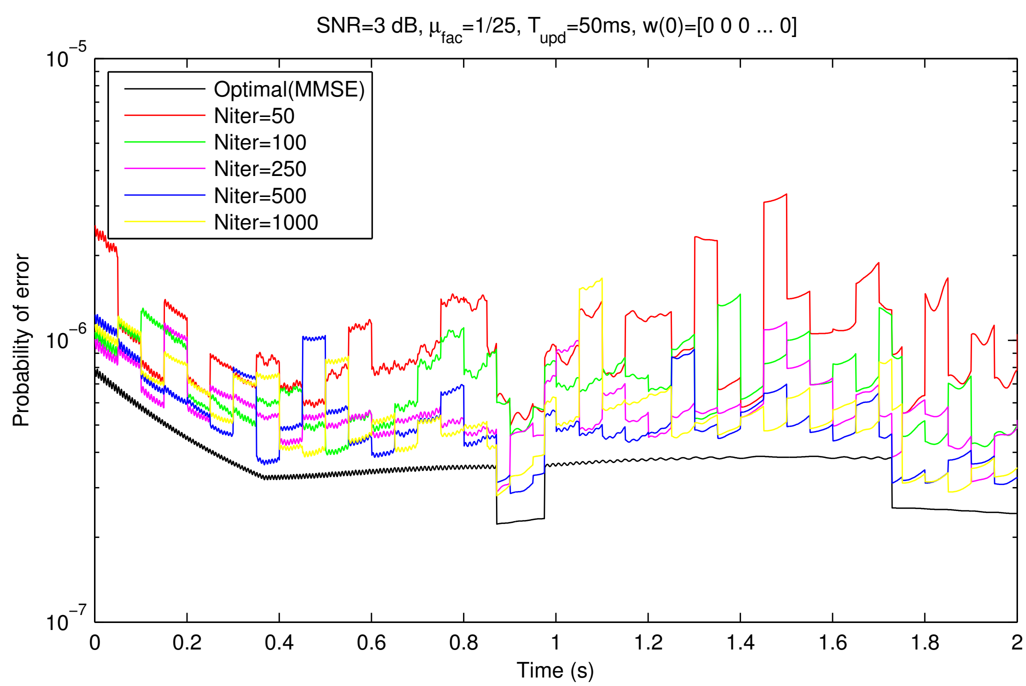

Figure 5.27: LMS performance in scenario I1 with regular weight update with $\mathbf{w}(0) = \mathbf{0}$

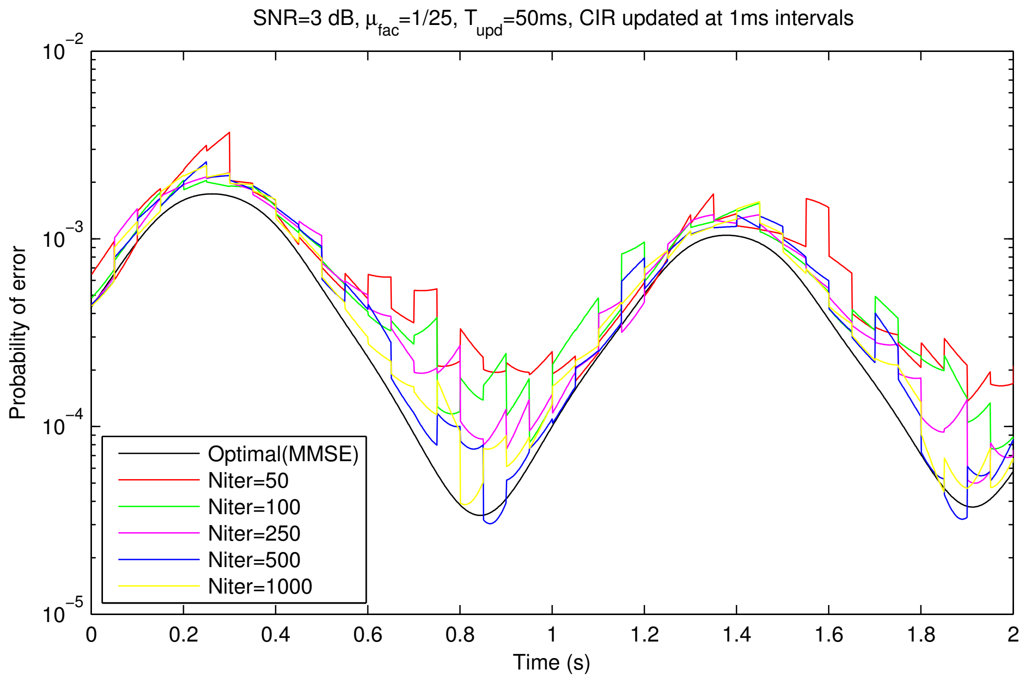

Figure 5.28: LMS performance in scenario O5 using previous weights

iterations of the LMS algorithm achieve a lower P_b than the weight vector at later iterations when the LMS algorithm has converged to the MMSE solution. Compare the performance in Fig. 5.28 with the performance in Fig. 5.29. The previous weight vector initializes the LMS algorithm closer to the MMSE weights. When the weight vector is initialized as the zeros vector, the algorithm achieves a performance better than MMSE before converging to the MMSE weight vector. This is observed in Fig. 5.29 where the largest number of iterations ($N_{\text{iter}} = 1000$) produces a performance nearest to the MMSE performance. When the multipath components constructively add (regions of lower P_b) performance is better with fewer iterations. However, the average P_b will be dominated by the regions of higher P_b where fewer iterations produce very poor performance.

The trade-off between the parameters T_{upd} and N_{iter} is analyzed by fixing the total number of iterations to $N_{\text{iter}}/T_{\text{upd}} = 10\,000$ iterations/s. The performance is compared for three sets of parameter values $\{T_{\text{upd}} = 100\text{ms},\ N_{\text{iter}} = 1\,000\}$, $\{T_{\text{upd}} = 50\text{ms},\ N_{\text{iter}} = 500\}$, and

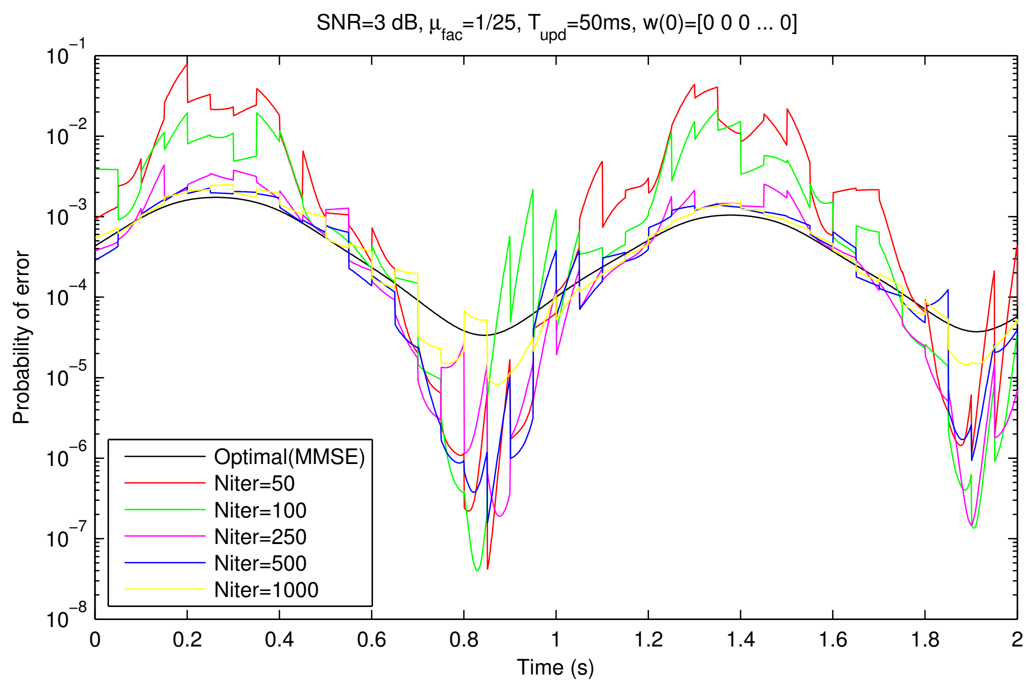

Figure 5.29: LMS performance in scenario O5 with $\mathbf{w}(0) = \mathbf{0}$

$\{T_{\text{upd}} = 10\text{ms}, N_{\text{iter}} = 100\}$. As demonstrated by the results for scenario I5 in Fig. 5.30, we do not observe a significant difference in the performance with each parameter set. This result could be anticipated because each update of the LMS algorithm makes use of the final weight vector from the previous update. Thus, for a fixed number of iterations per second, the performance is consistent across a range of update intervals and iteration values. Taking the mean performance over time for each scenario we find that the probability of error is on the same order of magnitude for each set and that no particular set consistently outperforms the others.

5.5.3 RLS performance

In order to analyze the performance of the RLS algorithm in regularly updating the weight vector, we maintain a constant interval of update at $T_{\text{upd}} = 50$ ms. In this simulation the number of iterations that the RLS algorithm performs is varied over the set $N_{\text{iter}} \in$

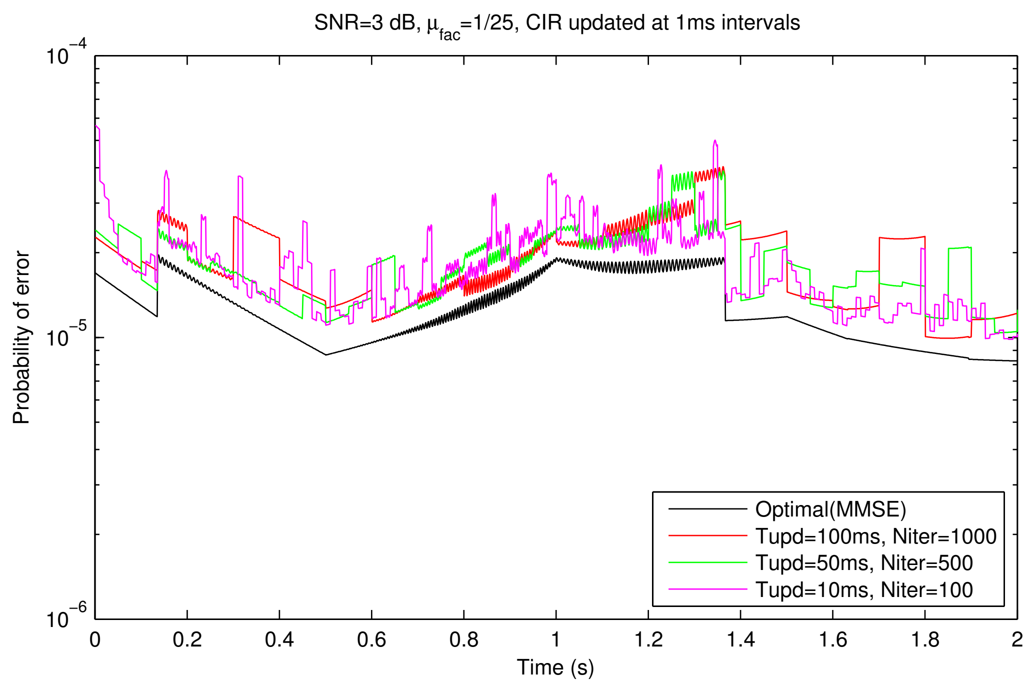

Figure 5.30: LMS performance in scenario I5 with fixed number of iterations/s

$\{50, 100, 250, 500, 1000\}$. The performance for scenarios I6 and O3 are shown in Figs. 5.31 and 5.32, respectively. For the indoor environments we found that good performance is possible with as few as 50 iterations per update. This agrees with the results in Section 5.3. Scenario O3 represents a channel in which a large number of iterations are required to approach the MMSE performance. Even in this case, 50 iterations is sufficient to obtain a P_b within one order of magnitude of the MMSE performance.

To analyze the trade-off between T_{upd} and N_{iter} for RLS we repeat the analysis conducted for LMS. Figs. 5.33 and 5.34 display the results for the trade-off in scenarios I3 and O3, respectively. We find that, indoors, the performance is not significantly affected by the trade-off because good performance can be achieved with 50 iterations. In outdoor environments, the performance of RLS, for the chosen parameter sets, is more sensitive to the number of iterations per update N_{iter} than it is to the weight update period T_{upd}.

In the simulations presented in this section, the previous weight vector is used to initialize

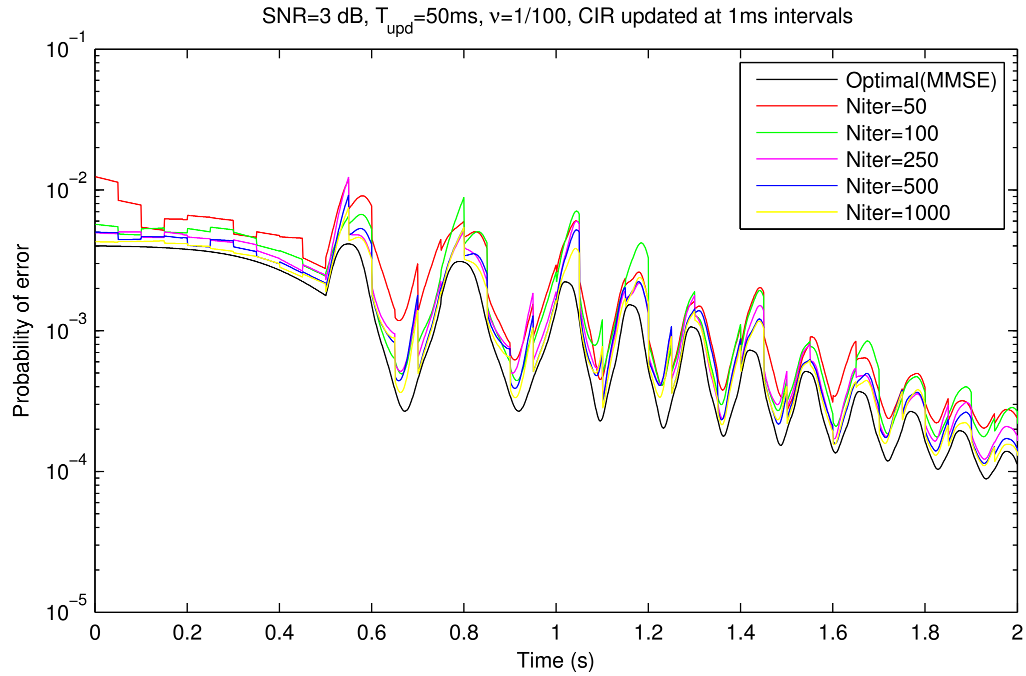

Figure 5.31: RLS performance in scenario I6 with regular weight update

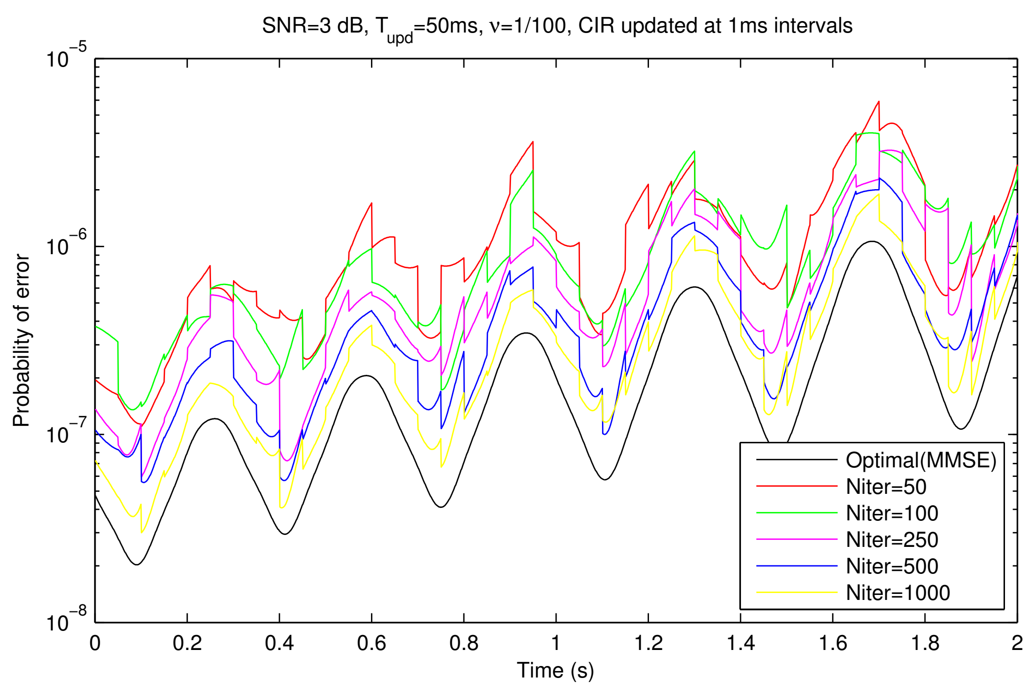

Figure 5.32: RLS performance in scenario O3 with regular weight update

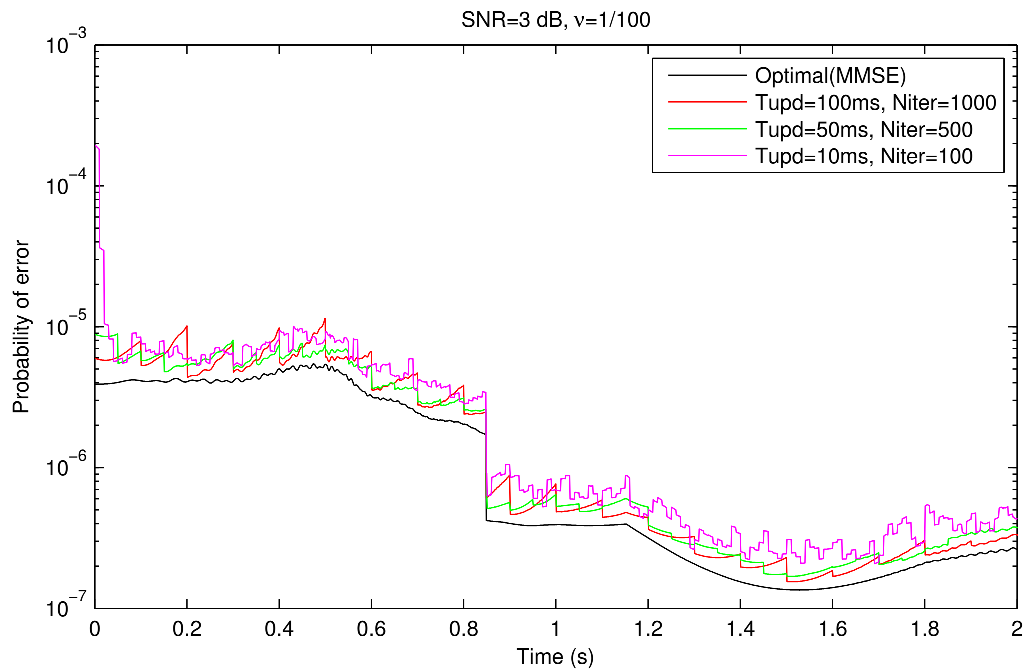

Figure 5.33: RLS performance in scenario I3 with fixed number of iterations/s

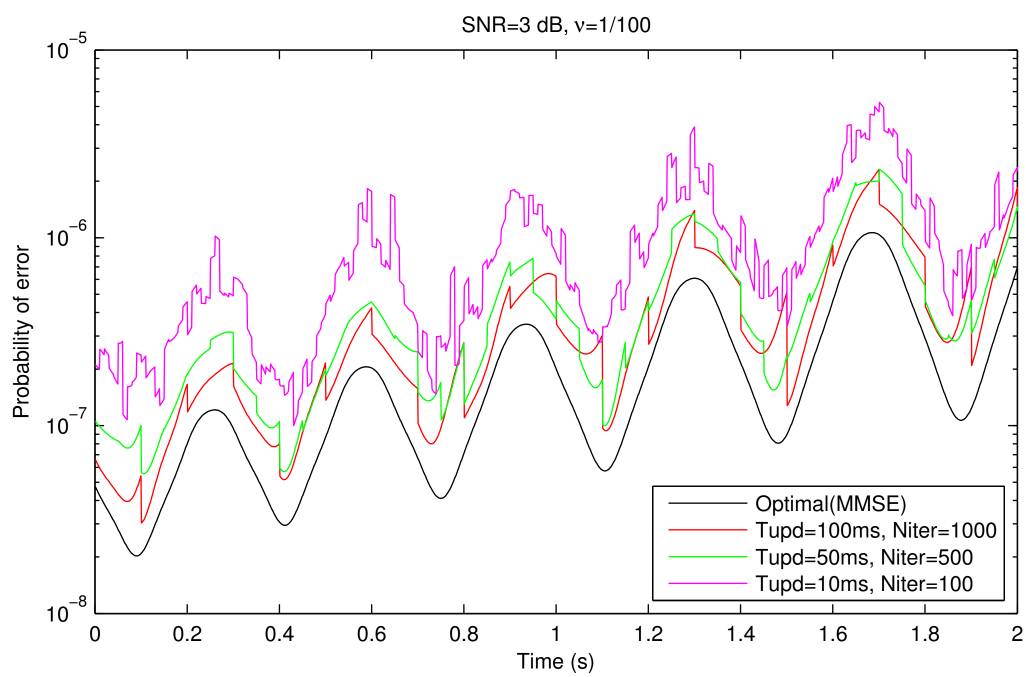

Figure 5.34: RLS performance in scenario O3 with fixed number of iterations/s

the current weight update, while the inverse correlation matrix $\mathbf{R}_{\mathbf{xx}}^{-1}$ is re-initialized each update. Because RLS is not being initialized with the previous inverse correlation matrix, reducing the number of iterations negatively affects performance even when the update period is decreased. Indoors, the trade-off is not pronounced because RLS converges quickly. However, in outdoor environments such as O3 in Fig. 5.34, P_b is higher with $\{T_{\text{upd}} = 10\text{ms}, N_{\text{iter}} = 100\}$ while P_b is similar between parameter sets $\{T_{\text{upd}} = 50\text{ms}, N_{\text{iter}} = 500\}$ and $\{T_{\text{upd}} = 100\text{ms}, N_{\text{iter}} = 1000\}$.

Since RLS iteratively estimates $\mathbf{R}_{\mathbf{xx}}^{-1}$, passing the previous weight vector and estimate of $\mathbf{R}_{\mathbf{xx}}^{-1}$ to the next update would allow RLS to build upon past iterations. It is expected that if each weight update was initialized with the previous estimate of $\mathbf{R}_{\mathbf{xx}}^{-1}$, fewer iterations of the RLS algorithm would be required, making the algorithm more efficient.

5.6 Conclusion

In this chapter, the theory behind the DMI, LMS, and RLS adaptive algorithms was presented. These algorithms are based on the MMSE optimality criterion which was selected in Chapter 4. The adaptive algorithms were evaluated (a) in stationary channels with continuous weight updates, (b) in time-varying channels with continuous weight updates, and (c) in time-varying channels with weight updates at regular intervals of time.

We found that initializing the weight vector as $\mathbf{w}(0) = \mathbf{0}$ and setting the step size parameter to $\mu = \frac{1}{25}\frac{2}{\text{trace}[\mathbf{x}(1)\mathbf{x}^H(1)]}$ provides a reliable and efficient implementation of the the LMS algorithm. This step size choice achieved a balance between convergence rate and steady state performance.

In the time-varying channels which have a coherence time of about 1 ms, the adaptive algorithms are capable of tracking the channel with continuous weight updates. Setting $\gamma = 0.995$ enables the RLS method to respond more quickly to changes in the channel while still maintaining steady state performance near that of the theoretical MMSE. Because the channel changes very slowly relative to the data rate of the system, a decision-directed approach in conjunction with the LMS algorithm was proposed. To ensure reliable transmission, an increase in the error rate of the system would trigger the transmission of a training packet.

In section 5.5 the link performance when the weights are regularly updated was analyzed. The results presented in this section provide direction in the design of array processors for the 60 GHz band. No noticeable degradation in performance was observed when T_{upd} is up to 10 times the channel coherence time. Also, for LMS, using the previous weight vector to initialize the current update reduces the number of iterations required to maintain performance near the theoretical MMSE weights. Indoors, RLS required very few iterations to maintain a P_b close to the theoretical MMSE. In outdoor environments, RLS should make use of the previous estimate of $\mathbf{R}_{\mathbf{xx}}^{-1}$ in order to efficiently track the channel.

Chapter 6

Conclusion

This thesis provided an analysis of array processing for communication systems operating in the 60 GHz band. Based on measurement campaigns at 60 GHz, deterministic modeling of the channel through ray tracing was proposed. We conducted a site-specific study using ray tracing to model an outdoor and indoor environment on the Virginia Tech campus. Because arrays are required for antenna gain and adaptability, we chose to explore the use of arrays as a form of equalization in the presence of channel-induced ISI. Throughout this work, a single carrier system with BPSK or QPSK modulation and a narrowband antenna array was utilized.

The first contribution of this thesis was to establish the expected performance achieved by arrays in the outdoor environment. The second contribution was to analyze the performance of adaptive algorithms applied to array processing in mobile indoor and outdoor environments.

In Chapter 3, an initial analysis of the performance of antenna arrays in the 60 GHz band was presented. The results demonstrate that beamsteering is not successful in mitigating ISI due to multipath. When the link budget is taken into account, reliable communication can only be achieved for ranges up to 10 m. At ranges of 25 and 50 m – typical ranges for outdoor environments – the link is severely interference limited.

At longer ranges, the ground bounce is a significant source of ISI. This is because as distance increases the magnitude and time delay approach that of the LOS path. In addition, the ground bounce enters the main beam of the array pattern. At ranges of 26 m and greater, the ground bounce always had a delay relative to the LOS of less than 1 ns. At a data rate of 1 Gbps, this delay is less than the symbol period. Thus, it is expected that equalization will also be unable to resolve the ground bounce as the range is increased above 26 m.

Even though a larger number of array elements increases the directivity of the array, we observe a minimal improvement in performance from the four by four array to the six by six array at ranges greater than or equal to 50 m. Thus, more powerful methods of array processing were explored.

In Chapter 4, four array processing methods, each built around an optimality criterion, were compared in terms of P_b. The Maximum SINR and MMSE methods both have improved performance over beamsteering. The MMSE criterion outperforms the other methods by constructively summing correlated multipath components.

Also in Chapter 4, we evaluated a practical beam codebook approach to array processing which is being adopted by IEEE 802.15.3c. The beam codebook method achieves a performance very near to that of the beamsteering method. Since the beam codebook effectively steers a beam to one of several predefined discrete directions, it is expected that the performance would be similar. Thus, the beam codebook, like beamsteering, does not sufficiently mitigate ISI and would need to be used along with another method for handling the frequency selective channel such as equalization or OFDM.

The link budget of Section 3.3 is not sufficient to enable effective communication at a range of 100 m. The additional power which is required can be obtained through larger arrays or increased transmit power. With the MMSE method, the performance of the link is not interference limited which means that increased transmit power reduces P_b. Additionally, when used with MMSE array processing, larger arrays achieve significant performance improvements as demonstrated by the comparison of the four by four and six by six planar arrays in Section 4.3.3. Specifically, increased resolution in the vertical dimension improves performance at longer ranges as demonstrated by the nine by four array. The nine by four array was used for the evaluation of array processing in the outdoor time-varying channel.

In Chapter 5, the theory behind the DMI, LMS, and RLS adaptive algorithms was presented. These algorithms are based on the MMSE optimality criterion which was selected in Chapter 4. The adaptive algorithms were evaluated (a) in stationary channels with continuous weight updates, (b) in time-varying channels with continuous weight updates, and (c) in time-varying channels with weight updates at regular intervals of time.

We found that initializing the weight vector as $\mathbf{w}(0) = \mathbf{0}$ and setting the step size parameter to $\mu = \frac{1}{25}\frac{2}{\mathrm{trace}[\mathbf{x}(1)\mathbf{x}^H(1)]}$ provides a reliable and efficient implementation of the the LMS algorithm. This step size choice achieved a balance between convergence rate and steady state performance.

In the time-varying channels which have a coherence time of about 1 ms, the adaptive algorithms are capable of tracking the channel with continuous weight updates. Setting $\gamma = 0.995$ enables the RLS method to respond more quickly to changes in the channel while still maintaining steady state performance near that of the theoretical MMSE. Because the channel changes very slowly relative to the data rate of the system, a decision-directed approach in conjunction with the LMS algorithm is proposed. To ensure reliable transmission, an increase in the error rate of the system would trigger the transmission of a training packet.

In Section 5.5, the link performance when the weights are regularly updated was analyzed. The results presented in this section provide direction in the design of array processors for the 60 GHz band. No noticeable degradation in performance was observed when T_{upd} was as much as 10 times the channel coherence time. Also, for LMS, using the previous weight vector to initialize the current update reduces the number of iterations required to maintain performance near the theoretical MMSE weights. Indoors, RLS required very few iterations to maintain a P_b close to the theoretical MMSE. Finally, in outdoor environments, RLS should make use of the previous estimate of $\mathbf{R}_{\mathbf{xx}}^{-1}$ in order to efficiently track the channel.

Appendix A

Complete Results for the Effect of Initial Weights on Convergence

This appendix includes the complete set of results for the simulation of the LMS and RLS algorithm's convergence with three initial weight vectors. In Figs. A.1 through A.15 the convergence results of the LMS algorithm and in Figs. A.16 through A.30 the convergence results of the RLS algorithm for each scenario in the indoor and outdoor environments are presented. A diagram of the indoor scenarios is available in Fig. 5.2 and a diagram of the outdoor scenarios is available in Fig. 5.3. The simulation is intended to provide insight into the effect of the initial weight vector on the convergence of the algorithm. Refer to Section 5.3.1 for an analysis of the results.

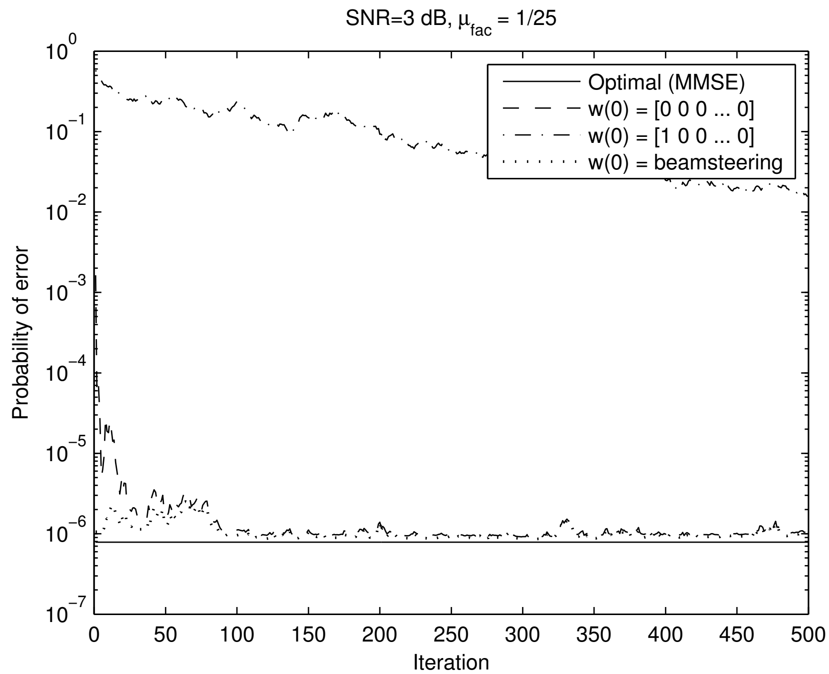

Figure A.1: Effect of $\mathbf{w}(0)$ on the convergence of LMS for scenario I1

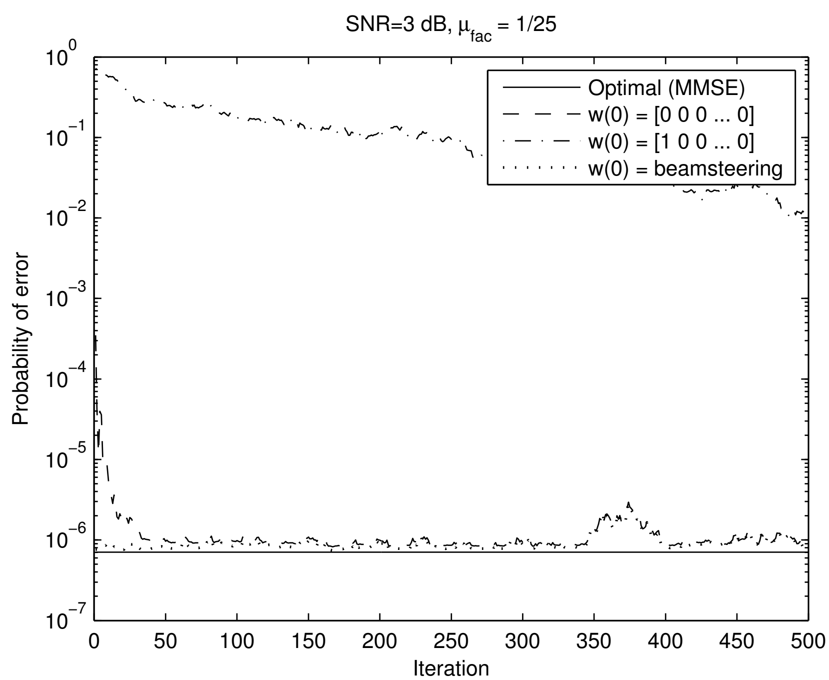

Figure A.2: Effect of $\mathbf{w}(0)$ on the convergence of LMS for scenario I2

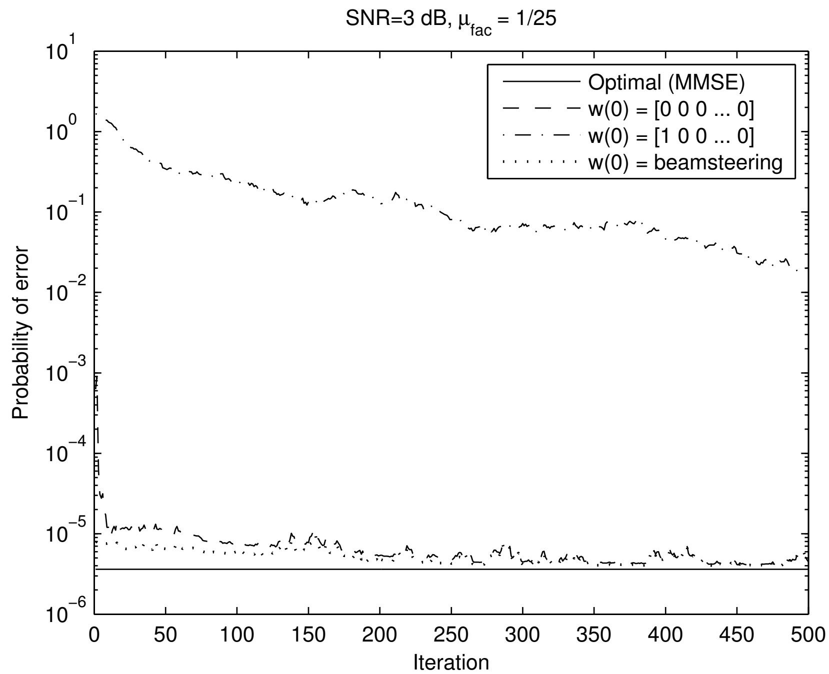

Figure A.3: Effect of $\mathbf{w}(0)$ on the convergence of LMS for scenario I3

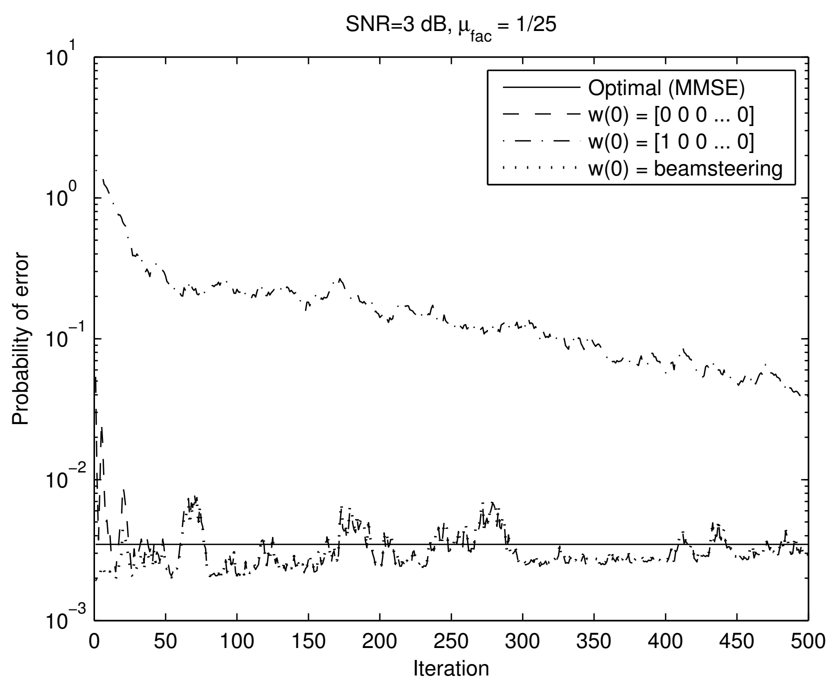

Figure A.4: Effect of $\mathbf{w}(0)$ on the convergence of LMS for scenario I4

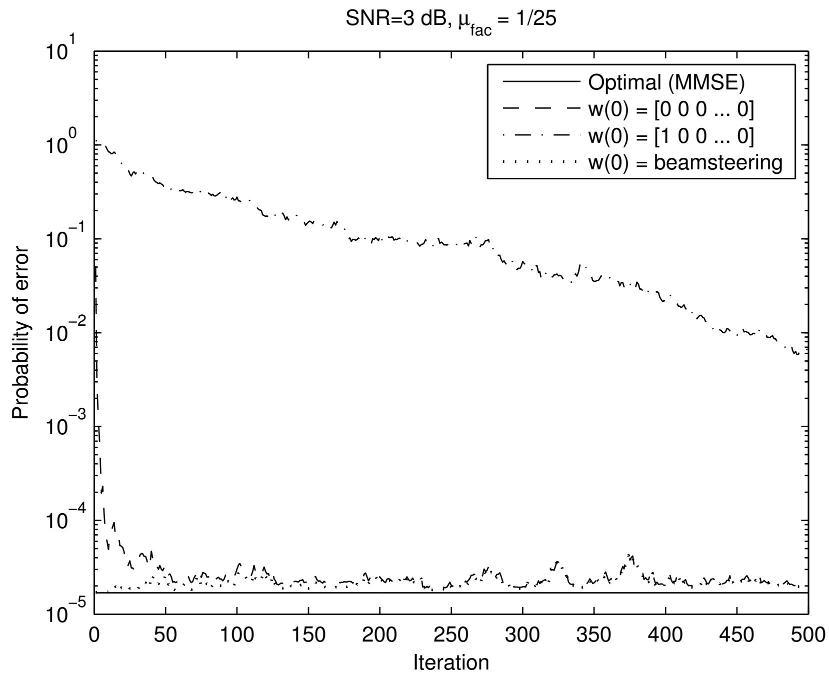

Figure A.5: Effect of $\mathbf{w}(0)$ on the convergence of LMS for scenario I5

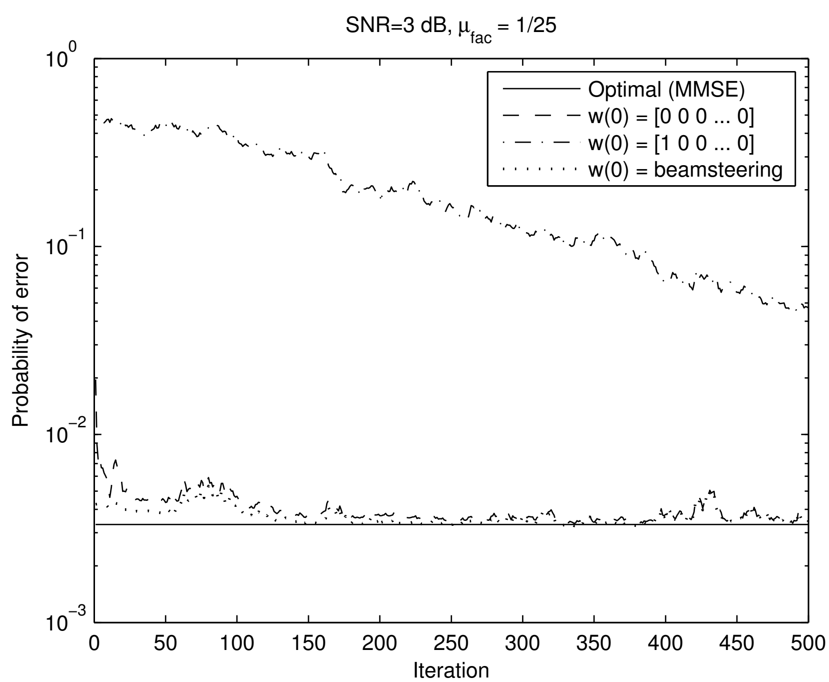

Figure A.6: Effect of $\mathbf{w}(0)$ on the convergence of LMS for scenario I6

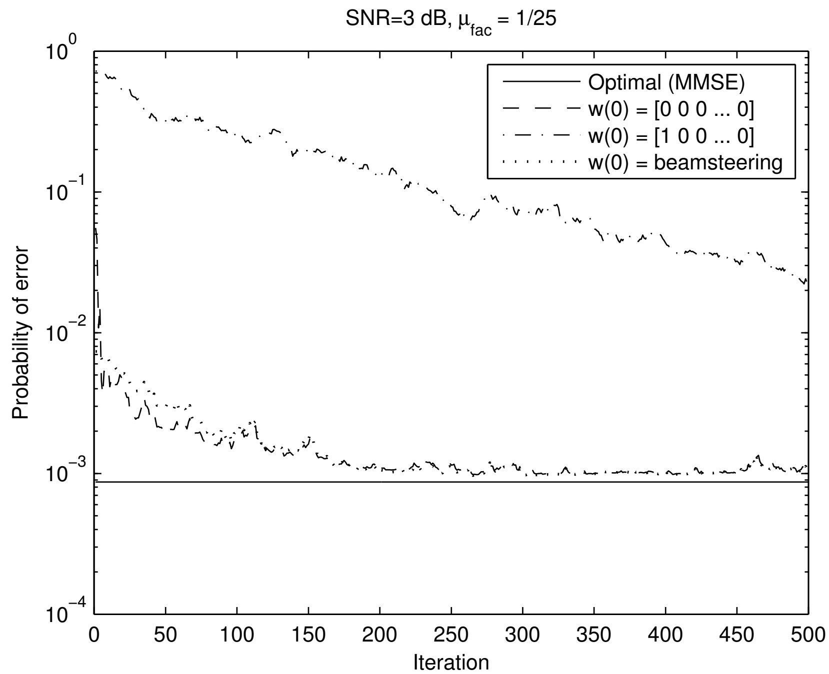

Figure A.7: Effect of $\mathbf{w}(0)$ on the convergence of LMS for scenario I7

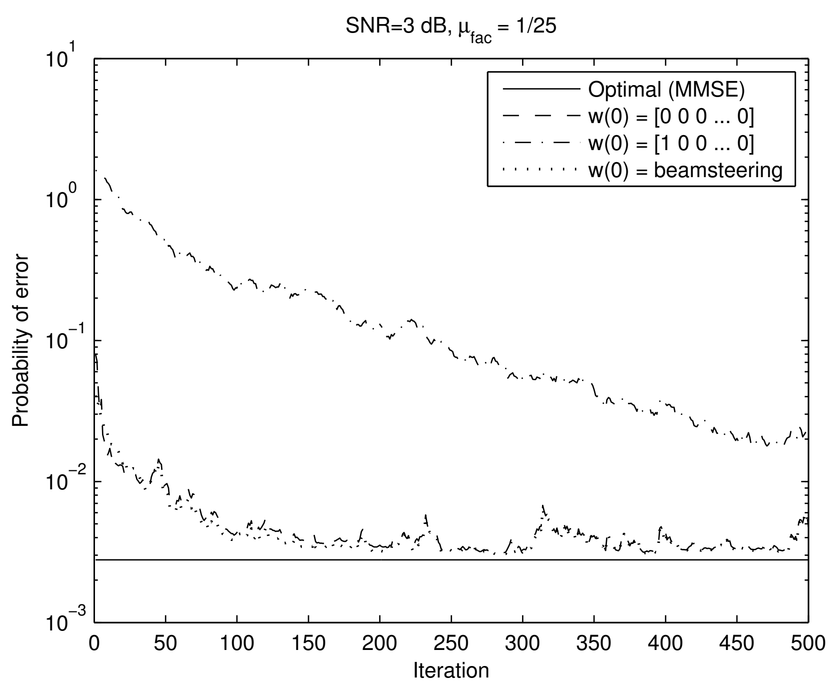

Figure A.8: Effect of $\mathbf{w}(0)$ on the convergence of LMS for scenario I8

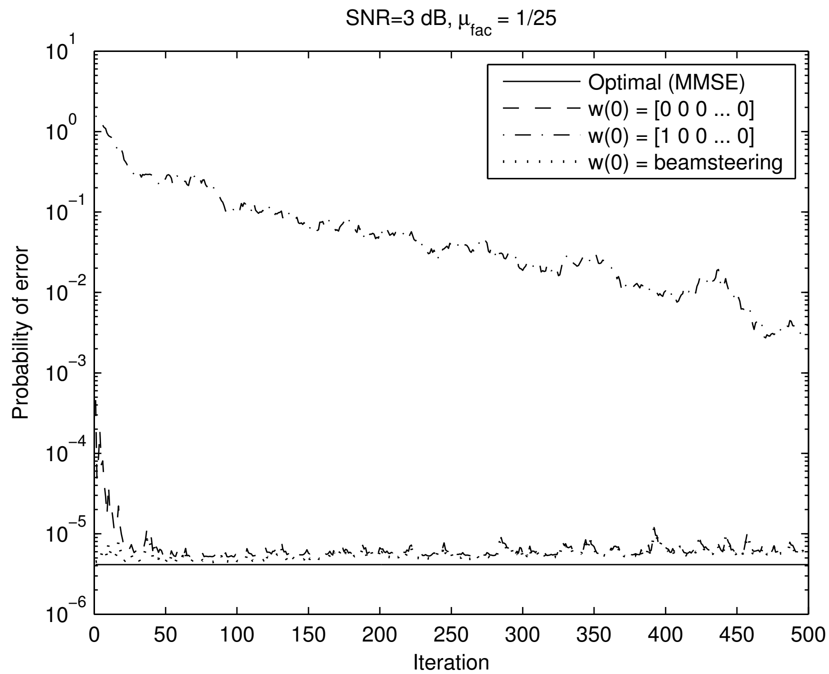

Figure A.9: Effect of $\mathbf{w}(0)$ on the convergence of LMS for scenario I9

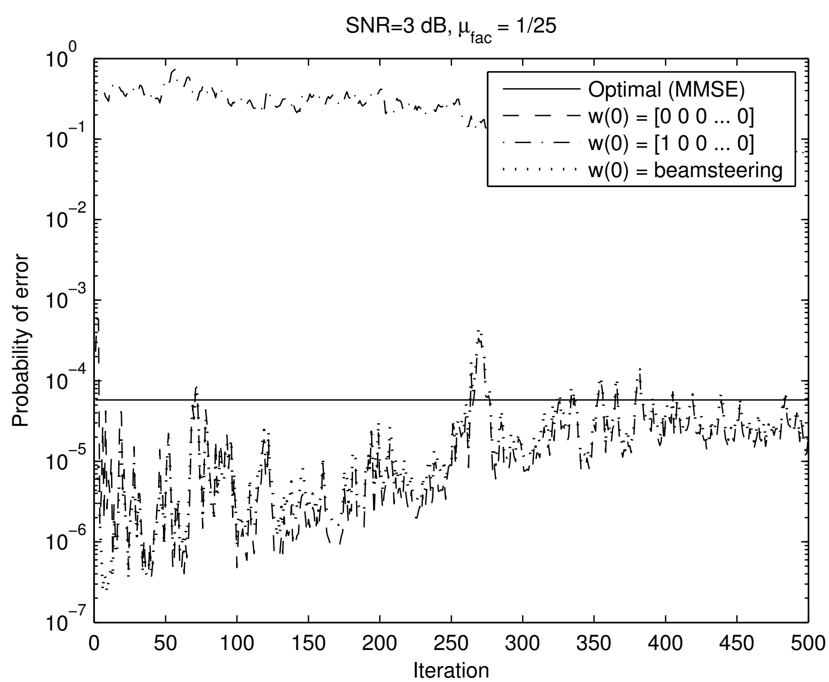

Figure A.10: Effect of $\mathbf{w}(0)$ on the convergence of LMS for scenario O1

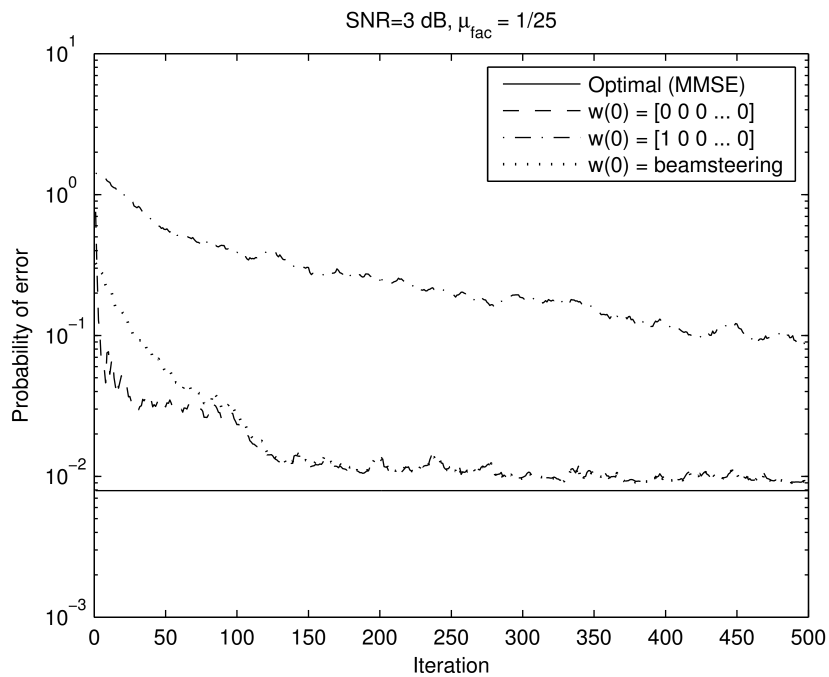

Figure A.11: Effect of $\mathbf{w}(0)$ on the convergence of LMS for scenario O2

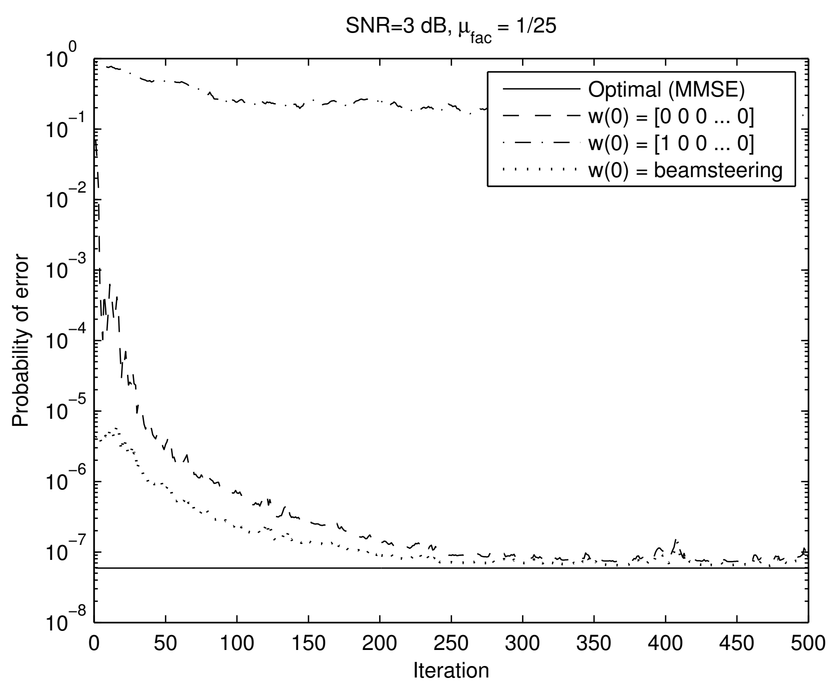

Figure A.12: Effect of $\mathbf{w}(0)$ on the convergence of LMS for scenario O3

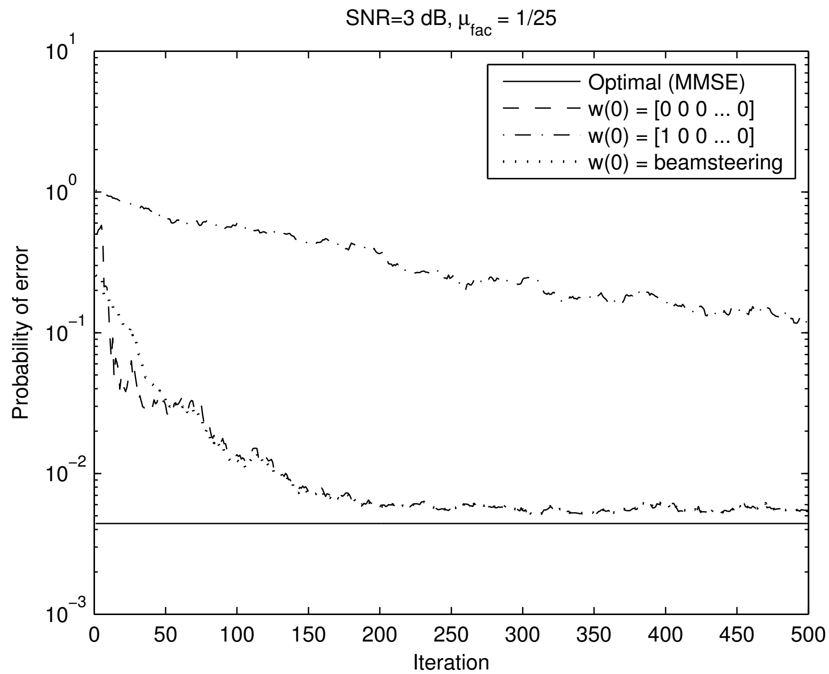

Figure A.13: Effect of $\mathbf{w}(0)$ on the convergence of LMS for scenario O4

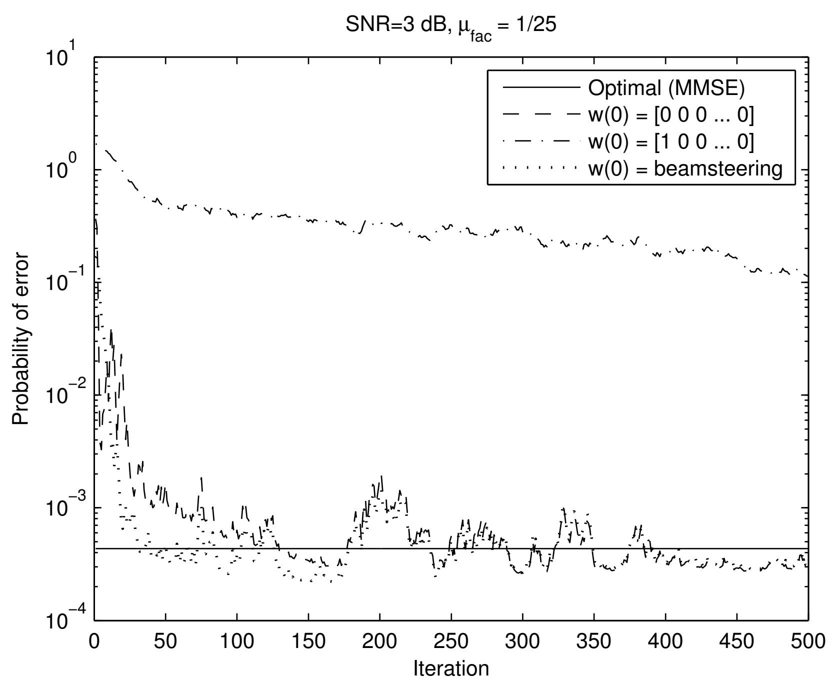

Figure A.14: Effect of $\mathbf{w}(0)$ on the convergence of LMS for scenario O5

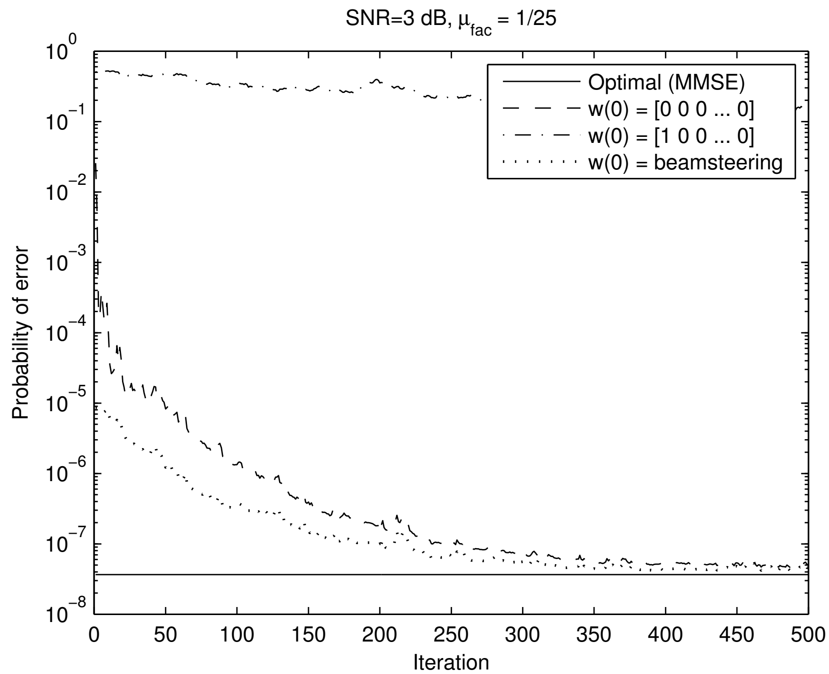

Figure A.15: Effect of $\mathbf{w}(0)$ on the convergence of LMS for scenario O6

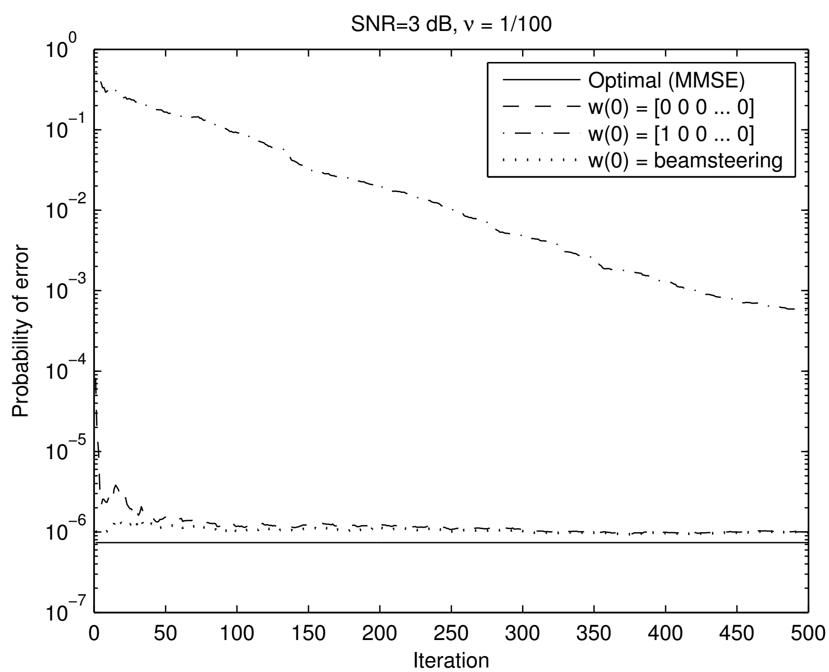

Figure A.16: Effect of $\mathbf{w}(0)$ on the convergence of RLS for scenario I1

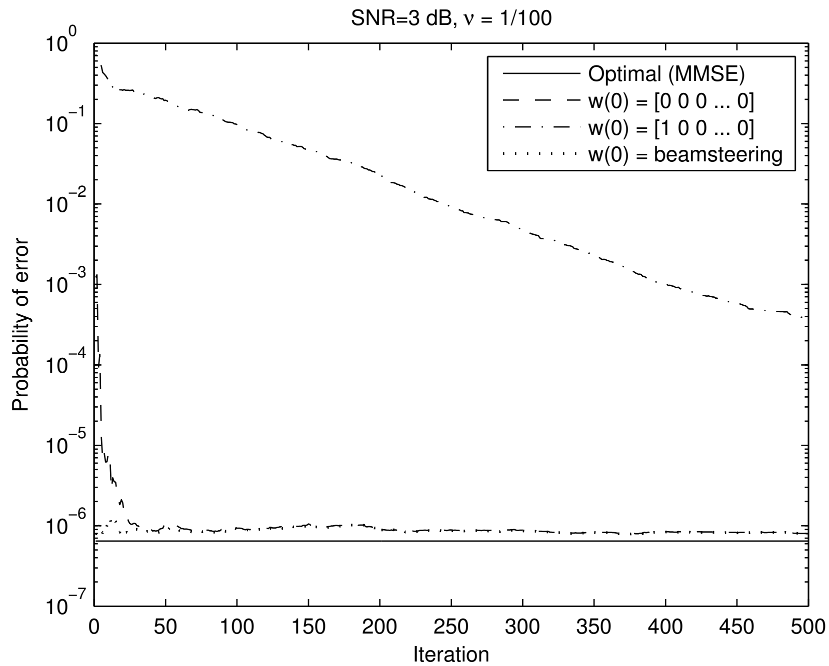

Figure A.17: Effect of $\mathbf{w}(0)$ on the convergence of RLS for scenario I2

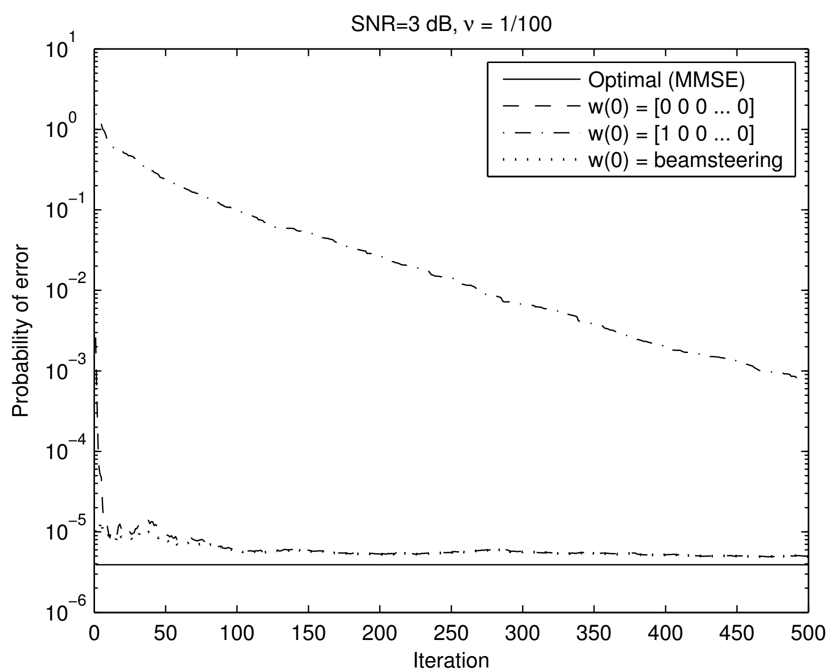

Figure A.18: Effect of $\mathbf{w}(0)$ on the convergence of RLS for scenario I3

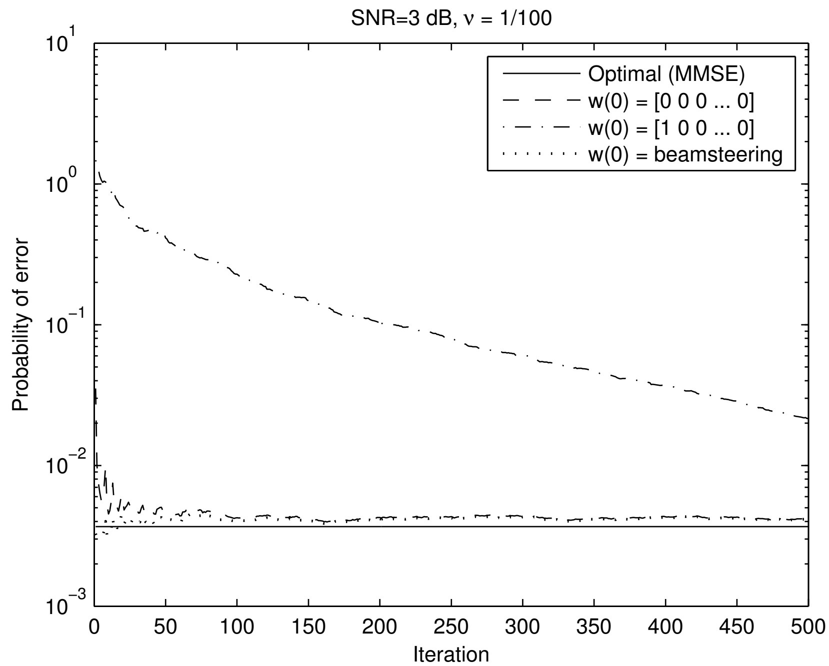

Figure A.19: Effect of $\mathbf{w}(0)$ on the convergence of RLS for scenario I4

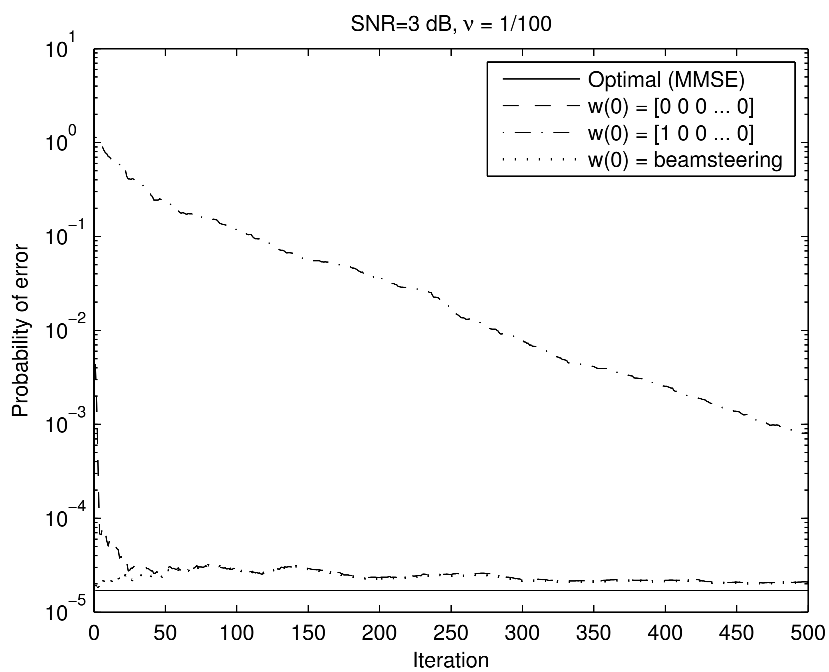

Figure A.20: Effect of $\mathbf{w}(0)$ on the convergence of RLS for scenario I5

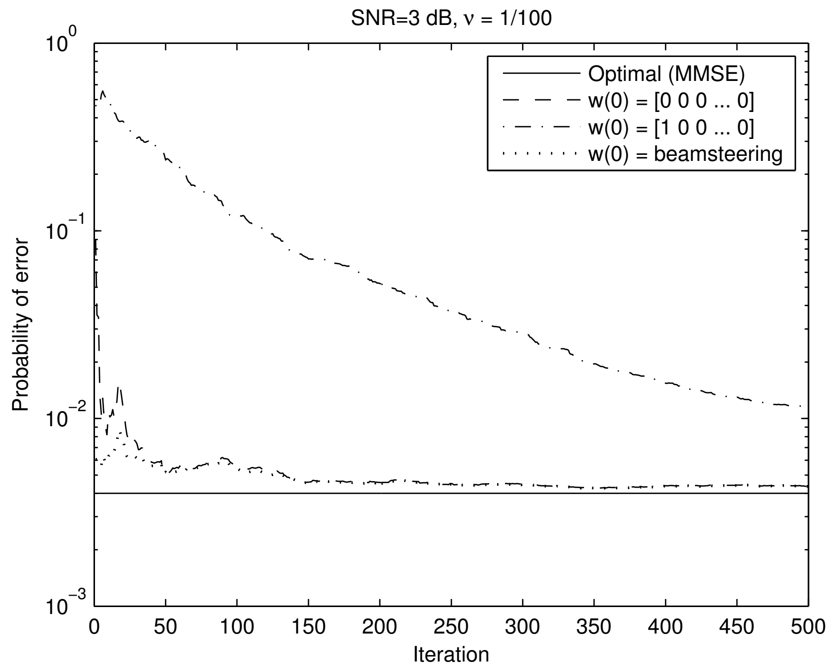

Figure A.21: Effect of $\mathbf{w}(0)$ on the convergence of RLS for scenario I6

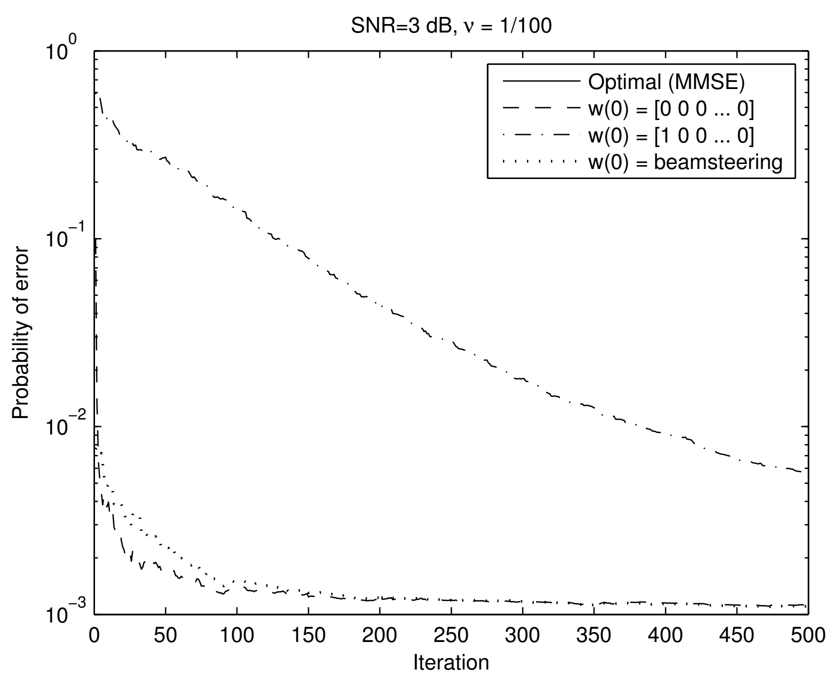

Figure A.22: Effect of $\mathbf{w}(0)$ on the convergence of RLS for scenario I7

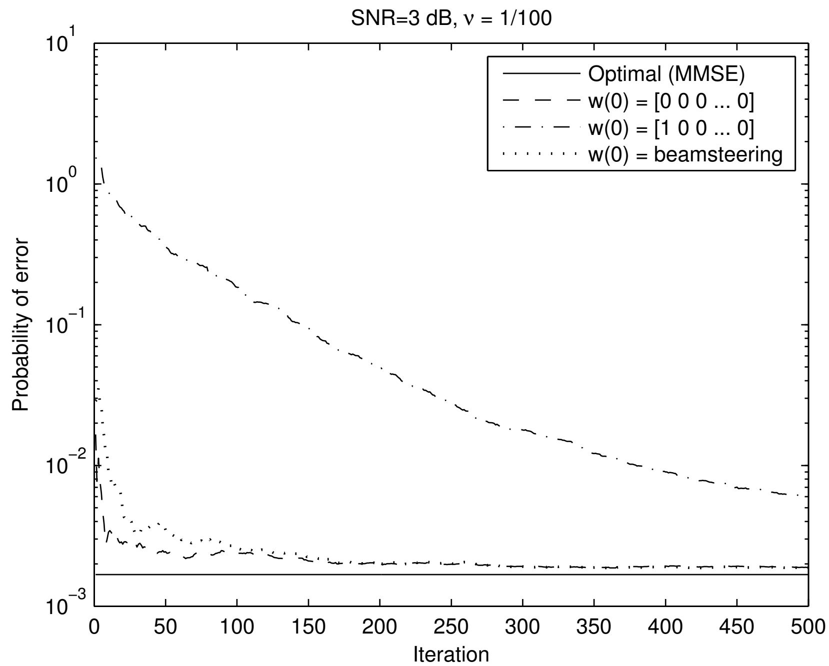

Figure A.23: Effect of $\mathbf{w}(0)$ on the convergence of RLS for scenario I8

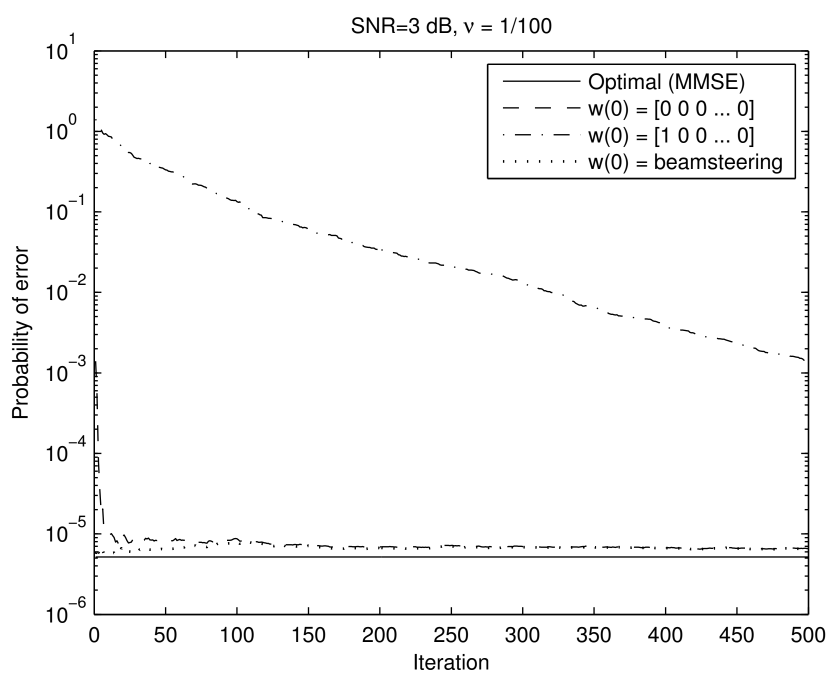

Figure A.24: Effect of $\mathbf{w}(0)$ on the convergence of RLS for scenario I9

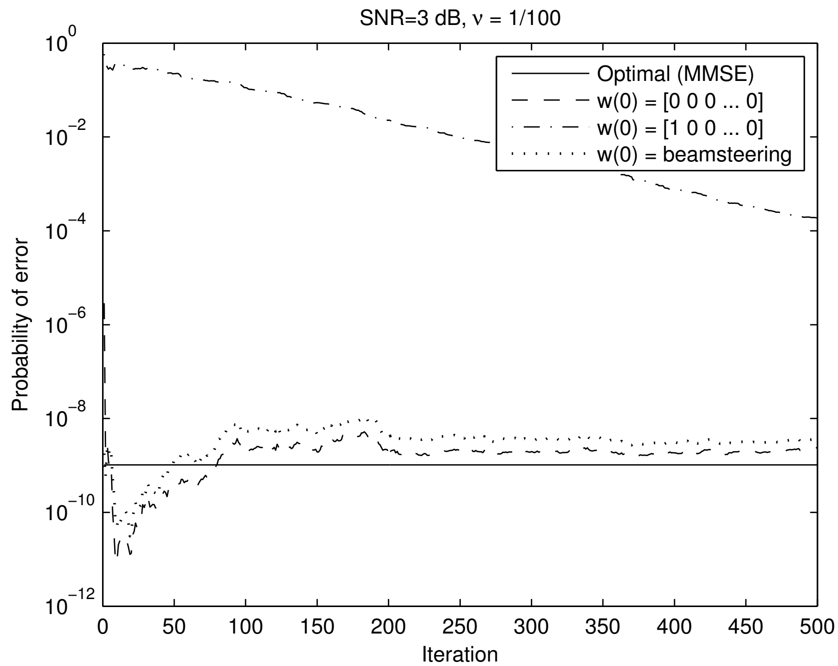

Figure A.25: Effect of $\mathbf{w}(0)$ on the convergence of RLS for scenario O1

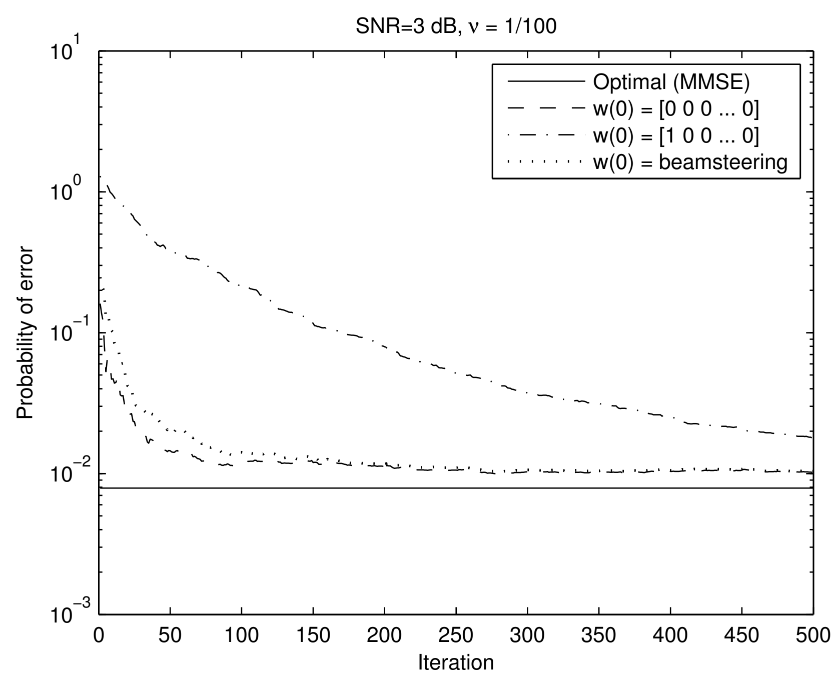

Figure A.26: Effect of $\mathbf{w}(0)$ on the convergence of RLS for scenario O2

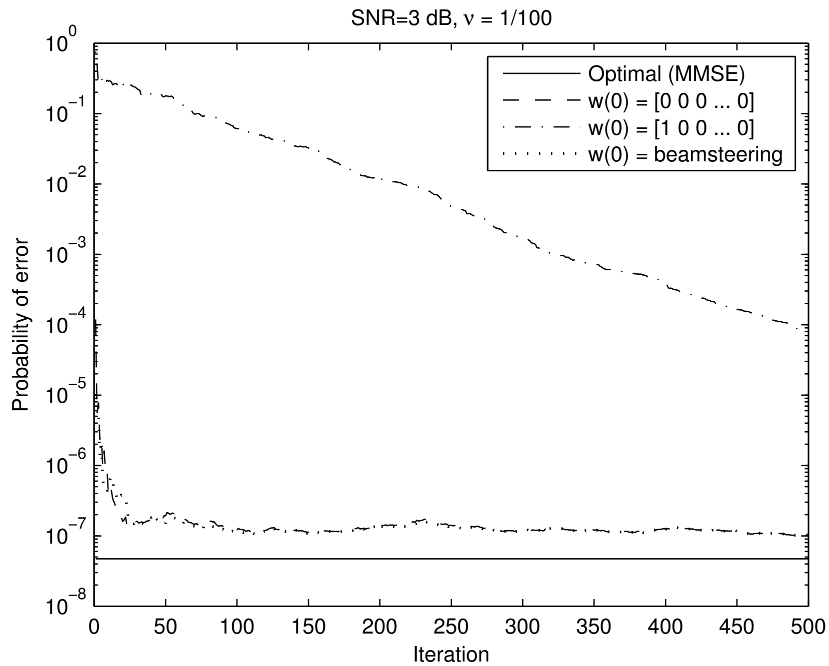

Figure A.27: Effect of $\mathbf{w}(0)$ on the convergence of RLS for scenario O3

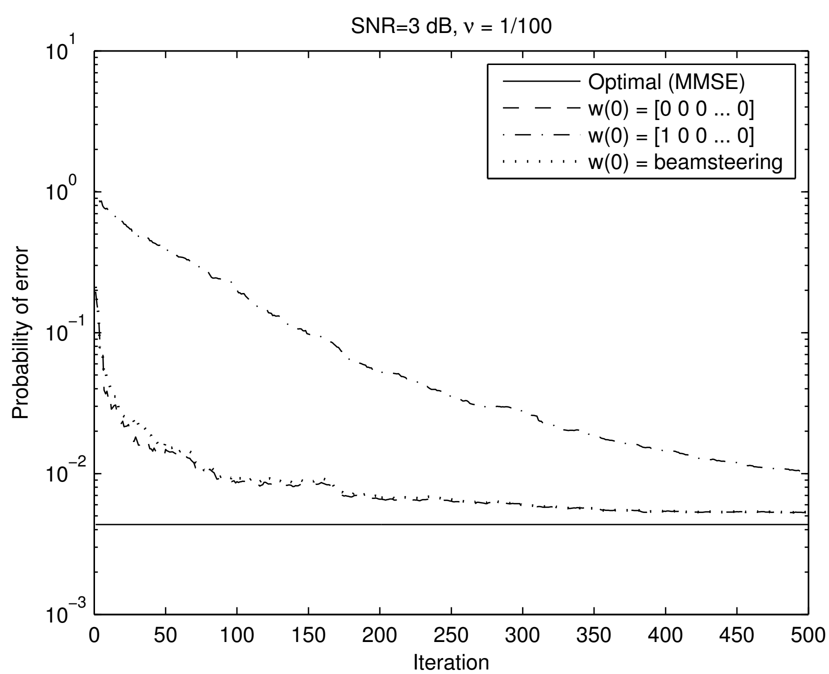

Figure A.28: Effect of $\mathbf{w}(0)$ on the convergence of RLS for scenario O4

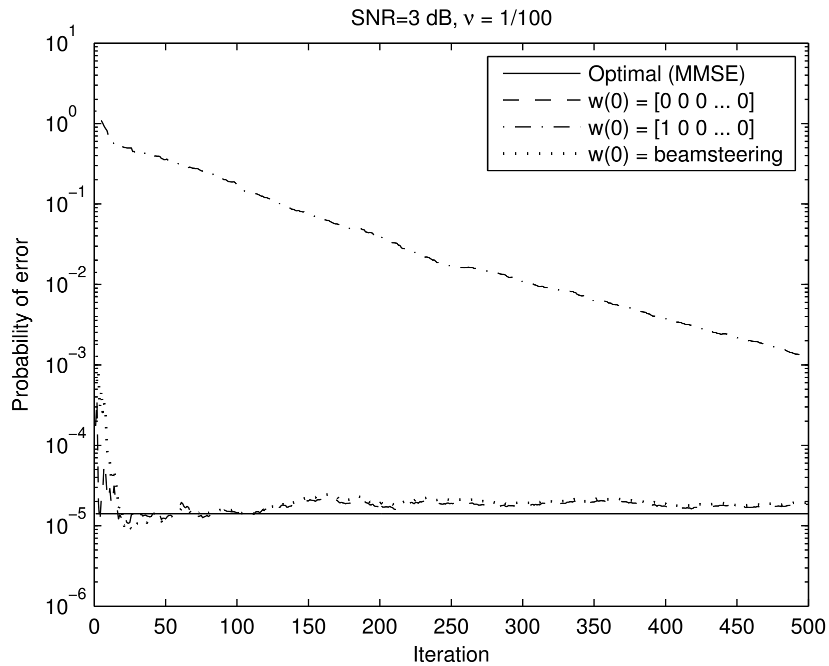

Figure A.29: Effect of $\mathbf{w}(0)$ on the convergence of RLS for scenario O5

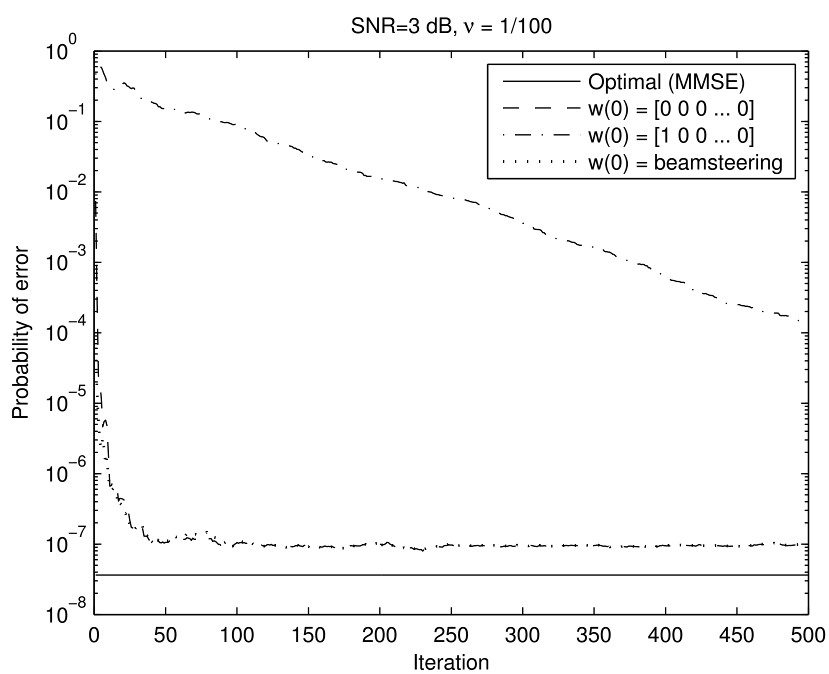

Figure A.30: Effect of $\mathbf{w}(0)$ on the convergence of RLS for scenario O6

Appendix B

Complete Results for the Effect of Step Size on the Convergence of the LMS Algorithm

This appendix includes the complete set of results for the simulation of the LMS algorithm's convergence with four step sizes. Figs. B.1 through B.15 present the results for each scenario in the indoor and outdoor environments. A diagram of the indoor scenarios is available in Fig. 5.2 and a diagram of the outdoor scenarios is available in Fig. 5.3. The simulation is intended to provide insight into the effect of the step size on the convergence of the algorithm. Refer to Section 5.3.2 for an analysis of the results.

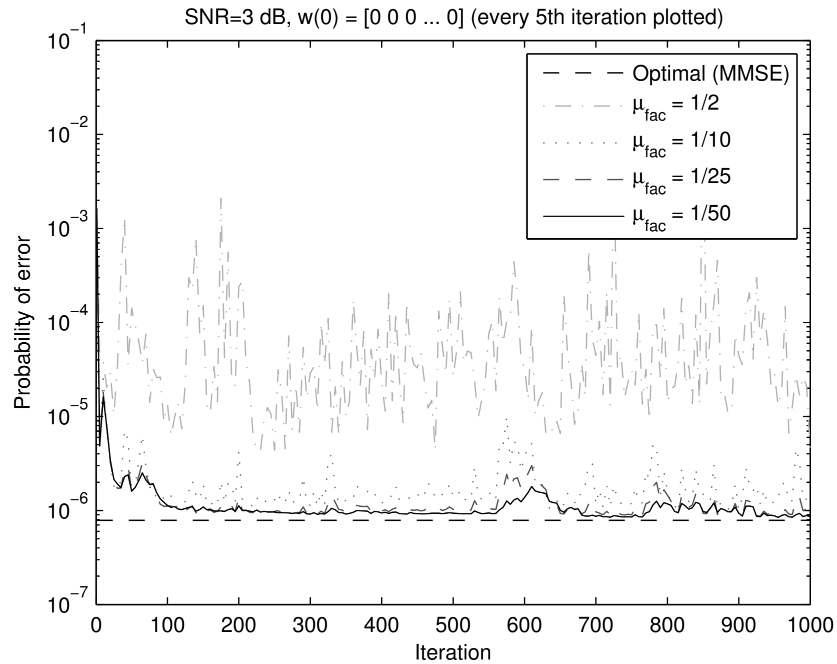

Figure B.1: Effect of μ on the convergence of LMS for scenario I1

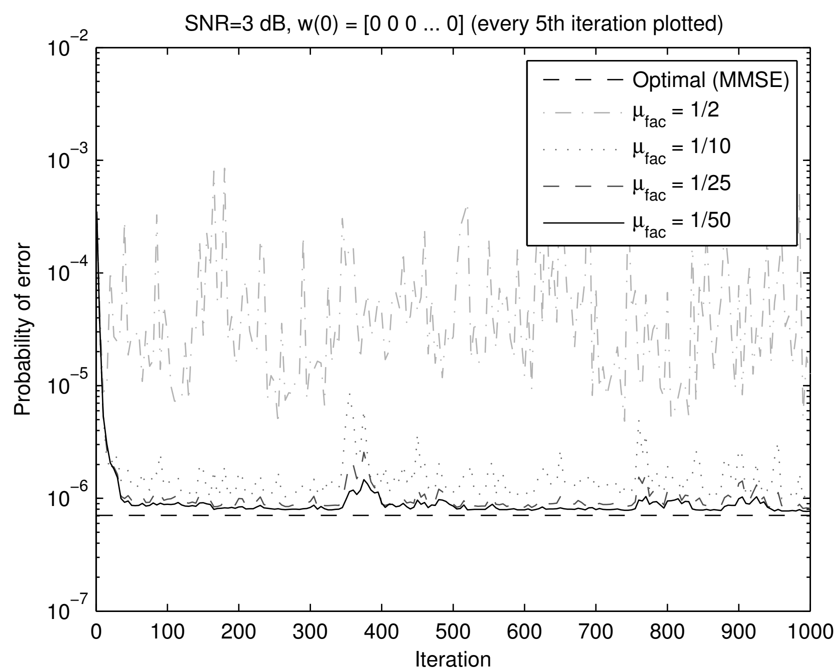

Figure B.2: Effect of μ on the convergence of LMS for scenario I2

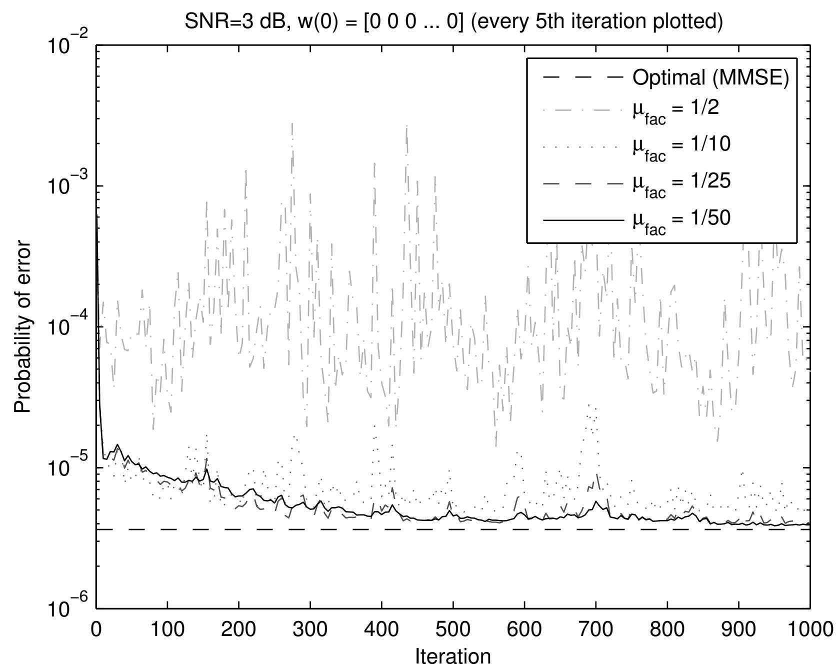

Figure B.3: Effect of μ on the convergence of LMS for scenario I3

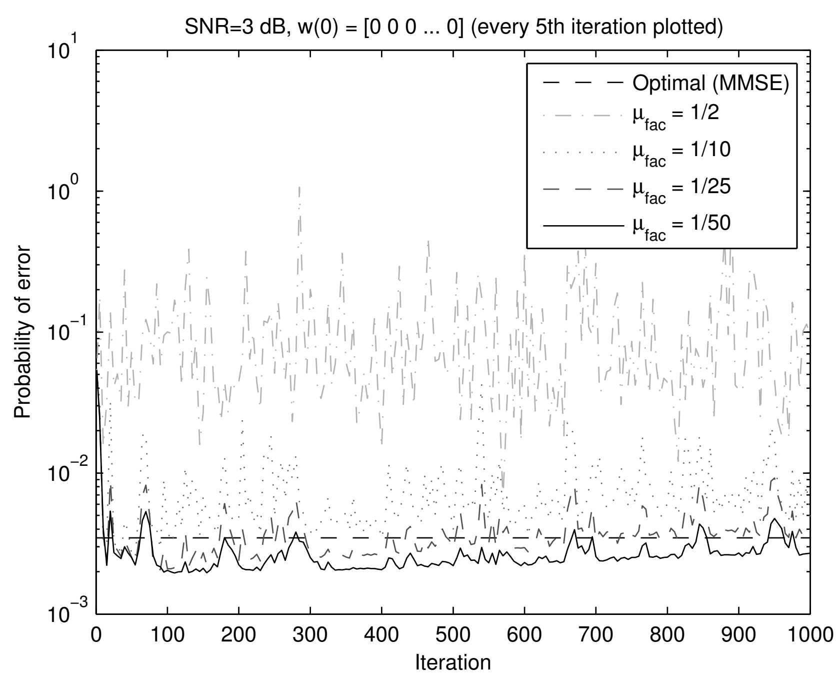

Figure B.4: Effect of μ on the convergence of LMS for scenario I4

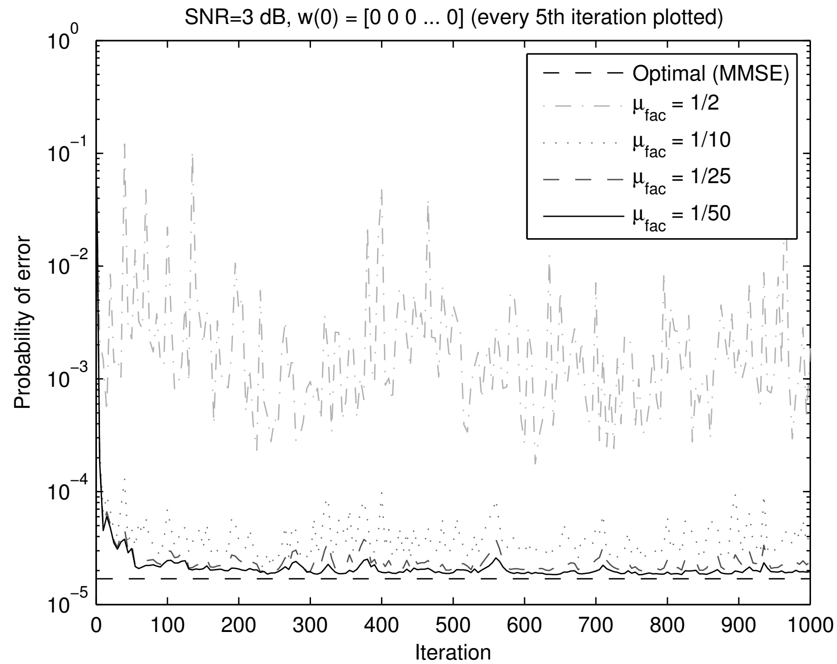

Figure B.5: Effect of μ on the convergence of LMS for scenario I5

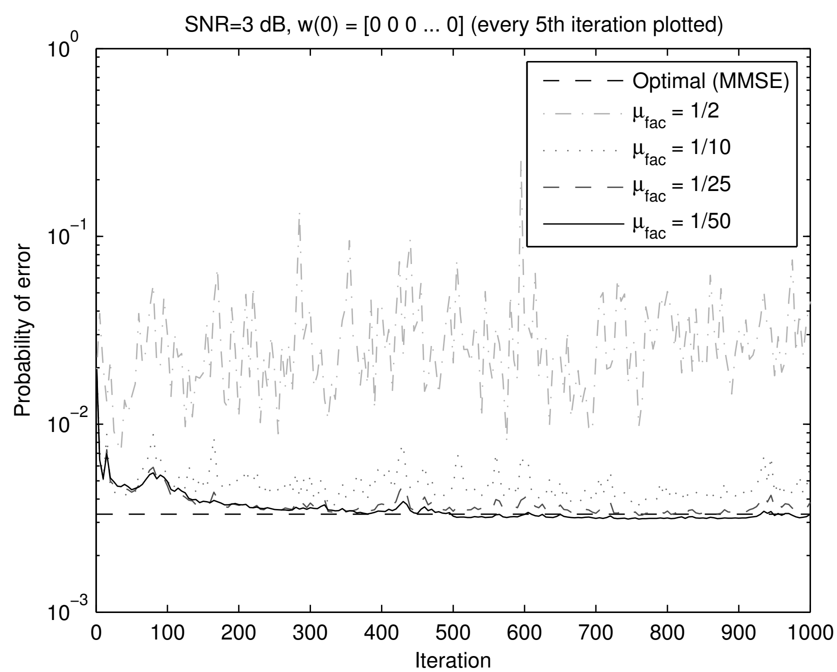

Figure B.6: Effect of μ on the convergence of LMS for scenario I6

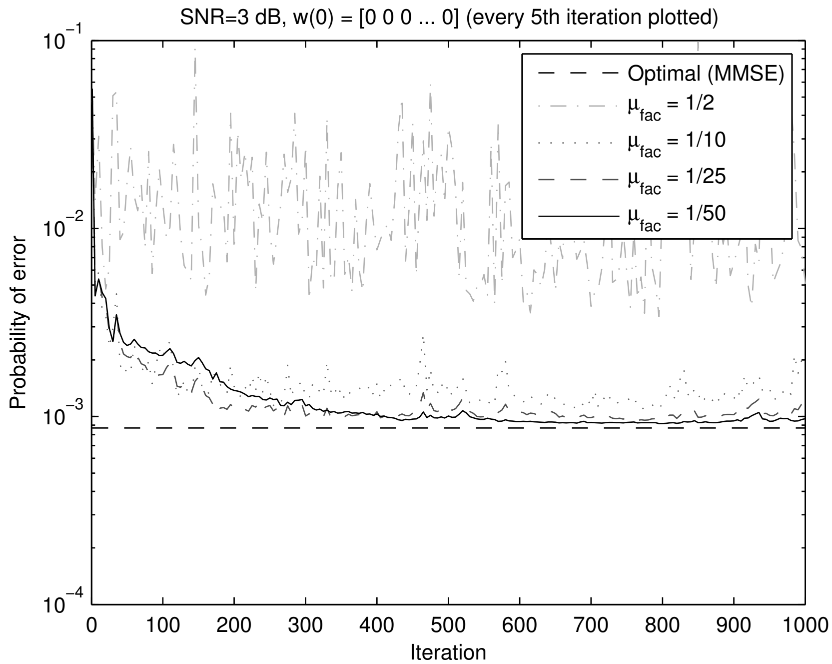

Figure B.7: Effect of μ on the convergence of LMS for scenario I7

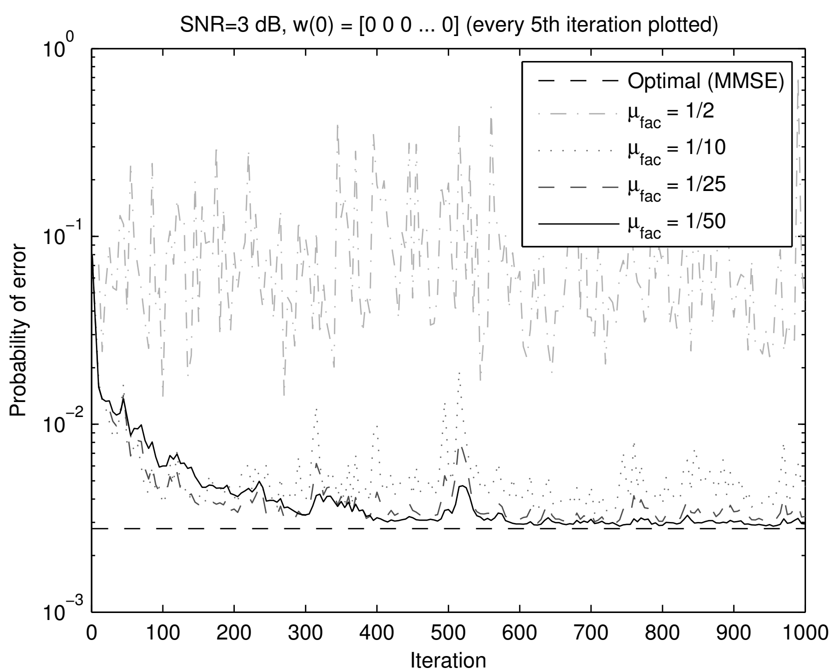

Figure B.8: Effect of μ on the convergence of LMS for scenario I8

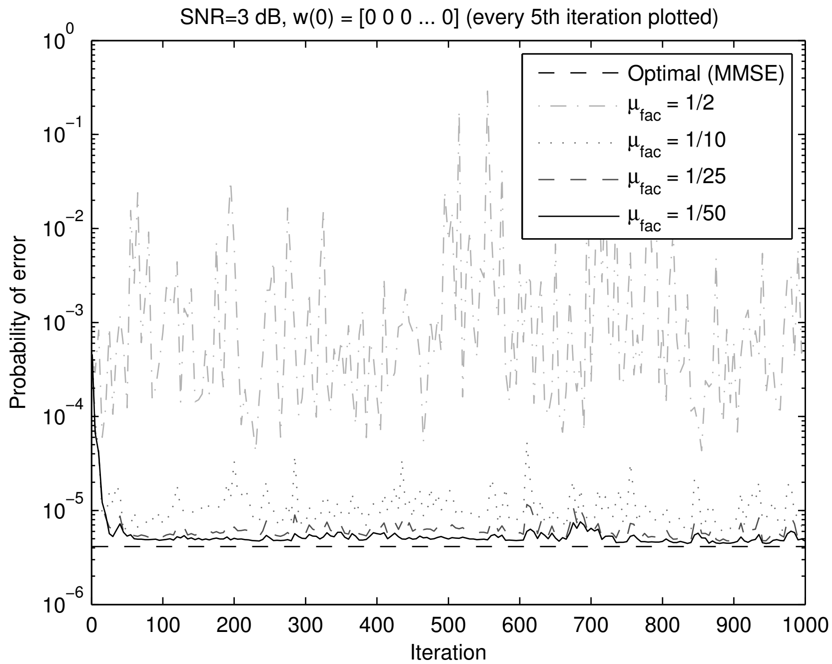

Figure B.9: Effect of μ on the convergence of LMS for scenario I9

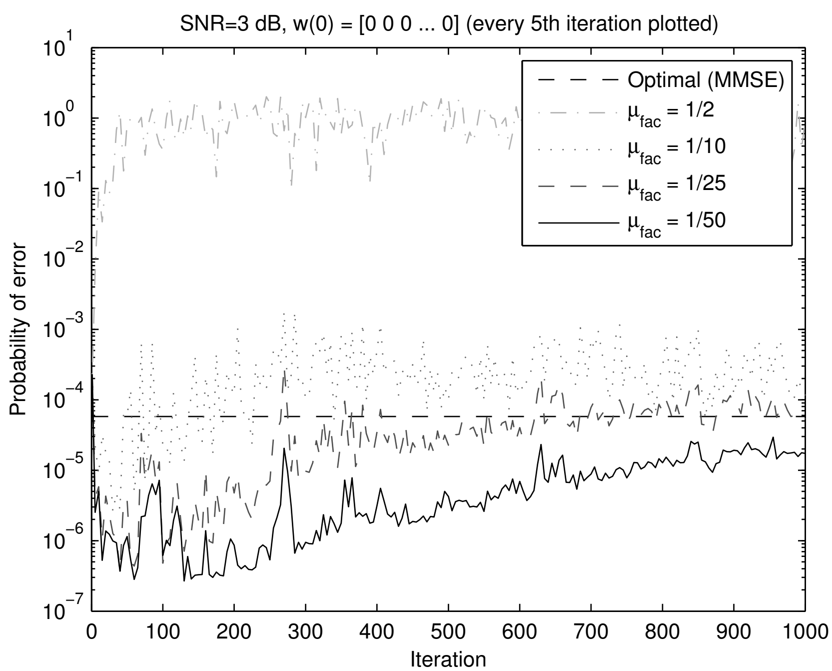

Figure B.10: Effect of μ on the convergence of LMS for scenario O1

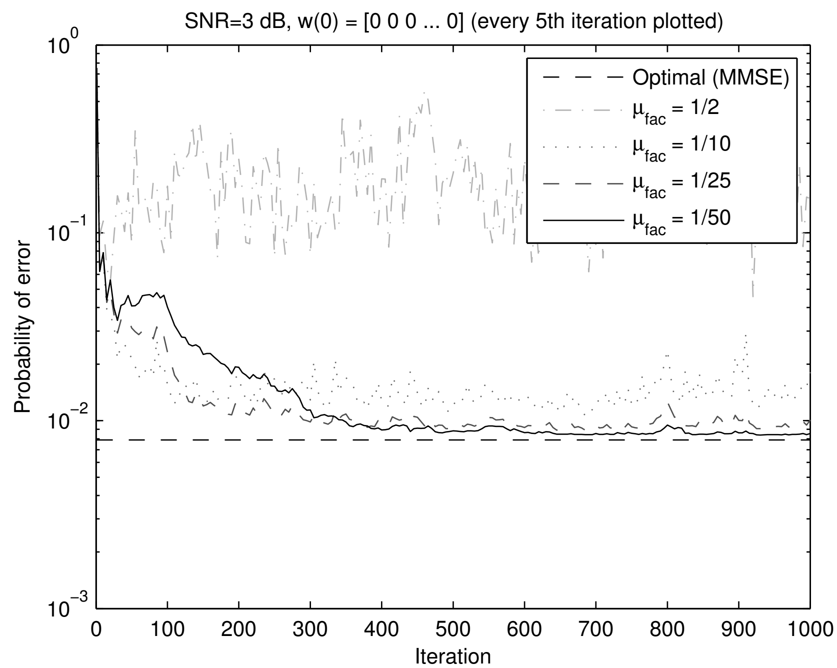

Figure B.11: Effect of μ on the convergence of LMS for scenario O2

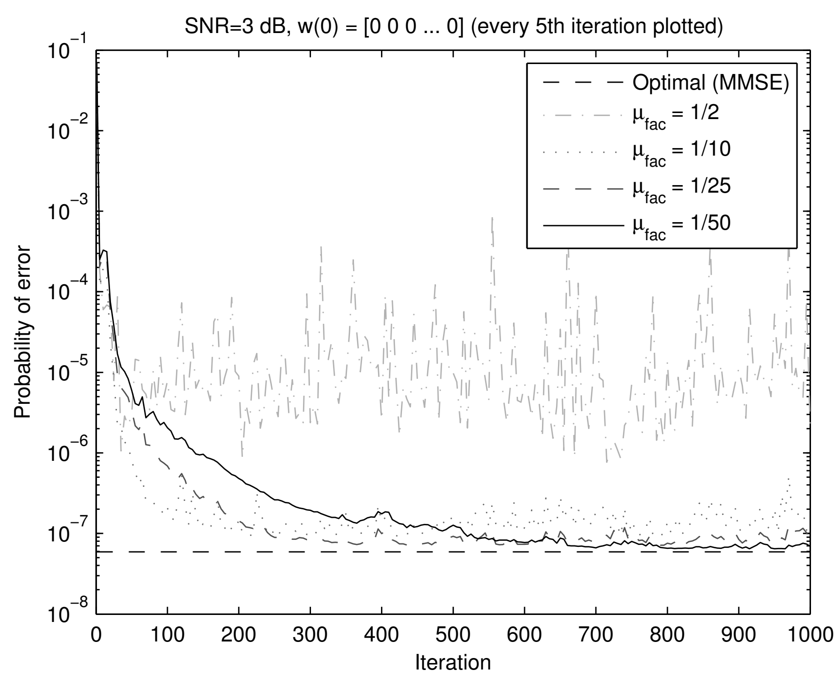

Figure B.12: Effect of μ on the convergence of LMS for scenario O3

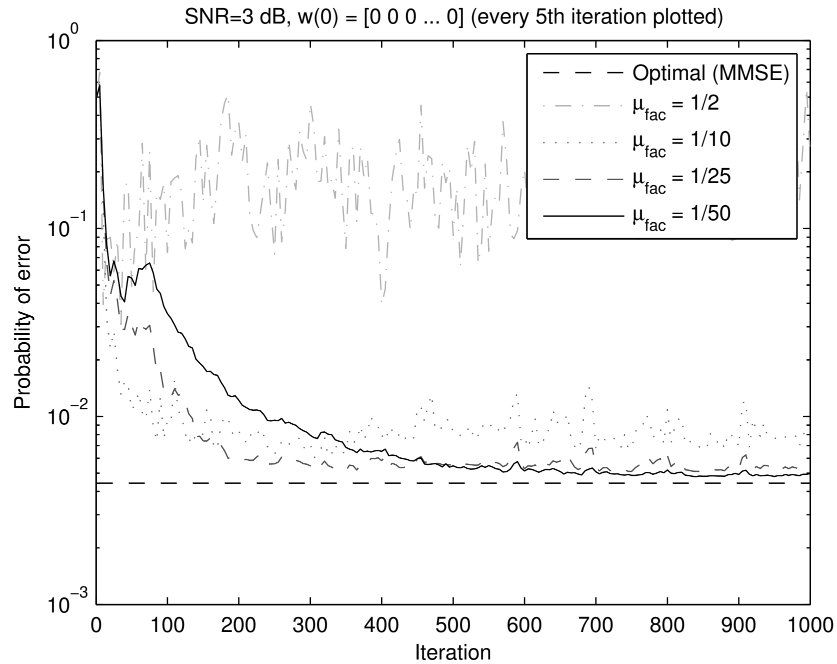

Figure B.13: Effect of μ on the convergence of LMS for scenario O4

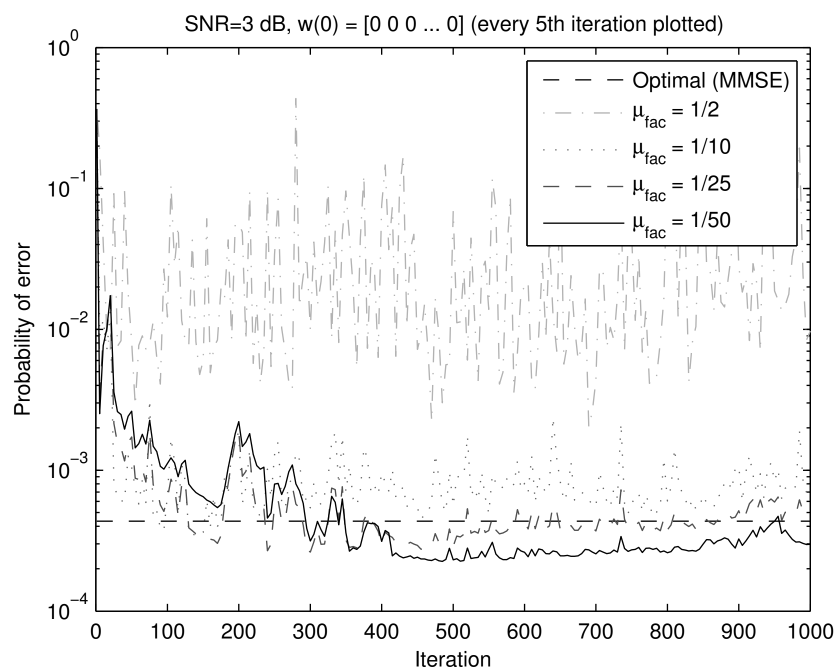

Figure B.14: Effect of μ on the convergence of LMS for scenario O5

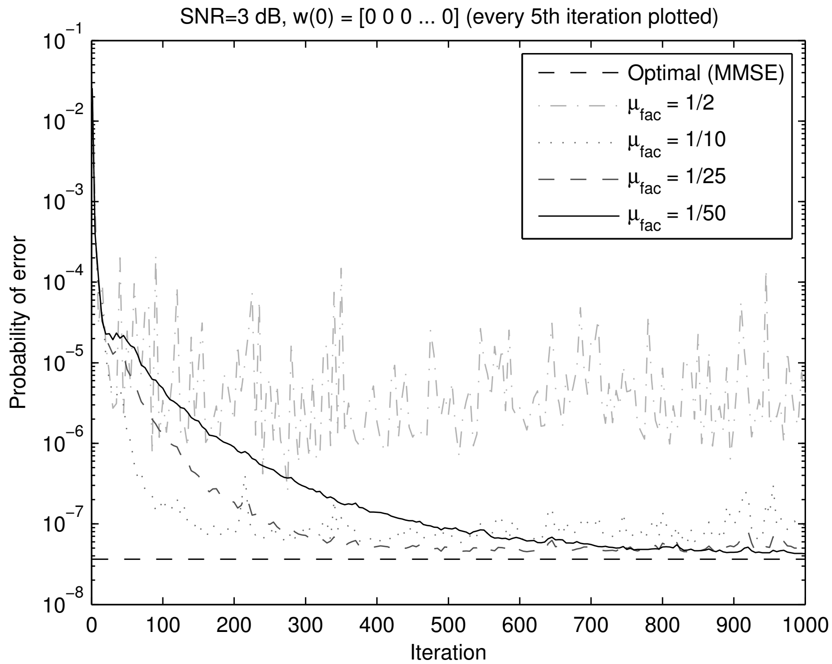

Figure B.15: Effect of μ on the convergence of LMS for scenario O6

Appendix C

Complete Results for the Comparison of DMI, LMS, and RLS

This appendix includes the complete set of results for the simulation comparing each adaptive method. Figs. C.1 through C.15 present the results for each scenario in the indoor and outdoor environments. A diagram of the indoor scenarios is available in Fig. 5.2 and a diagram of the outdoor scenarios is available in Fig. 5.3. DMI, LMS, and RLS are compared in terms of MSE and P_b. In addition to demonstrating their relative performances, the results provide insight into the relationship between MSE and P_b. Refer to Section 5.3.3 for an analysis of the results.

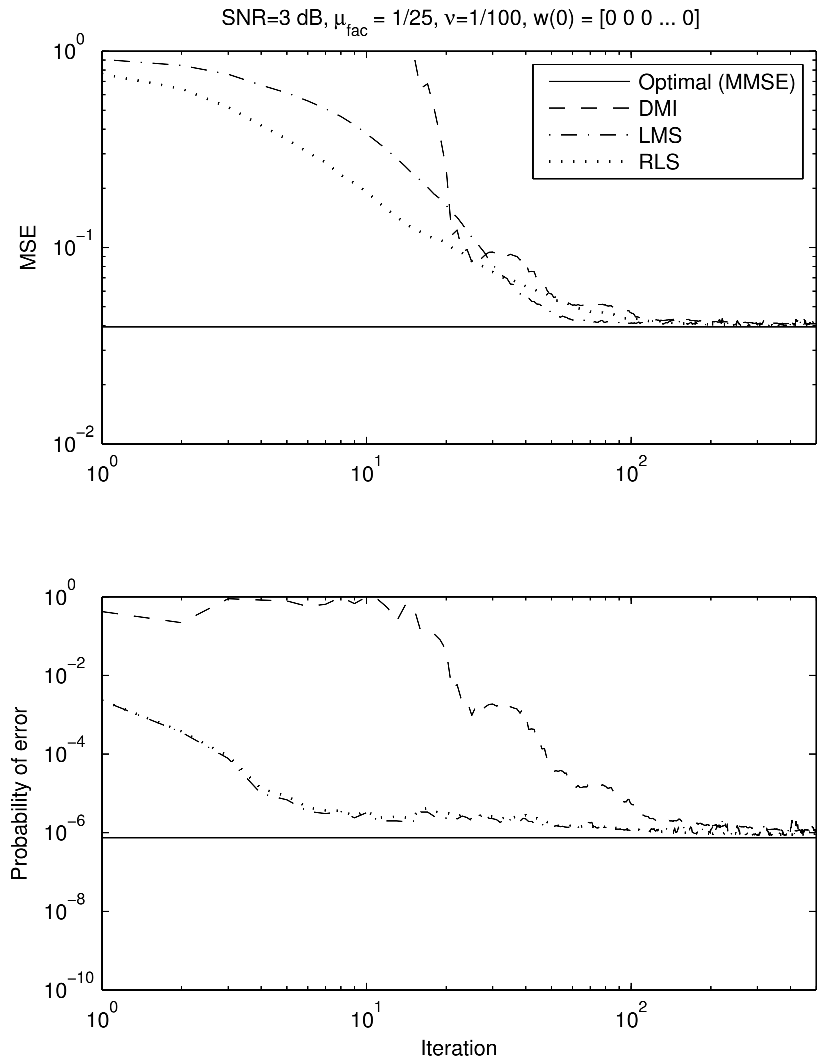

Figure C.1: Comparison of convergence for scenario I1

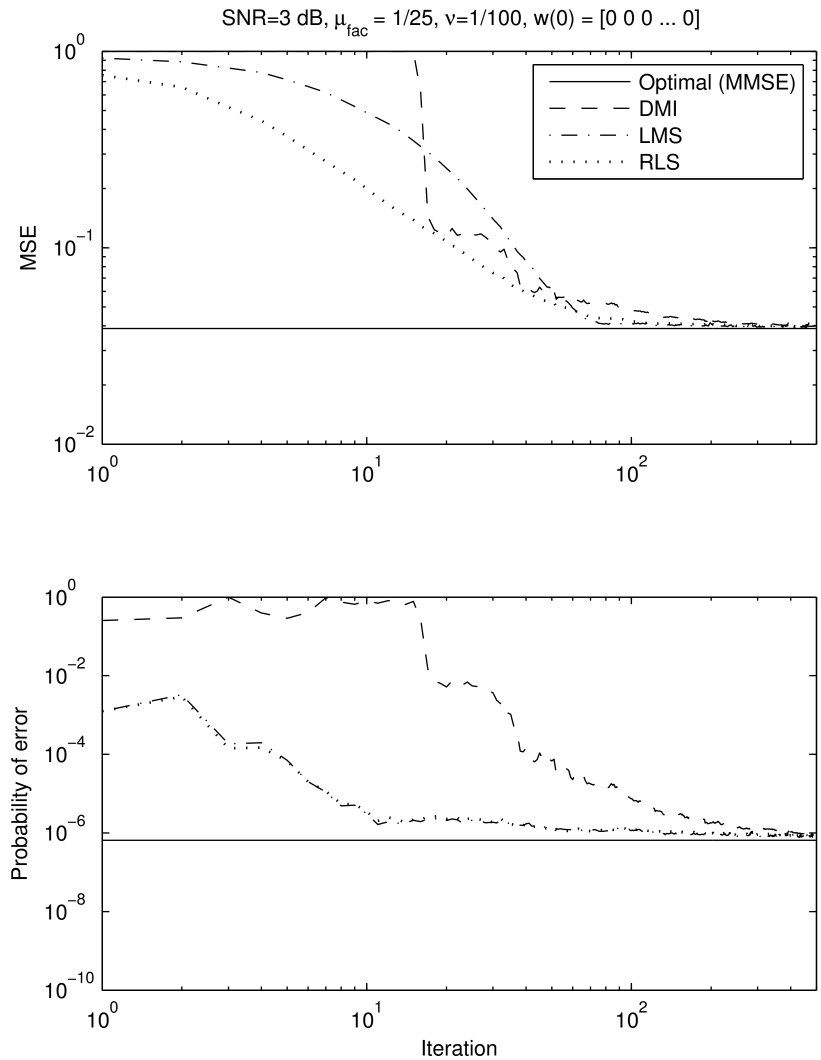

Figure C.2: Comparison of convergence for scenario I2

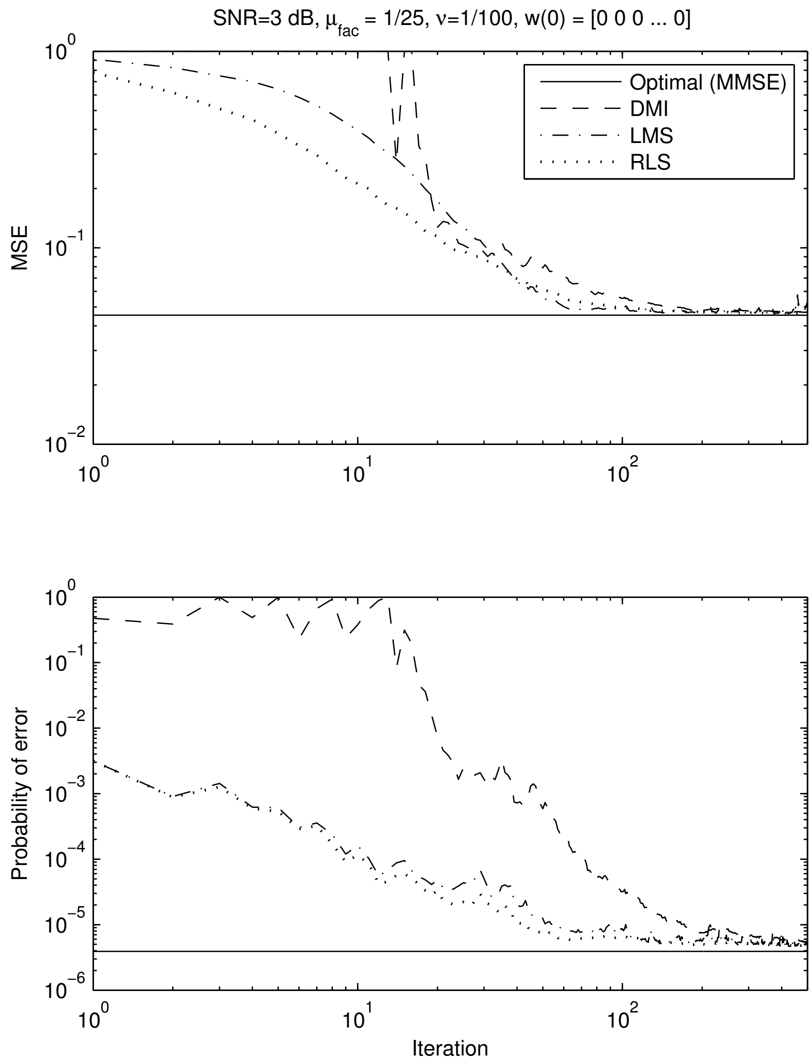

Figure C.3: Comparison of convergence for scenario I3

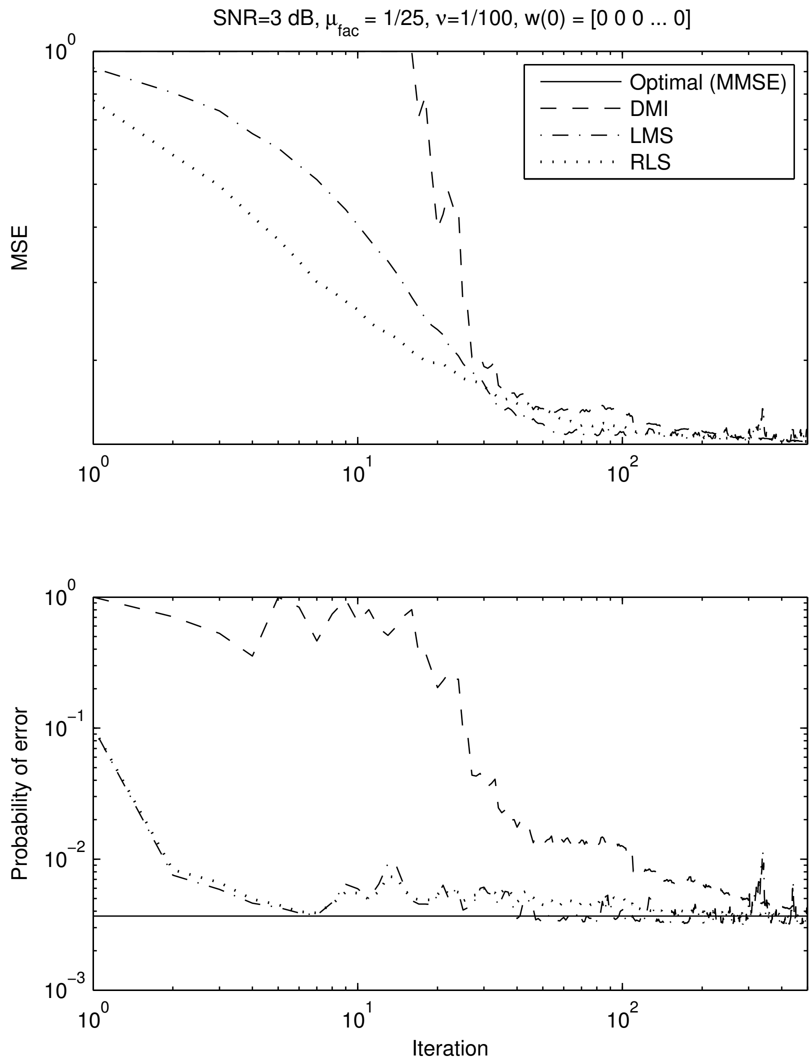

Figure C.4: Comparison of convergence for scenario I4

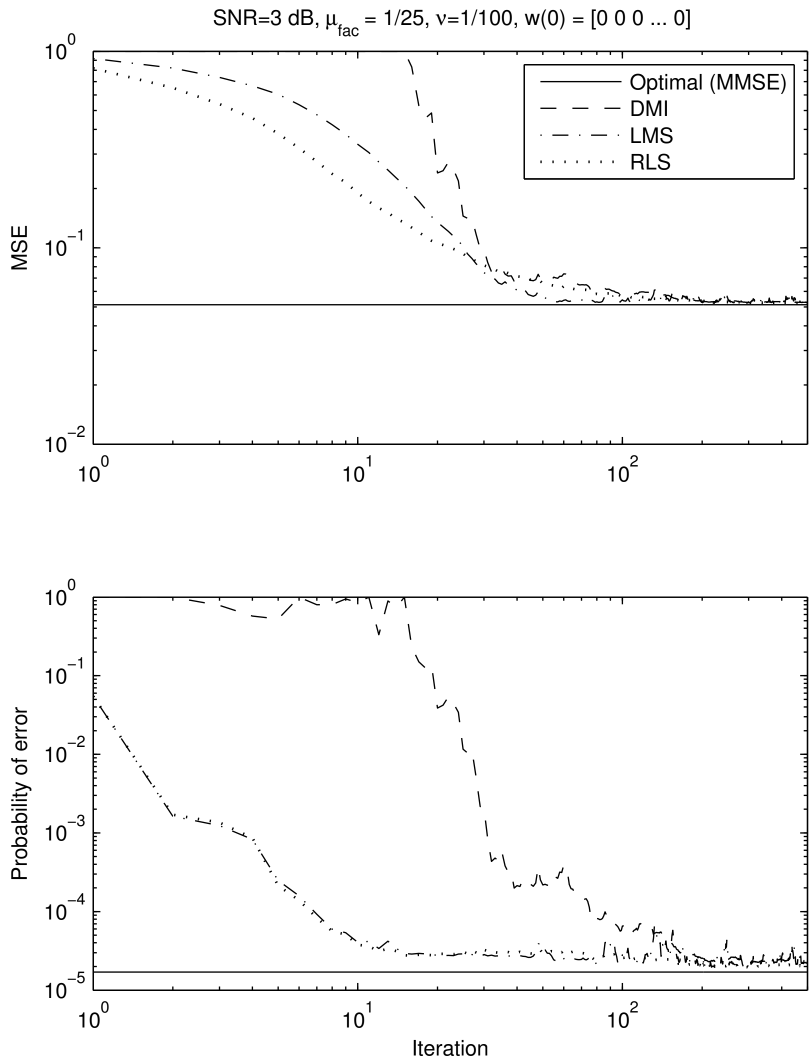

Figure C.5: Comparison of convergence for scenario I5

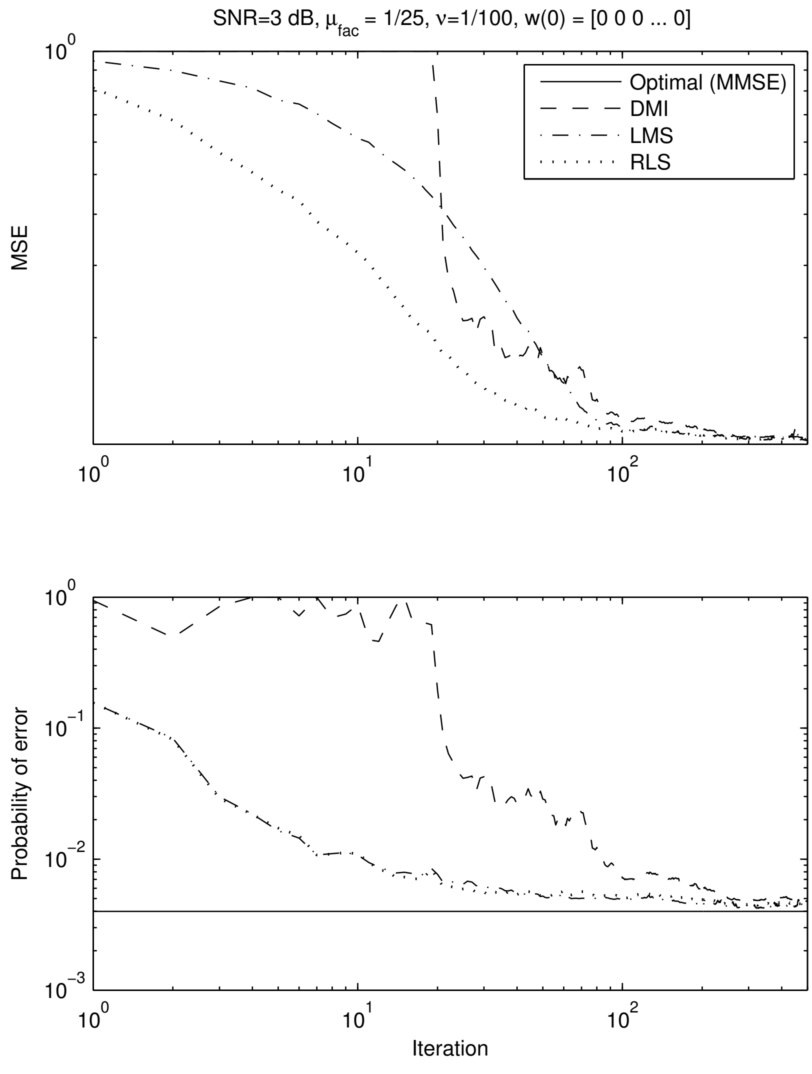

Figure C.6: Comparison of convergence for scenario I6

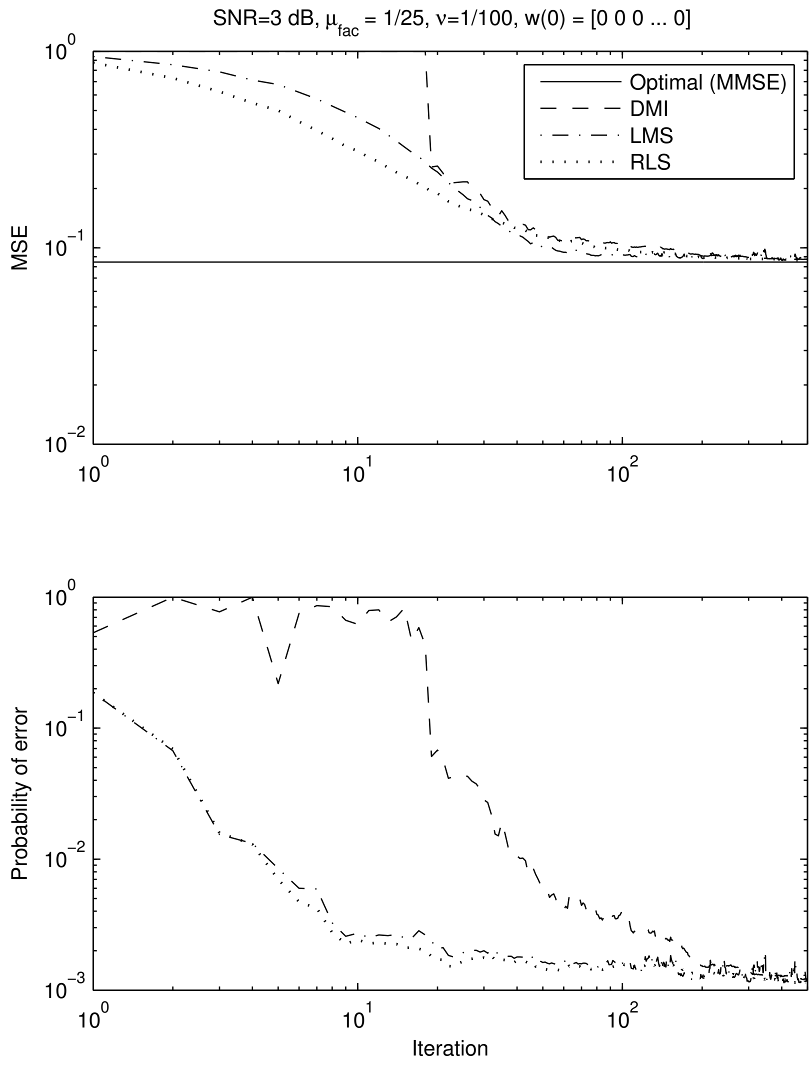

Figure C.7: Comparison of convergence for scenario I7

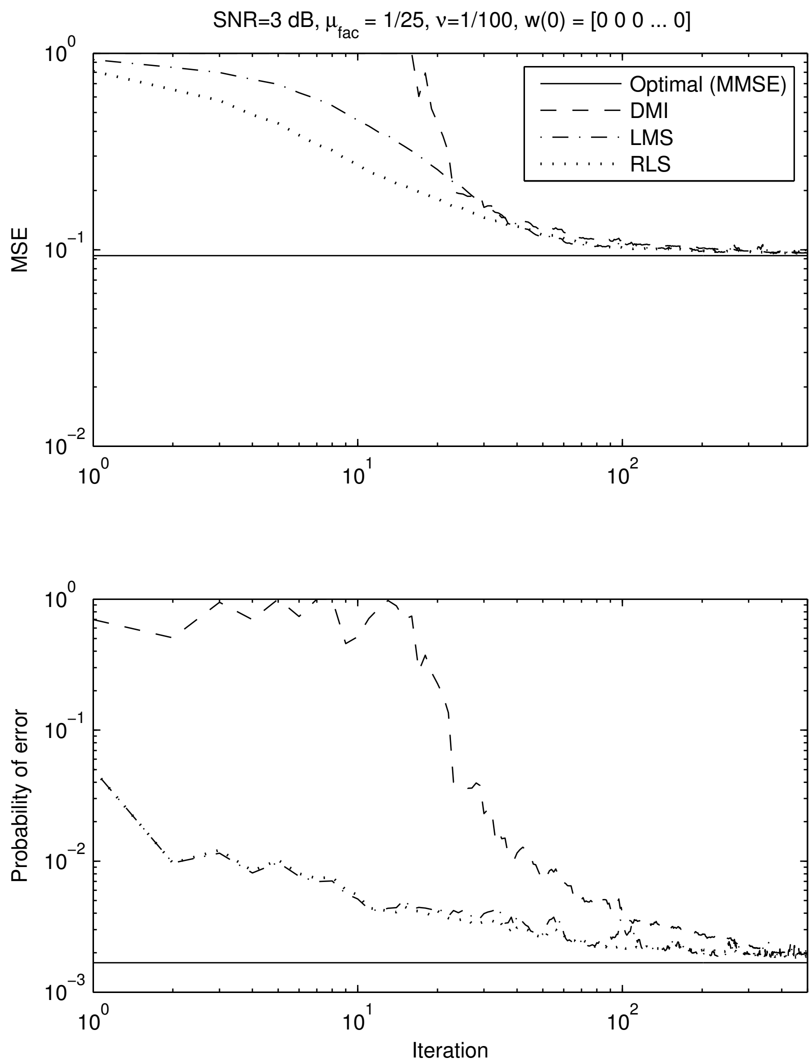

Figure C.8: Comparison of convergence for scenario I8

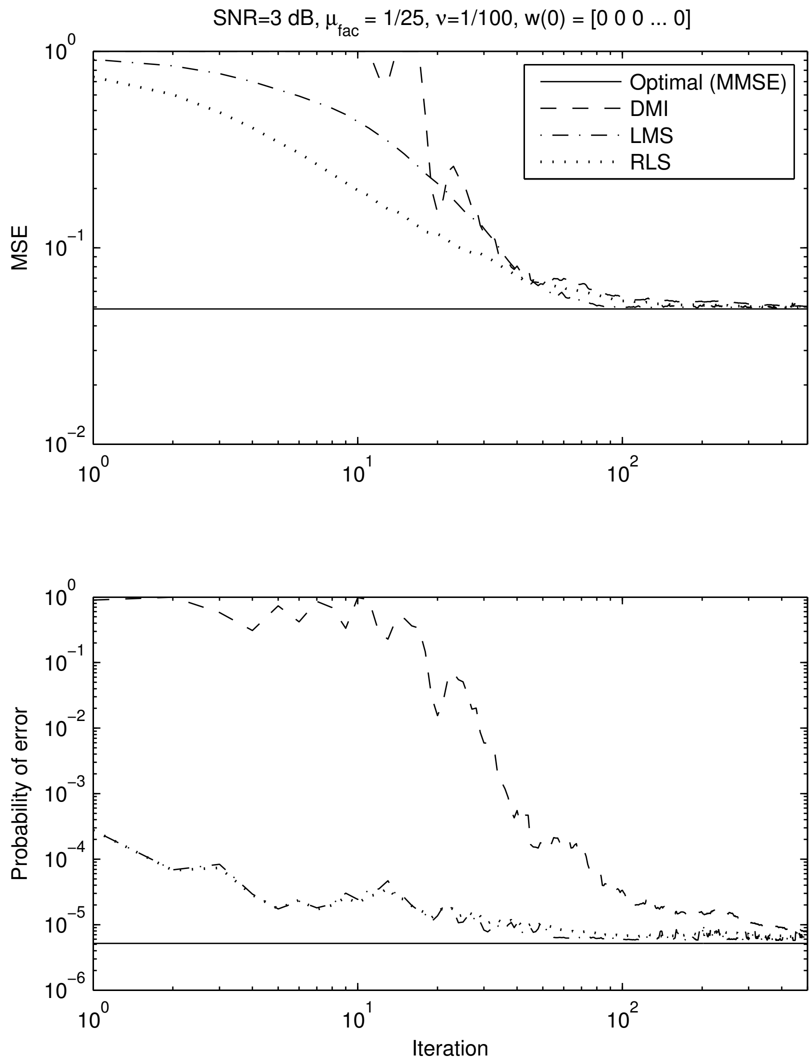

Figure C.9: Comparison of convergence for scenario I9

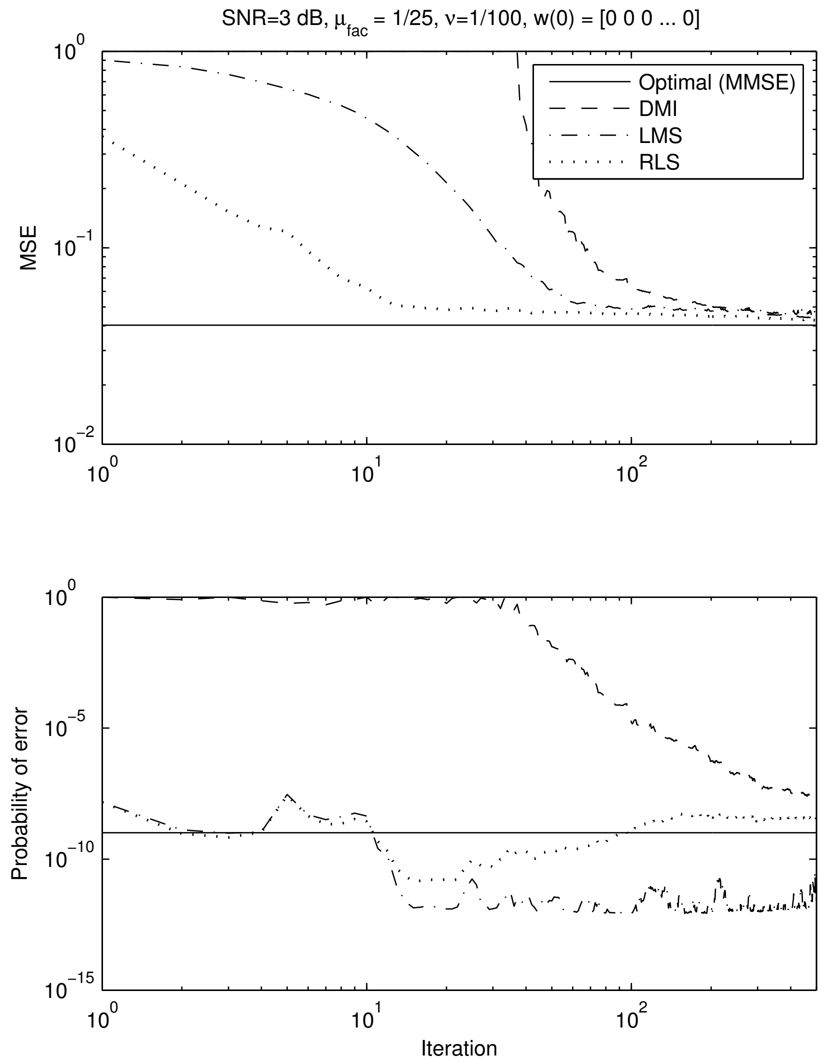

Figure C.10: Comparison of convergence for scenario O1

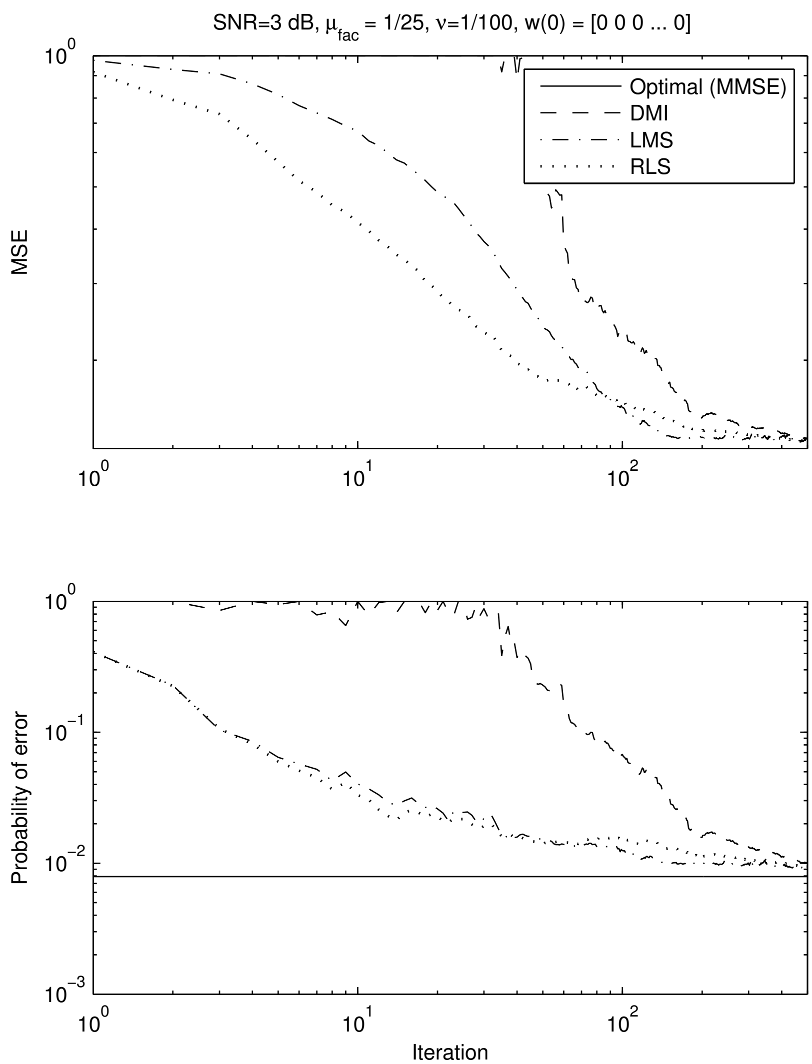

Figure C.11: Comparison of convergence for scenario O2

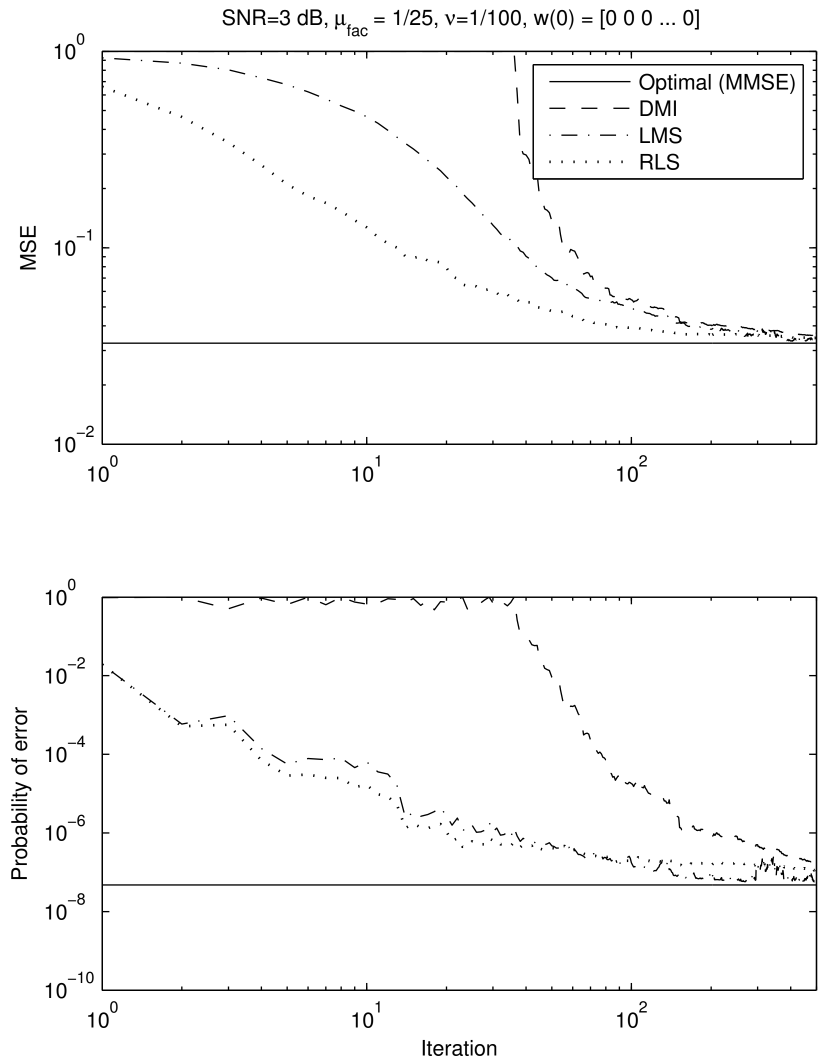

Figure C.12: Comparison of convergence for scenario O3

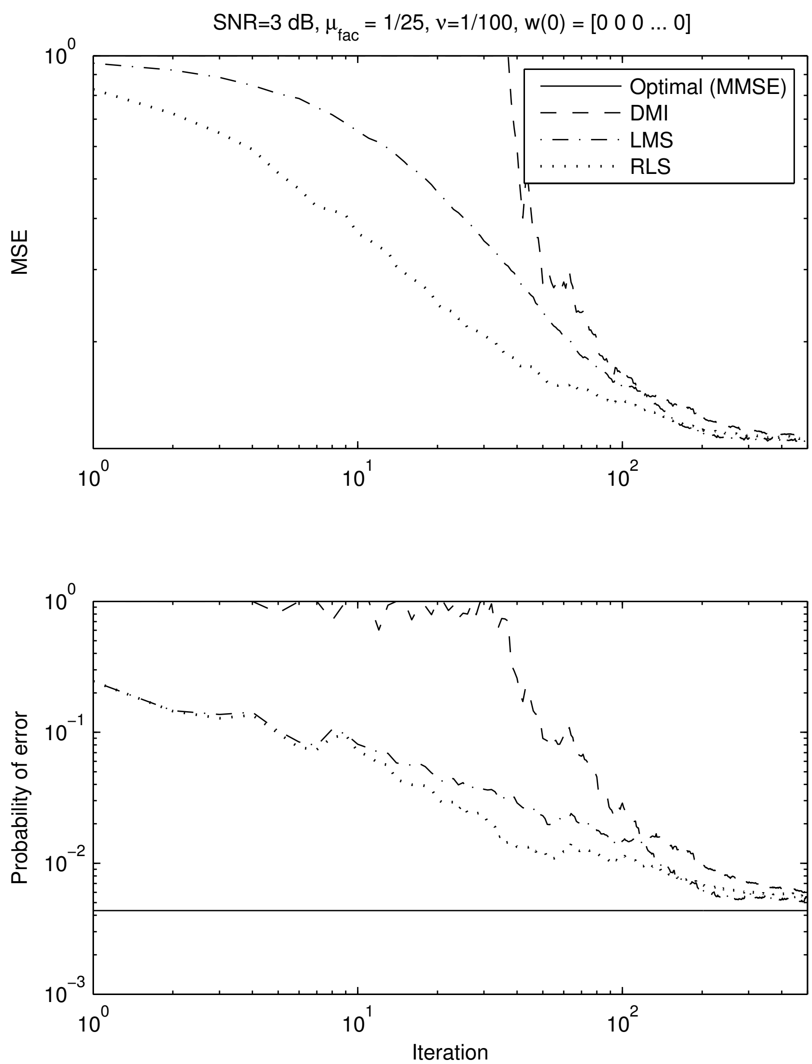

Figure C.13: Comparison of convergence for scenario O4

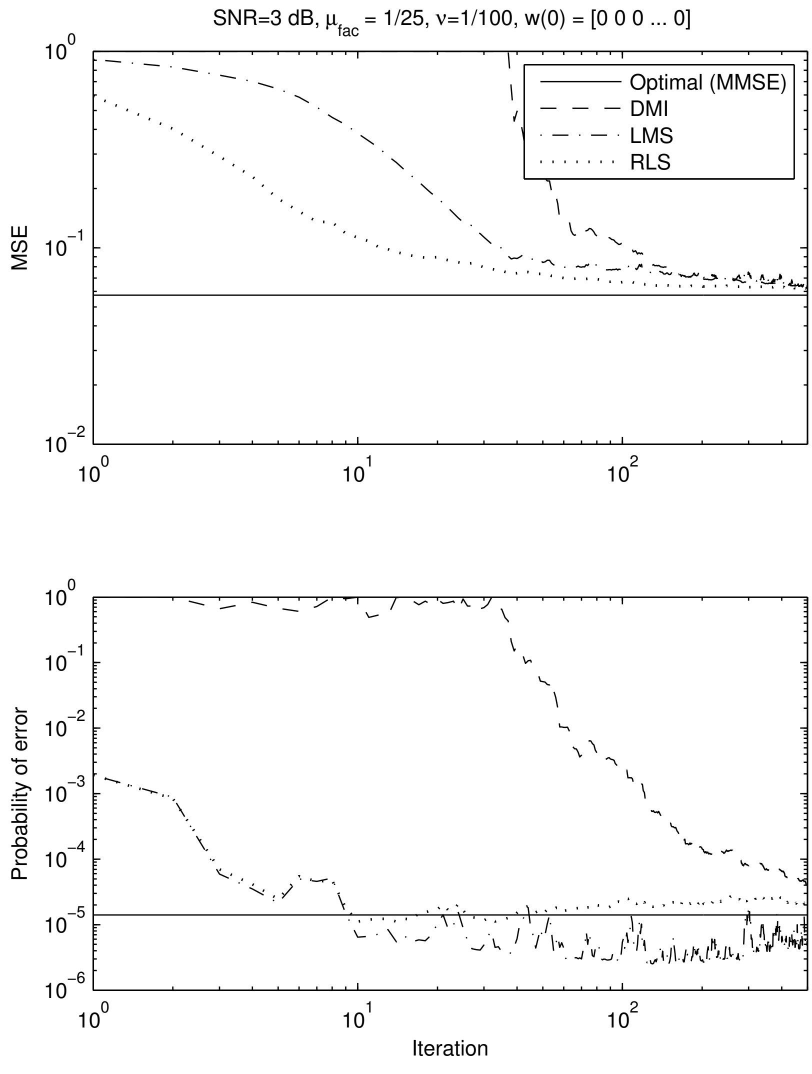

Figure C.14: Comparison of convergence for scenario O5

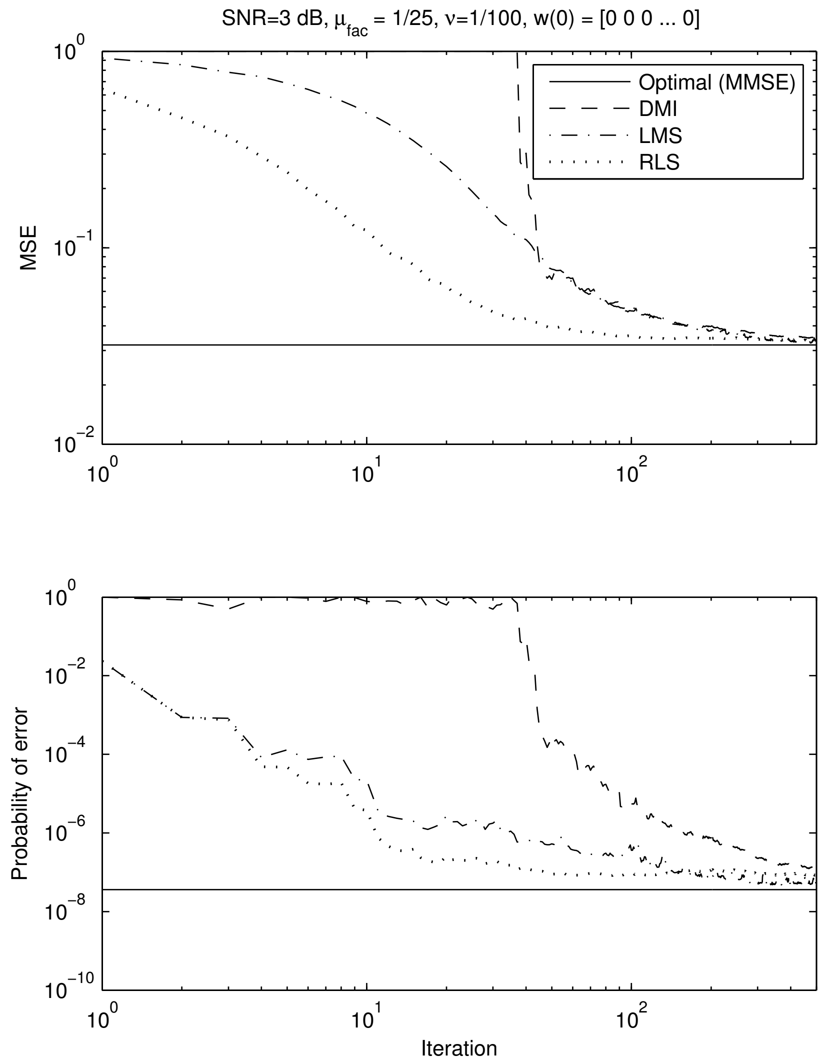

Figure C.15: Comparison of convergence for scenario O6

Bibliography

[1] N. Guo, R. C. Qiu, S. S. Mo, and K. Takahashi, "60-GHz Millimeter-Wave Radio: Principle, Technology, and New Results," *EURASIP J. Wirel. Commun. Netw.*, vol. 2007, pp. 48–48, Jan. 2007.

[2] A. Niknejad, "Siliconization of 60 GHz," *IEEE Microwave Mag.*, vol. 11, no. 1, pp. 78–85, Feb. 2010.

[3] R. Daniels, J. Murdock, T. Rappaport, and R. Heath, "60 GHz Wireless: Up Close and Personal," *IEEE Microwave Mag.*, vol. 11, no. 7, pp. 44–50, Dec. 2010.

[4] M. Marcus and B. Pattan, "Millimeter Wave Propagation; Spectrum Management Implications," *IEEE Microwave Mag.*, vol. 6, no. 2, pp. 54–62, June 2005.

[5] B. Langen, G. Lober, and W. Herzig, "Reflection and transmission behaviour of building materials at 60 GHz," in *Proc. IEEE 5th Int. Symp. on Personal, Indoor, Mobile Radio Commun.*, Sep. 1994, pp. 505–509.

[6] H. Xu, V. Kukshya, and T. Rappaport, "Spatial and Temporal Characteristics of 60-GHz Indoor Channels," *IEEE J. Sel. Areas Commun.*, vol. 20, no. 3, pp. 620–630, Apr. 2002.

[7] C. Anderson and T. Rappaport, "In-Building Wideband Partition Loss Measurements at 2.5 and 60 GHz," *IEEE Trans. Wireless Commun.*, vol. 3, no. 3, pp. 922–928, May 2004.

[8] W. L. Stutzman and G. A. Thiele, *Antenna Theory and Design.* New York: John Wiley & Sons, 1981.

[9] A. Myles and R. de Vegt, "Wi-Fi Alliance (WFA) VHT Study Group Usage Models," IEEE 802.11-07/2988r3, 2008, Available: http://www.ieee802.org/11/Reports/tgad_update.htm.

[10] S. Cotton, W. Scanlon, and B. Madahar, "Millimeter-Wave Soldier-to-Soldier Communications for Covert Battlefield Operations," *IEEE Commun. Mag.*, vol. 47, no. 10, pp. 72–81, Oct. 2009.

[11] T. S. Rappaport, *Wireless Communications: Principles and Practice*, 2nd ed. Upper Saddle River, N.J.: Prentice Hall, 2002.

[12] IEEE TGad, "PHY/MAC Complete Proposal Specification (approved as TGad D0.1)," IEEE 802.11-10/0433r2, 2010, Available: http://www.ieee802.org/11/Reports/tgad_update.htm.

[13] E. Damosso, L. Correia *et al.*, *Digital mobile radio towards future generation systems.* COST 231 Final Report, Brussels, Belgium: European Commission, 1999.

[14] D. Matic, H. Harada, and R. Prasad, "Indoor and outdoor frequency measurements for MM-waves in the range of 60 GHz," in *Proc. IEEE 48th Vehicular Technology Conf.*, vol. 1, May 1998, pp. 567–571.

[15] N. Moraitis and P. Constantinou, "Measurements and Characterization of Wideband Indoor Radio Channel at 60 GHz," *IEEE Trans. Wireless Commun.*, vol. 5, no. 4, pp. 880–889, Apr. 2006.

[16] B. Neekzad, K. Sayrafian-Pour, J. Perez, and J. Baras, "Comparison of Ray Tracing Simulations and Millimeter Wave Channel Sounding Measurements," in *Proc. IEEE 18th Int. Symp. Personal, Indoor, and Mobile Radio Commun.*, Sept. 2007, pp. 1–5.

[17] P. Smulders and L. Correia, "Characterisation of propagation in 60 GHz radio channels," *Electron. Commun. Eng. J.*, vol. 9, no. 2, pp. 73–80, Apr. 1997.

[18] A. Maltsev, V. Erceg, E. Perahia, C. Hansen, R. Maslennikov *et al.*, "Channel Models for 60 GHz WLAN Systems," IEEE 802.11-09/0334r8, 2010, Available: http://www.ieee802.org/11/Reports/tgad_update.htm.

[19] H. Zhang, S. Venkateswaran, and U. Madhow, "Channel Modeling and MIMO Capacity for Outdoor Millimeter Wave Links," in *Proc. IEEE Wireless Communications and Networking Conf.*, Apr. 2010, pp. 1–6.

[20] G. D. Durgin, "Advanced site-specific propagation prediction techniques," Master's thesis, Bradley Dept. Elect. Comput. Eng., Virginia Tech, Blacksburg, VA, 1998.

[21] H. Bertoni, W. Honcharenko, L. Macel, and H. Xia, "UHF propagation prediction for wireless personal communications," *Proc. IEEE*, vol. 82, no. 9, pp. 1333–1359, Sept. 1994.

[22] J. Proakis and M. Salehi, *Digital Communications*, 5th ed. Boston:McGraw-Hill, 2008.

[23] C. Balanis and P. Ioannides, *Introduction to Smart Antennas*, 1st ed. Morgan & Claypool Publishers, 2007.

[24] H. L. Van Trees, *Optimum Array Processing.* Wiley Online Library, 2002.

[25] B. Van Veen and K. Buckley, "Beamforming: A Versatile Approach to Spatial Filtering," *IEEE ASSP Mag.*, vol. 5, no. 2, pp. 4–24, Apr. 1988.

[26] E. Ben-Dor, T. Rappaport, Y. Qiao, and S. Lauffenburger, "Millimeter-Wave 60 GHz Outdoor and Vehicle AOA Propagation Measurements Using a Broadband Channel Sounder," in *Proc. IEEE Global Telecommunications Conf.*, Dec. 2011, pp. 1–6.

[27] U. Pfeiffer and D. Goren, "A 20 dBm Fully-Integrated 60 GHz SiGe Power Amplifier With Automatic Level Control," *IEEE J. Solid-State Circuits*, vol. 42, no. 7, pp. 1455–1463, July 2007.

[28] Y.-N. Jen, J.-H. Tsai, T.-W. Huang, and H. Wang, "Design and Analysis of a 55–71 GHz Compact and Broadband Distributed Active Transformer Power Amplifier in 90-nm CMOS Process," *IEEE Trans. Microw. Theory Tech.*, vol. 57, no. 7, pp. 1637–1646, July 2009.

[29] E. Cohen, S. Ravid, and D. Ritter, "An ultra low power LNA with 15dB gain and 4.4db NF in 90nm CMOS process for 60 GHz phase array radio," in *Proc. IEEE Radio Frequency Integrated Circuits Symp.*, Apr. 2008, pp. 61–64.

[30] J. Wang, Z. Lan, C.-S. Sum, C.-W. Pyo, J. Gao, T. Baykas, A. Rahman, R. Funada, F. Kojima, I. Lakkis, H. Harada, and S. Kato, "Beamforming Codebook Design and Performance Evaluation for 60GHz Wideband WPANs," in *Proc. IEEE 70th Vehicular Technology Conf.*, Sept. 2009, pp. 1–6.

[31] M. Khan, "Antenna Beamforming for a 60 GHz Transceiver System," Master's thesis, Elect. Eng. Math. Comput. Sci., Delft Univ. Tech., Delft, The Netherlands, 2009.

[32] C.-S. Choi, M. Elkhouly, E. Grass, and C. Scheytt, "60-GHz adaptive beamforming receiver arrays for interference mitigation," in *Proc. IEEE 21st Int. Symp. Personal Indoor and Mobile Radio Commun.*, Sept. 2010, pp. 762–767.

[33] H. Yang, P. F. M. Smulders, and M. H. A. J. Herben, "Channel characteristics and transmission performance for various channel configurations at 60 GHz," *EURASIP J. Wirel. Commun. Netw.*, vol. 2007, pp. 43–43, Jan. 2007.

[34] Y. Ogawa, M. Ohmiya, and K. Itoh, "An LMS Adaptive Array for Multipath Fading Reduction," *IEEE Trans. Aerosp. Electron. Syst.*, vol. 23, no. 1, pp. 17–23, Jan. 1987.

[35] S. Anderson, M. Millnert, M. Viberg, and B. Wahlberg, "An adaptive array for mobile communication systems," *IEEE Trans. Veh. Technol.*, vol. 40, no. 1, pp. 230–236, Feb. 1991.

[36] F. Gross, *Smart Antennas for Wireless Communications with MATLAB*. New York: McGraw-Hill, 2005.

[37] R. Monzingo, R. Haupt, and T. Miller, *Introduction to Adaptive Arrays*, 2nd ed. Raleigh, N.C.: SciTech Pub., 2011.

[38] S. Haykin, *Adaptive Filter Theory*, 4th ed. Upper Saddle River, N.J.: Prentice Hall, 2002.

[39] B. Widrow, P. Mantey, L. Griffiths, and B. Goode, "Adaptive antenna systems," *Proc. IEEE*, vol. 55, no. 12, pp. 2143–2159, Dec. 1967.

[40] J. Wang, Z. Lan, C.-W. Pyo, T. Baykas, C.-S. Sum, M. Rahman, J. Gao, R. Funada, F. Kojima, H. Harada, and S. Kato, "Beam codebook based beamforming protocol for multi-Gbps millimeter-wave WPAN systems," *IEEE J. Sel. Areas Commun.*, vol. 27, no. 8, pp. 1390–1399, Oct. 2009.

[41] D. Brandwood, "A complex gradient operator and its application in adaptive array theory," *IEE Proc. Microw. Optics and Antennas*, vol. 130, no. 1, pp. 11–16, Feb. 1983.

[42] A. Bryson and Y. Ho, *Applied Optimal Control: Optimization, Estimation, and Control*. Washington: Hemisphere Pub. Corp., 1975.

[43] S. Chen, N. Ahmad, and L. Hanzo, "Adaptive Minimum Bit-Error Rate Beamforming," *IEEE Trans. Wireless Commun.*, vol. 4, no. 2, pp. 341–348, Mar. 2005.

[44] B. Carlson, "Covariance matrix estimation errors and diagonal loading in adaptive arrays," *IEEE Trans. Aerosp. Electron. Syst.*, vol. 24, no. 4, pp. 397–401, July 1988.

[45] N. Celik, M. Iskander, R. Emrick, S. Franson, and J. Holmes, "Implementation and Experimental Verification of a Smart Antenna System Operating at 60 GHz Band," *IEEE Trans. Antennas Propag.*, vol. 56, no. 9, pp. 2790–2800, Sept. 2008.